



Development of alternative cementitious binders and functionalized materials

DESIGN, PERFORMANCE AND DURABILITY

Anna Kaja

Bouwstenen

308

Development of alternative cementitious binders and functionalized materials

DESIGN, PERFORMANCE AND DURABILITY

Anna Monika Kaja

This work is part of the research programme “Tailoring new nano-silica and its application in smart concrete” with project number 12824, which is (partly) financed by the Netherlands Organisation for Scientific Research (NWO).



CIP-DATA LIBRARY TECHNISCHE UNIVERSITEIT EINDHOVEN

Development of alternative cementitious binders and functionalized materials / by Anna Kaja

A catalogue record is available from the Eindhoven University of Technology Library

ISBN: 978-90-386-5225-2

Bouwstenen 308

NUR 955

Copyright © 2021 by Anna Kaja

Ph.D. thesis, Eindhoven University of Technology, the Netherlands

Cover design: Anna Kaja, Photo by Jan Kroon from Pexels

Printed by: www.proefschriftmaken.nl

All rights reserved. No part of this publication may be reproduced in any form or by any means without permission in writing form from the author.

Development of alternative cementitious binders and functionalized materials

DESIGN, PERFORMANCE AND DURABILITY

PROEFSCHRIFT

ter verkrijging van de graad van doctor
aan de Technische Universiteit Eindhoven,
op gezag van de rector magnificus, prof.dr.ir. F.P.T. Baaijens,
voor een commissie aangewezen door het College voor Promoties,
in het openbaar te verdedigen op woensdag 24 maart 2021 om 13:30 uur

door

Anna Monika Kaja

geboren te Limanowa, Polen

Dit proefschrift is goedgekeurd door de promotoren en de samenstelling van de promotiecommissie is als volgt:

Voorzitter: prof.dr.ir. T.A.M. Salet
1^e promotor: prof.dr.ir. H.J.H. Brouwers
2^e promotor: prof.dr. Q.L. Yu (Wuhan University)
Leden: prof.dr. W. Chen (Wuhan University of Technology)
prof.dr. H. Justnes (Norwegian University of Science and Technology)
prof.dr.eng. J. Deja (AGH University of Science and Technology)
prof.dr. S.R. van der Laan
prof.ir. S.N.M. Wijte

Het onderzoek of ontwerp dat in dit proefschrift wordt beschreven is uitgevoerd in overeenstemming met de TU/e Gedragscode Wetenschapsbeoefening.

Preface

With writing this thesis, I come to the end of Anna's PhD story. I am happy to be at this point, but at the same time, I feel very nostalgic. Well, it has been more than 4 years!

I would like to start with a word of thanks to my promotors Prof.dr.ir. H.J.H (Jos) Brouwers and Prof.dr. Qingliang Yu. Jos, this story began when you accepted my application for the PhD position. I want to thank you for these 4 years of working together, for teaching me how to approach the research problems and how to translate the research into real-world solutions through collaboration with the companies. Thank you for your trust and your encouragement in my scientific growth. I would like to also express my warmest thanks to my second promotor Qingliang. You were of enormous support to me throughout the entire PhD process, from my tough beginnings to the final stages, leading to my defense. Working with you is an unforgettable experience. You were the one to check the 15th version of the same paper draft and the one to help me get back on track with my work when I was facing various troubles. With our countless talks and your patient guidance, I always felt motivated to aim higher and do more. You helped me to develop as a scientist but also to shape my character.

I would like to thank also the committee members for reading this thesis, for the positive feedback and valuable suggestions for improvements.

My great gratitude goes to Dr. Alberto Lazaro and Prof.dr. Sieger van der Laan. Alberto, you were my supervisor during the first year of my PhD study. I remember you questioning my ideas to help me define my research path. I am glad I had support from such a knowledgeable person. Sieger, you became my unofficial supervisor during the last years of my PhD. Thank you for sharing with me your enthusiasm and passion for science. You showed me that the limits are in our heads, and it is always useful to question them.

Dr. Katrin Schollbach and Dr. Stefan Melzer, thanks for the work we have done together. What a great lesson on mineralogy and XRD I received from you! With your friendly attitude and willingness to help, the learning process was enjoyable and exciting.

The performance of the experiments presented in this thesis would not be possible without the support of our technicians Anneke Delsing and Harrie Smulders. Thank you for all your help, especially at the end of my PhD study, when the coronavirus started and I was in the middle of my last experiments. I would not reach this point without your openness and willingness to help. Thank you!

Przemek Spiesz, you are the first Polish person I met in the Netherlands and the first one to help me start on my PhD path. It was of great value to have support from someone who faced similar challenges. Here, I would also like to thank my Polish neighbour Mirka. Thank you for your openness, valuable talks, but also for introducing me to the church community. Agata, Ewa, and Kinga (Polish girls from the 6th floor), you brought to our office a piece of Polish culture and homelike feeling with all the talks and jokes, which can only be said in Polish.

Warm thanks go to a few people who I met at university quite unexpectedly, through different turns of events, and who brought lots of happiness to my life. Jonathan, thank you for all the joyful time that we spent together. Those are countless moments. Little Darda (Giorgia), thanks for your presence, young spirit, and energy to make good use of the time here (you made me discover the best ice cream in Eindhoven!). And Varun, thank you for your openness, for your support and friendliness, for all the cycling trips.

Throughout these years of PhD life, I met so many amazing people. With some of you, I got recently in touch, and some of you are already in different parts of the world. I would like to thank the church community for supporting my spiritual development, the salsa community for sharing with me the joy of dancing, and the community of Hemelrijken, including my dear PDEngs (for our international parties), and more recently, Rastko and Nika (for the dinners and funny Slavic talks). I am also grateful for the 6th-floor community. With all the chitchats at the coffee machine corner and during lunches, the office was always full of life. I especially thank our dear secretaries, Leontine and Nathaly, for building up this community, creating good atmosphere, for the great support and friendly Goede Morgen every day!

My dear Building Materials group, my daily life, full of ups and downs, I shared with you. My desk was in the centre of our office corner, and despite the people around me were changing during these 4 years, I always felt that I am surrounded by friends. Here, I would

like to express my special thanks to Winnie, TaoTao (Tao), and Jawados (Jawad). You gave me this strong feeling of belonging and support in every matter. I truly enjoyed the time with you, Tao's piano concerts, the philosophical speeches of Jawad, and all the adventures with Winnie (with her unconstrained imagination). Our office would not be the same without Katka, Veronica, Florent, Kate, Miruna, Perry, Azee, and Qadeer calling for the morning coffee, without Hoss, Guillaume, and Jonathan, making funny jokes, or without Yan posing his "Why not?". I appreciate our "scientific" discussions, especially with Yuri, Zixiao, Kinga, Chris, and Bo. Yuri, it was a pleasure to work on the same project with such a knowledgeable researcher. Gang, Xu, Peipeng, Cao, Yuxuan, Zhengyao, Pei, and Xiaoxiao, I want to thank you in particular for your hospitality in China. I am amazed by your culture and your friendliness, which I also experienced from the "younger generation," including Xuan (my dear soul mate), Shaohua, Huarong, Fan, Yanjie, and Ce. I also say thank you to the newcomers. Charles, Iris, Ricardo, Helong, and Zhihan, I wish you all the best for these amazing yet challenging years ahead. My dear group, I will remember all the moments together, including trips, game nights, birthday celebrations, dinners (especially spicy woks), late evening walks, or ice creams at Strijp S, with a smile on my face.

Finally, my special appreciation goes to my friends who were supporting me from Poland. Magda, Kara, Dominik, and Bernadka, with you, distance is not a problem. I am feeling extremely happy to have you, and I am sure that those are lifetime friendships!

Szczególne podziękowania kieruję oczywiście do mojej drogiej rodzinki, mamy (Małgorzaty), taty (Jana), Renaty, Pawła i Witusia oraz Natalii, Pawła i Hanii! Bez Was na pewno by mi się nie udało. Wasze codzienne wsparcie nie równa się z żadnym innym. Jak dobrze mieć taką rodzinę! Cokolwiek by się nie działo i gdziekolwiek bym nie była, wiem, że mam Was i zawsze mogę na Was liczyć!

Anna Kaja

Eindhoven, November 2020

Summary

Three fundamental aspects, namely, market competitiveness (costs), availability of resources and environmental impact, determine the need for implementation of new solutions in concrete technology. Facing the challenge of the optimization of these interactive aspects, this thesis firstly focuses on the improvement of existing eco-friendly technology (alkali-activated materials), secondly, offers the design of new alternative binders (BOF slag) and finally investigates opportunities for air-purifying technology in concrete.

In the first section, alkali-activated materials are discussed. The nature and properties of alkali-activated materials depend on the chemical composition and reactivity of the resources used. Alkali-activated materials from siliceous/aluminous by-products (geopolymers) offer excellent properties, e.g., chemical resistance or fire resistance. However, the manufacture of geopolymers often requires the external heat supply to ensure a sufficient rate of geopolymerization, especially at an early age. In order to overcome this problem, the addition of small quantities of cement (up to 10 wt%) is proposed. The impact of cement addition on the reaction kinetics and phase development and their subsequent influences on the usage properties, including setting time and mechanical performance, are investigated thoroughly. The optimal dosages of cement required to avoid non-ambient temperature curing and to maintain high compressive strength are correlated with the silica modulus of the sodium silicate activator.

The second section moves towards new potentially reactive binders, dealing with the activation of Basic Oxygen Furnace (BOF) slag, a by-product of steel manufacture. This material is currently not utilized as a binder in concrete due to its low reactivity and contamination with heavy metals (mainly vanadium and chromium). Based on the phase composition of BOF slag, a novel route to activate iron-containing phases is proposed and investigated. The tri-potassium citrate is selected to activate the slag phases and to reduce the water demand of slag as it also possesses a superplasticizing function. The K_3 -citrate is found to promote the dissolution and hydration of brownmillerite, which hydrates mostly within the first 24 hours and to accelerate the hydration of belite and wuestite. An analogous

working mechanism is observed for BOF slag pastes activated with the Na_3 -citrate. The main reaction products of BOF slag hydration are determined and modeled, including siliceous hydrogarnet, pyroaurite and C-S-H gel. It is revealed that the addition of K_3 -citrate significantly reduces the water demand of slag, enabling the production of BOF slag paste with low porosity (10-16%) and desirable compressive strength up to 75 MPa after 28 days of hydration. The early age mechanical properties of BOF slag-based products are further optimized with the addition of nanosilica. By applying the in-situ XRD and thermogravimetric analyses, it is found that nanosilica enhances precipitation of C-S-H gel while delays the hydration of brownmillerite. The enhanced formation of C-S-H gel improves the compressive strength of mortars after 3 and 7 days of hydration. However, the mechanical performance after 28 days is compromised. Therefore, the synergistic effects of activator dosage and nanosilica content must be considered to meet the desired strength criteria. Finally, the environmental impact of the newly designed products is investigated by utilizing the leaching tests. The leaching properties of BOF slag pastes are evaluated with the one-batch leaching test and tank test on the hydrated samples before and after accelerated carbonation curing. This strategy is applied in order to predict the durability and potential toxicity of the BOF products during their service life. The concentrations of vanadium and chromium released from the samples are examined with regard to the limit values specified in the Dutch Soil Quality Decree.

In the last section, the potential of functionalization of concrete with the application of nanotitania particles in the mortar mixtures is investigated in terms of air purification. For the representativity of the results, two types of titania nanoparticles (P25 and KRONOClean 7000 carbon-doped) and one (synthesized) silica-titania composite are analysed. As photocatalytic oxidation of the pollutants takes place only on the concrete surface, which is exposed to atmospheric conditions, the durability aspects (carbonation) are investigated. Upon carbonation, the phase composition of concrete is altered, consequently affecting the pH, specific surface area and porosity. These factors, in turn, have a significant impact on photocatalytic efficiency. Therefore, the carbonation-induced physicochemical changes are analysed and compared for two mortar series, the first one rich- and the second one free of portlandite. White Portland cement is employed as the primary binder in both mortar series, and pozzolanic microsilica is applied in the second mix to adjust the portlandite content. This strategy is used to differentiate between the impact of carbonation of CH and the C-S-

H phase on photocatalytic performance. In consequence, the prediction of the photocatalytic efficiency during the service life of photocatalytic mortars can be performed based on the initial mix design. The results reveal that mortars with microsilica addition exhibit superior properties over the pure cement-based mortars upon carbonation in terms of both photocatalytic efficiency and selectivity. The carbonation of C-S-H gel results in the formation of capillary pores between 10-50 nm, which outbalances the shielding effects of carbonates formed, leading to enhanced photocatalytic properties. Furthermore, in contrast to CH, the C-S-H gel maintains its high NO₂ adsorption capacity after carbonation.

Content

1	Introduction	1
1.1	Background and motivation.....	1
1.2	Scope and objectives	5
1.3	Outline of the thesis	6
2	Effects of Portland cement on the activation mechanism of class F fly ash geopolymer cured under ambient conditions.....	9
2.1	Introduction.....	9
2.2	Experimental	11
2.2.1	Materials	11
2.2.2	Sample preparation and test methods	13
2.3	Results and discussion.....	15
2.3.1	Setting behaviour.....	15
2.3.2	Reaction kinetics	16
2.3.3	Infrared spectroscopy analysis of the activation process	18
2.3.4	Microstructure.....	21
2.3.5	Phase characterization.....	23
2.3.6	Mechanical performance	26
2.4	Conclusions	27
3	Hydration of potassium citrate-activated BOF slag	29
3.1	Introduction.....	29
3.2	Materials and methods	31
3.2.1	Materials and mix design	31
3.2.2	Methodology	33
3.3	Results and discussion.....	36
3.3.1	Characterization of unhydrated BOF slag.....	36
3.3.2	Isothermal calorimetry.....	37
3.3.3	Identification of reactive phases.....	39
3.3.4	Hydrates assemblage	41

3.3.5	Microstructure and mechanical properties	46
3.3.6	Environmental impact	48
3.4	BOF slag hydration: theoretical water demand and chemical shrinkage	49
3.5	Conclusions	52
4	The optimization of BOF slag hydration kinetics	55
4.1	Introduction.....	55
4.2	Experimental	56
4.2.1	Materials	56
4.2.2	Mix design and sample preparation	58
4.2.3	Methodology	59
4.3	Results and discussion.....	61
4.3.1	Hydration kinetics	61
4.3.2	Phase assemblage.....	62
4.3.3	Hydration of brownmillerite	63
4.3.4	Hydration of silicate	65
4.3.5	Mechanical performance	69
4.4	Conclusions	70
5	Effects of carbonation on the retention of heavy metals in chemically activated BOF slag pastes	73
5.1	Introduction.....	73
5.2	Experimental	76
5.2.1	Materials	76
5.2.2	Methodology	77
5.2.2.1	Mix design and sample preparation.....	77
5.2.2.2	Evaluation of the hydration process	78
5.2.2.3	Carbonation resistance and heavy metals retention.....	79
5.3	Results analysis	80
5.3.1	Hydration of BOF slag phases	80
5.3.2	Environmental impact	84
5.3.2.1	Leaching of heavy metals before carbonation	84
5.3.2.2	Leaching of heavy metals after carbonation	87
5.4	Conclusions	92
6	NO_x degradation by photocatalytic mortars: The underlying role of the CH and C-S-H carbonation	95
6.1	Introduction.....	95

6.2	Experimental	99
6.2.1	Materials	99
6.2.2	Mix design and sample preparation	100
6.2.3	Methods	101
6.3	Results analysis	104
6.3.1	Mortars characterization	104
6.3.2	Photocatalytic efficiency	108
6.4	Discussion	111
6.4.1	Influence of carbonation on the photocatalytic performance	111
6.4.2	Influence of carbonation on selectivity	112
6.5	Conclusions	114
7	Conclusions and recommendations	117
7.1	Conclusions	117
7.1.1	Ambient cured silica-rich alkali activated materials	117
7.1.2	BOF slag as a cementitious binder	118
7.1.3	The durability of photocatalytically active mortars	119
7.2	Recommendations	120
7.2.1	Ambient cured silica-rich alkali activated materials	121
7.2.2	BOF slag as a cementitious binder	121
7.2.3	The durability of photocatalytically active mortars	122
	Bibliography	123
	List of publications	139
	Curriculum Vitae	141

Introduction

1.1 Background and motivation

Cement sector is the second-largest industrial emitter of CO₂ (6-7% of global emissions) [1], [2]. Based on the current prognosis, the demand for cement and concrete is expected to rise about 12-23% by 2050, therefore, further increasing its share in the total industrial emission of CO₂ (4% from the current level) [1]. In this context, the cement industry is facing a great challenge to fulfill the new climate policies, aiming to limit global warming to 2% in the twenty-first century, according to the Paris Agreement [3]. Following the new policy measures, in many countries, carbon taxes have been implemented to enforce the changes [1]. In the cement sector, several strategies, presented by the International Energy Agency (IEA) and the Cement Sustainability Initiative (CSI), have been proposed to tackle the CO₂ emission problem [2]. Owing to the fact that about two-thirds of the total CO₂ emission during cement manufacture originates from the decomposition of limestone (clinker production) and one-third is due to combustion of fuels, the primary focus is the reduction of the clinker factor (defined as clinker to cement ratio) [1]. The commonly applied strategies to minimize the use of clinker in cement and concrete include the application of supplementary cementitious materials (reducing clinker content) and the manufacture of alkali activated materials (often clinker-free) [4], [5]. Another solution is the utilisation of alternative clinkers (belite clinker, calcium sulphoaluminate clinker). Since the currently used by-products (including fly ash, ground granulated blast furnace slag (GGBS), silica fume) have recently received high market value due to their excellent properties and limited accessibility, further improvement is foreseen through the implementation of currently non-used by-products (so-called alternative binders) [4]. High potential in reducing the environmental impact of cement is also recognised in advanced technologies, including the

integration of carbon capture into the cement manufacturing process and adoption of life-cycle approaches e.g. with the re-use of crushed concrete fines [2].

Alkali activated materials

The supplementary cementitious materials can be used as partial cement substituents but also as sole binders. Due to their low or latent hydraulic activity and/or pozzolanic properties, alkali activation is required for the dissolution and solidification processes to happen at a reasonable timeframe. The term “alkali activated materials” covers all binder systems where the alkali metal source is used to activate a solid silicate precursor, such as natural pozzolans, fly ash or GGBS [6]. Among the alkali components, the most commonly utilised embrace alkali hydroxides, silicates, sulfates, carbonates and aluminates [7]. The idea of using alkali activated materials as competitive substitutes for cement originates from the work of Kühl, who patented his findings on alkali activation of vitreous slags in 1908 [8]. The broad and fundamental investigation on activation of slag was later performed by a Purdon in 1940s [9]. These studies opened the floodgates of the development of alkali activated materials technology in the twentieth century, having its heyday in the mid-1950s in Europe, in the former Soviet Union where professor Glukhovsky discovered so-called “soil cements” while working with low-calcium precursors [10]. Due to a prominent development of alkali activated materials technology on different continents, mainly from the 1970s onwards, the expertise in alkali-activated materials has been further developed, e.g., in Poland [11], enabling their worldwide utilisation [12], [13], [14], [15]. The wide range of the precursors and therefore, the variable properties of alkali activated materials led to the distinction of geopolymers among alkali activated materials [16]. Geopolymers are produced from low-calcium aluminosilicate precursors, enabling the formation of a pseudo-zeolitic silicate network structure. This highly coordinated structure renders unique properties of geopolymers, including fire-resistance, chemical resistance and capacity to encapsulate radioactive waste. However, to ensure a sufficient rate of the polymerization process, heat supply is necessary, which often becomes a technological barrier, as it enforces special accommodations and additional energy input [6].

New cementitious binders

The scarcity of currently applied supplementary cementitious materials and the market competitiveness dictate the trends in cement and concrete development. The attention is shifted towards the by-products with negative or very low market value, including biomass

ash, Municipal Solid Waste Incineration (MSWI) bottom ash, steel slag, non-ferrous slag, bauxite residue and waste glass (Fig. 1.1) [17]. Among them, steel slags (represented by Basic Oxygen Furnace (BOF) slag and Electric Arc Furnace (EAF) slag) have recently received considerable attention due to their highest worldwide availability.

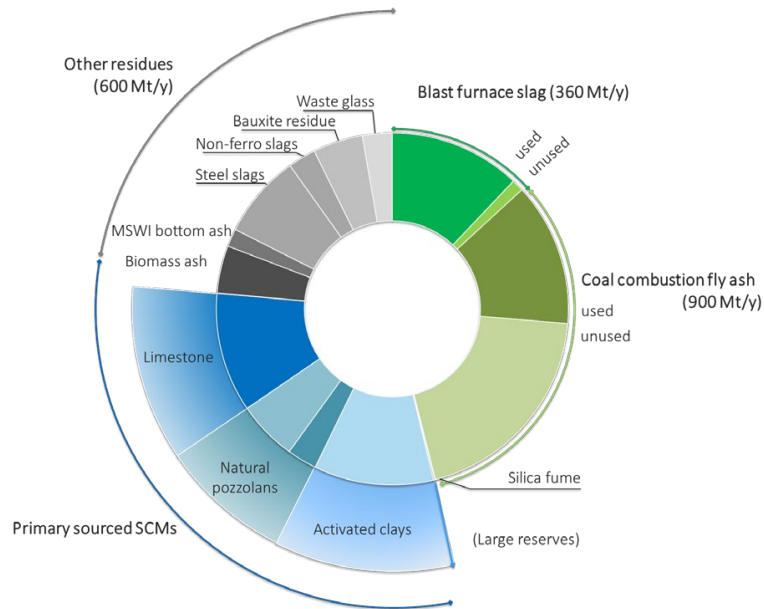


Figure 1.1: Currently utilised and potential supplementary cementitious materials [17].

The abovementioned by-products can be considered as potential cementitious binders. However, their utilisation is still very limited due to various technical challenges [18]. First and foremost, industrial residues often reveal variable and heterogeneous composition, which makes it difficult to standardise their use in concrete products. In view of the phase diversity, the promising benefits of new potential binders often require the assessment of physicochemical properties on the level of individual phases. In consequence, the commonly applied analytical techniques might not be sufficient or suitable for the analyses. Furthermore, in order to predict the long-term behaviour and durability aspects, the development of special evaluation methods is of significance since industrial residues are often contaminated with heavy metals or contain expansive components, including free CaO and MgO [4], [5].

Air purifying functionalized building materials

Concrete, with its wide applications, should not only be viewed as one of the main contributors to the CO₂ release. With recent development, it became apparent that by utilising advanced technologies, concrete offers enormous potential for capturing air

pollutants. The breakthrough technologies include the use of CO_2 to form calcite during the solidification of cementitious binders (so-called carbon capture, used, e.g., for belite cements, slags and fly ashes) as well as the functionalization of concrete surfaces to provide air-purifying properties [19]. The latter can be obtained through the application of photocatalytically active materials, e.g., nanotitania [20]. With nanotitania addition, large concrete surfaces become photocatalytically active, enabling oxidation of a variety of organic and inorganic pollutants, e.g., NO_x , SO_x , formaldehyde, etc. The oxidation process of NO and NO_2 results in the formation of nitrates, which can be removed with the rainwater from the active surfaces (Fig. 1.2) [21]. Since around 34% of NO_x emissions originate from road vehicles, air-purifying concrete pavements received special attention [22]. Several examples of this technology can be found in some countries, for instance, the Netherlands and Poland (Hengelo, Warszawa, Zielona Góra, Nowa Sól, Chorula and Boguchwała) [23].

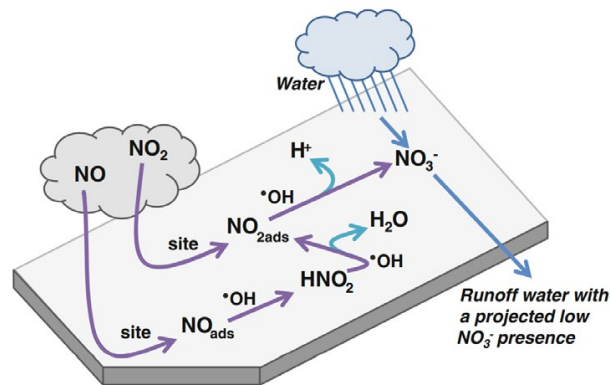


Figure 1.2: Photocatalytic oxidation of NO_2 and NO by the surface of TiO_2 -containing concrete pavement [21].

Nevertheless, despite the broad research interests on this topic, worldwide applications are still limited, mainly due to the concerns around the effectiveness of photocatalytically active surfaces under real outdoor conditions. The real scale projects often reveal discrepancies with the laboratory-scale simulations, where with well-defined parameters, superior photocatalytic performance is observed [24]. One of the reasons for these discrepancies is an insufficient accuracy of the photocatalytic efficiency monitoring, affected by a number of variables, including weather conditions, concentrations of pollutants but also durability of the photocatalytic material itself [22], [25], [26]. As shown in the study of Ballari [21], due to simple wearing, weather factors and/or depositions of the solids on the surface, the photocatalytic performance of TiO_2 -coated pavements dramatically drops over time. Therefore, before application in the field, durability aspects should be thoroughly

investigated e.g. by performing accelerated aging tests, to ensure sufficient lifetime of the photocatalytic product.

1.2 Scope and objectives

Intending to reduce the environmental impact of the cement and concrete industry, the objective of this thesis is threefold. As a point of departure, the work focuses on the improvement of existing eco-friendly technology (alkali-activated materials). Secondly, it offers a design of new alternative binders, and finally, investigates opportunities for air-purifying technology in concrete. These objectives are addressed within the following topics:

Ambient curing of silica-rich alkali-activated materials

Since silica-rich alkali activated materials require heat supply to ensure a sufficient reaction rate, special accommodations during their manufacture are needed. To overcome this issue, the addition of small quantities of cement is proposed. The impact of cement during the solidification processes in alkali-activated high-silica systems is evaluated.

BOF slag as a cementitious binder

Currently, the utilisation of BOF slag in the cement and concrete industry is insubstantial. One of the reasons for that is its very low early age reactivity. On the basis of phase composition, chemical activation of BOF slag with the use of citrate salts is proposed and evaluated. With the aim to further accelerate the hydration of BOF slag at the early ages, and consequently, to improve early strength development, the addition of nano-silica and its effect on the hydration rate of individual phases is investigated. Finally, the potential hazardous impact of the BOF slag-based products is examined upon accelerated aging conditions to reveal the feasibility of their industrial applications.

Durability of photocatalytically active mortars

Implementing TiO₂ nanoparticles in the concrete surface yields air-purifying properties. However, simple spraying of TiO₂ on the concrete surface can result in a short lifetime of the coating and pose a risk of release of the nano-sized particles to the surroundings, arising concerns around its safety. This risk is expected to be lower when nanoparticles are intermixed in the concrete surface layer. However, in this case, the physicochemical changes related to concrete aging, including progressive hydration and carbonation on the concrete surface, might affect their performance. The correlation between the initial mix design and

the photocatalytic performance before and after accelerated carbonation is proposed to predict and optimize the long-term performance of photocatalytic products.

1.3 Outline of the thesis

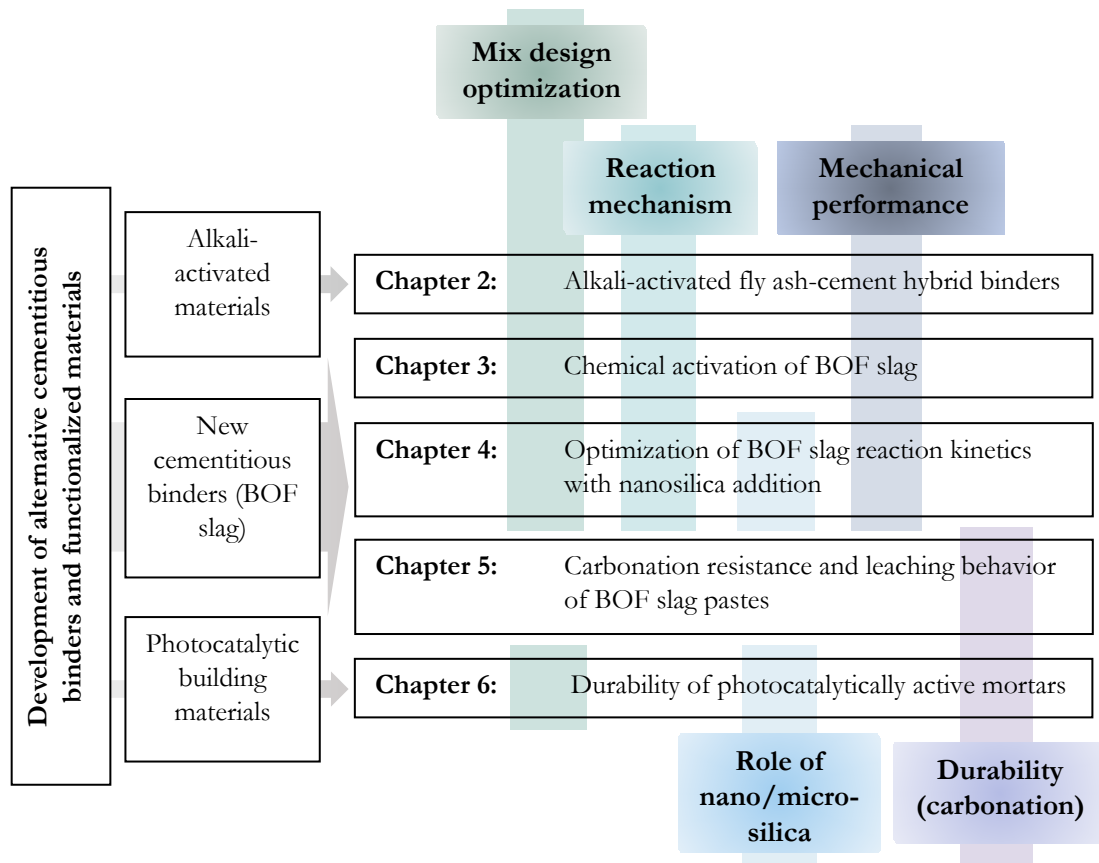


Figure 1.3: Outline of the thesis.

The outline of this thesis, schematically shown in Fig. 1.3, is as follows. In **Chapter 2**, the strategy to eliminate high-temperature curing of alkali-activated silica-rich materials is described. The effects of cement addition on the solidification processes and mechanical performance of the alkali-activated fly ash are analysed. In **Chapter 3**, BOF slag as a new alternative binder is introduced. The activation procedure applying citrate salt is proposed and investigated. Following, in **Chapter 4**, the early hydration kinetics of slag pastes and consequent strength development of BOF slag mortars are evaluated. The optimisation method for strength development is offered through nanosilica addition. Durability aspects of the BOF slag-based products, with the focus on post-carbonation leaching of heavy metals, are analysed in **Chapter 5**. In **Chapter 6**, the concept of photocatalytic technology in concrete is presented. The impact of the hydration products on the photocatalytic

response of mortars containing nanotitania is analysed. Furthermore, the link between the carbonation-induced compositional and microstructural changes and photocatalytic performance of mortars is discussed. In **Chapter 7**, the main conclusions from this thesis are provided, followed by the recommendations for future research.

Effects of Portland cement on the activation mechanism of class F fly ash geopolymer cured under ambient conditions

The need for high-temperature curing of geopolymeric systems creates a technological barrier and boosts production costs. In this chapter, the reaction kinetics and phase evolution of ambient cured alkali activated fly ash (class F)-Portland cement hybrid systems (with cement content up to 10 wt%) are investigated. The results show that setting time and reaction kinetics can be controlled by tailoring the precursor and activator characteristics, primarily the Ca/Si molar ratio. Calcium ions, dissolved from cement phases, contribute to faster precipitation of products and, consequently, to a denser microstructure of composite pastes and a higher mechanical performance at an early age. However, excessive cement contents impede the gel formation at later ages due to the limited overall reaction degree of cement in highly alkaline conditions and high intake of alkali and silica from activator in calcium-enriched early hydration products. It is found that the optimal dosage of cement in fly ash-based geopolymeric system depends on the total silica content, being equal to 5 wt% and 7.5 wt% for the mixtures containing sodium silicate with a silica modulus of 1.2 and 1.5, respectively.

2.1 Introduction

Over the last years, extensive research has been performed on geopolymeric binders. Duxson et al. [27] proposed a model based on the Si/Al atomic ratios in metakaolin-based geopolymers, linking the composition of the raw materials with the microstructure and mechanical properties of the products. This enabled tailoring the mix design for specific applications. Later, Criado et al. [28] disclosed the dependence between the activator characteristics and the phase assemblage in geopolymers. The applicability of geopolymers

Reproduced from:

Kaja, A. M., Lazaro, A., & Yu, Q. L. (2018). Effects of Portland cement on activation mechanism of class F fly ash geopolymer cured under ambient conditions. Construction and Building Materials, 189, 1113–1123.

in real conditions was analysed by Bakharev et al. [29], who investigated the effect of curing temperature on the microstructure and mechanical properties of fly ash-based geopolymers. A significant influence of thermal conditions on the performance of geopolymers as well as the link between the initial mix design and the optimal curing conditions were disclosed. Despite extensive research, there is limited number of full-scale geopolymer productions over the world. As was shown by Bakharev et al. [4], the external heat supply in order to ensure a sufficient rate of geopolymerization generates an additional variable in designing geopolymers. In contrast to alkali-activated calcium-rich systems, special accommodations must be applied in the production of geopolymers to provide the required amount of heat with a suitable method, especially for large concrete casting [30], [31].

Recently, special attention has been paid to alkali-activated systems consisting of fly ash and cement. These hybrid materials can be produced without thermal treatment while maintaining a high content of fly ash in the binder. It has been suggested that combining the geopolymeric binder with a calcium source hinders the formation of zeolites, which are found to have an adverse effect on the mechanical performance of geopolymers [32], [33]. Krivenko et al. [34] reported that in comparison to pure geopolymeric systems, they also possess better abilities to bind sodium ions, preventing efflorescence from occurring. At the same time, the content of the calcium source considerably influences the setting time of alkali-activated materials [35]. Due to the provision of additional nucleation sites for the precipitation of products, accelerated hardening occurs [36]. As calcium ions possess a similar ionic radius to sodium ions, they render the charge balancing function in the structure formation [37].

Due to the different nature of cement hydration and the fly ash geopolymerization process, the activation mechanism of hybrid systems is very complex. While investigating the phase assemblage and mechanical properties of a mixture comprising of 70 wt% of fly ash and 30 wt% of cement, Garcia-Lodeiro et al. [38] revealed that at the early activation ages, C-S-H and N-A-S-H gels are simultaneously formed. At longer hydration periods, C-S-H gel transforms into C-A-S-H gel, which is more thermodynamically stable in a highly alkaline environment. A similar transition is observed for N-A-S-H gel, which evolves towards (N,C)-A-S-H [39].

On the other hand, Yip et al. [40] proved that whereas a calcium source (cement, ground granulated blast furnace slag) with a dosage up to 20 wt% in hybrid systems can have a

positive impact on the mechanical performance of these materials, higher dosages (40 wt%) cause a decrease in compressive strength compared to the plain geopolymer samples (when pretreatment at elevated temperature is applied). Moreover, the studies of Nath et al. [41] and Suwan et al. [42] showed that at ambient conditions, the compressive strength of geopolymers could be considerably improved even with a small amount of cement addition (5-10 wt%). The mechanism behind this phenomenon remains unclear. Even though recent studies explored in-depth the compatibility between C-S-H and N-A-S-H gels in fly ash-cement systems as well as synthetic gels systems [38], [43], there is still a lack of knowledge regarding the influence of cement dosage on the formation of geopolymeric structure and accordingly mechanical performance of these materials.

In this study, the alterations in the geopolymerization process in the presence of a low amount of cement are addressed in detail. Mixtures with cement dosages up to 10 wt% and two different sodium silicate activator moduli are investigated in order to systematically understand the kinetics of the gel formation, characteristics of the formed phases and their interaction. The presented results provide fundamental insights into the greatly shortened setting behaviour and enhanced early age mechanical performance, which are critical parameters for the manufacture of these hybrid materials at ambient conditions.

2.2 Experimental

2.2.1 Materials

Class F fly ash (FA) and Ordinary Portland Cement (OPC) CEM I 42.5 N (provided by ENCI, the Netherlands) were used as solid precursors in this study. Their chemical composition, determined by X-ray fluorescence, is presented in Table 2.1. In order to minimize the effect of the particle size of the raw materials on the final performance of geopolymeric pastes, solid precursors with similar particle size distribution were selected, as presented in Fig. 2.1. The PSD was measured by laser diffraction (Mastersizer 2000, Malvern).

Table 2.1: Chemical composition of the raw materials.

Raw material	Mass fraction wt%											
	CaO	SiO ₂	Al ₂ O ₃	Fe ₂ O ₃	MgO	SO ₃	K ₂ O	Na ₂ O	TiO ₂	Mn ₂ O ₄	P ₂ O ₅	LOI
OPC	63.71	20.27	4.8	3.43	1.58	2.91	0.53	0.26	-	-	-	2.51
Fly ash	4.44	54.62	24.42	7.21	1.43	0.46	1.75	0.73	1.17	0.11	0.86	2.8

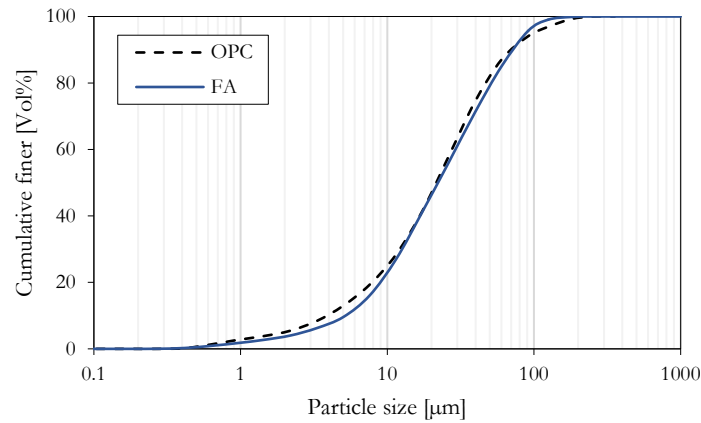


Figure 2.1: Particle size distribution of the investigated materials.

Two alkaline activators were prepared by mixing commercially available sodium silicate solution with analytical sodium hydroxide pellets and demineralized water and named in this study as M1.2 (19.7 wt% SiO₂, 16.9 wt% Na₂O, and 63.4 wt% H₂O) and M1.5 (24.4 wt% SiO₂, 16.8 wt% Na₂O, and 58.8 wt% H₂O). The equivalent sodium oxide content in both activators was kept constant (8 wt% of the binder). This level of alkali content has been proved to be optimal regarding the dissolution rate of low calcium fly ash [29], [44]. Skvara et al. [45] demonstrated that optimum compressive strength of fly ash-based geopolymers can be achieved when Na₂O content in sodium silicate activator ranges between 7 wt% and 9 wt% of fly ash. Similar observations were reported by Winnefeld et al. [46], who stated that the increasing Na₂O content up to 9 wt% of fly ash has a positive effect on the strength development of geopolymers, whereas higher dosages are not recommended (as reported for pastes with L/S (liquid to solid) ratio between 0.4 and 0.5). Another important feature characterizing the activator solution is the silica modulus (Ms), defined as the molar ratio between silicon oxide and sodium oxide. The content of silica in activating solution considerably influences the early age development of the geopolymeric structure. Rees et al. [47] proved that a silica concentration of approximately 0.6 M is sufficient to shift the reaction mechanism from hydroxide activation towards silicate activation. It has been widely demonstrated that silicate species readily available in the pore solution enhance the formation of a geopolymeric structure, resulting in a homogenous and dense microstructure of the final products [48], [49]. In this work, two silica moduli (Ms) of 1.2 (M1.2) and 1.5 (M1.5) were applied, based on the previous study [50].

2.2.2 Sample preparation and test methods

Alkali solutions were prepared and cooled down to room temperature (20 ± 1 °C) in the sealed containers one day prior to application. For compressive strength measurements, geopolymeric pastes were produced according to the mix design presented in Table 2.2. The liquid to binder ratio was kept constant as 0.5 for all the mixtures. Dry powders were firstly mixed for one minute in a Hobart mixer. Subsequently, the sodium silicate solutions were added to the homogenized solid precursors and mixed for another 4 minutes. Fresh pastes were cast into plastic molds ($40 \text{ mm} \times 40 \text{ mm} \times 160 \text{ mm}$) and covered with foil to prevent moisture loss. After 24 h of curing, samples were demolded (pastes based solely on fly ash were demolded after 3 days of curing) and sealed cured at room temperature of about 20 °C until the testing age.

Compressive strength and setting time

The compressive strength of all samples was determined according to EN 196-1 [51] after 7 and 28 days of curing, respectively. The average values were obtained from 3 measurements for each sample. The initial and final setting time measurements were conducted with a Vicat needle test setup according to EN 196-3 [52].

Table 2.2: Mix proportions of investigated geopolymeric pastes.

Mixture	Mass fraction wt%		W/B ratio**		L/B ratio**
	Fly ash	Cement	Activator		
			Ms = 1.2*	Ms = 1.5*	
P0M1.2	100	-	0.30		0.5
P5M1.2	95	5	0.30		0.5
P7.5M1.2	92.5	7.5	0.30		0.5
P10M1.2	90	10	0.30		0.5
P100M1.2	-	100	0.30		0.5
P0M1.5	100	-		0.28	0.5
P5M1.5	95	5		0.28	0.5
P7.5M1.5	92.5	7.5		0.28	0.5
P10M1.5	90	10		0.28	0.5
P100M1.5	-	100		0.28	0.5

*[OH⁻] recalculated from the pH values (measured with a Metrohm 780 pH Meter) were 0.955 M and 0.631 M for activators with silica modulus (Ms) 1.2 and 1.5, respectively.

**W/B is a mass ratio between water from activating solution (excluding Na₂O and SiO₂) and binder (fly ash + cement). L/B ratio is a mass ratio between activating solution (including Na₂O and SiO₂) and binder (fly ash + cement).

Isothermal calorimetry

The reaction kinetics of the investigated systems were determined with an isothermal calorimeter (TAM Air, Thermometric) at 20 °C. Powders were firstly mixed with sodium silicate solutions for 2 min and about 10 g of pastes were transferred to sealed ampoules that were then loaded into the calorimeter. To evaluate the cumulative heat, the integration of the heat flow curve was performed between 30 min and 140 hours.

Fourier transform infrared spectroscopy (FTIR)

The FTIR spectra of geopolymeric samples were collected using a PerkinElmer Frontier™ MIR/FIR Spectrometer with the attenuated total reflection (ATR) method (GladiATR). The analyses were performed on pastes without terminating the hydration during the first 28 days of activation. All spectra were scanned 50 times from 2000 to 600 cm⁻¹ at a resolution of 4 cm⁻¹.

X-ray diffraction (XRD)

The X-ray diffraction (XRD) analysis and thermogravimetric analysis (TGA) were carried out on powder samples. To stop the activation process, pastes were firstly crushed and immersed in isopropanol for 24 hours, then dried for 5 hours at 40 °C and ground. A D2 PHASER X-ray Diffractometer with a Co X-ray tube and a step size of 0.02° for a 2θ range of 10-50° was used to determine the phase composition of pastes.

Thermogravimetry

About 40-70 mg of powdered samples were thermally treated using a Jupiter STA 449 F1 Netzsch instrument. The samples were firstly isothermally held at 105° C for 2 hours and then heated up to 1000 °C at the rate of 5 °C/min with nitrogen as a carrier gas.

Scanning electron microscopy + Energy dispersive X-ray spectroscopy (SEM + EDX)

For the microstructure analysis, the activation process was stopped by immersing the paste specimens in isopropanol for 24 hours and subsequent drying in the oven at 40 °C for 3 days. Selected sections were sputtered with gold by using an Emitech K550X sputter coater (current 25 mA, coating time 2 min). The Phenom ProX scanning electron microscope (SEM) was used with an accelerating voltage of 15 kV. Point analyses were conducted on polished samples with the Element Identification (EID) software package with a fully

integrated Energy Dispersive Spectrometer (EDS) (more than 120 points were taken for each measurement).

2.3 Results and discussion

2.3.1 Setting behaviour

Table 2.3 shows the Vicat test results for designed mixes. Vicat test is universally accepted and utilised since the simple procedure allows to obtain satisfactory results when hydration of Portland cement is analysed [53]. It should be pointed out, however, that during the alkali activation, different mechanisms of stiffening and hardening take place. Therefore, considering the practical aspects of hybrid systems manufacture, it has to be taken into account that the properties of alkali-activated materials (e.g., mechanical properties, microstructure, reaction extent) at the setting point can differ substantially from the cement paste properties. Nevertheless, this test provides useful information about the hardening process taking place at the early activation stages.

Table 2.3: Setting behaviour of alkali activated pastes.

Mixture	Initial setting time [min]	Final setting time [min]
P0M1.2	> 24h	> 24h
P5M1.2	210	300
P7.5M1.2	130	180
P10M1.2	80	115
P0M1.5	> 24h	> 24h
P5M1.5	350	520
P7.5M1.5	190	300
P10M1.5	110	145

While samples based solely on fly ash are not able to set within 24 hours, the results show that even a very small amount of cement addition can considerably accelerate the setting. This behaviour has been also reported by others [41], [54]. Suwan et al. [54] suggested the addition of 5 wt% of cement in order to obtain reasonable setting times for practical applications of these materials. In the study of Yip et al. [40], the significant role of calcium ions at the early stages of alkali activation was emphasized by analysing the influence of different calcium sources in fly ash-based hybrid systems. Similarly here, calcium ions dissolved from the cement

phases greatly contribute to the hardening process. The present study additionally reveals that next to the cement content, the $\text{SiO}_2/\text{Na}_2\text{O}$ molar ratio of the activator significantly influences the setting behaviour. Whereas the increasing cement content accelerates the hardening process of highly alkaline low-calcium systems, the setting time is substantially prolonged with a higher silica concentration in the alkaline solution. Due to the exothermic nature of cement hydration, the additional reaction heat can also contribute to the faster setting of these binders.

The accelerating effect of cement addition on the setting time can be explained by the presence of calcium ions, which pose a significantly higher charge screening capacity of the silicic acid anions than sodium ions [55]. It is known that in a highly alkaline environment, negatively charged silicic acid monomers will repulse each other, preventing condensation [56]. Calcium ions can therefore accelerate the formation of products due to the charge neutralization effect. Gaboriaud et al. [57] suggested that the presence of calcium ions in the sodium silicate solution leads to the aggregation and subsequent densification of the gel network. In a high pH environment, however, their effect is rather associated with precipitation of calcium-silica products than gelation.

2.3.2 Reaction kinetics

Fig. 2.2 shows the heat flow profiles and cumulative heat curves of the designed systems (normalized to the mass of binder (fly ash + cement)). Regardless of the activator modulus, the heat flow curves of pastes based solely on fly ash do not reveal any peaks, which could be associated with the formation of products. With the presence of cement in the mixtures, the influence of the activator characteristics becomes more significant. For the samples activated with sodium silicate solution with a silica modulus of 1.2, an additional peak occurs between 2 and 6 hours. This peak is attributed to the precipitation of products. With the increasing cement content, the position of this peak shifts towards shorter times and its intensity rises. This behaviour is consistent with the setting time observations. Most likely, C-S-H-like structures are formed in these systems as a consequence of the reaction between calcium ions dissolved from cement phases and silica. On the contrary, no “main reaction peak” can be distinguished in the hybrid systems activated with sodium silicate solution with a silica modulus 1.5 (Fig. 2.2c). These observations are attributed to the higher concentration of silica ions and a lower concentration of OH^- in the activator of $[\text{OH}^-]$ of 0.631 versus 0.955 molL^{-1} . Therefore, it is likely that due to the high availability of silica ions, and lower

pH, condensation of silica species is a dominant process in this system (as observed for geopolymers).

To broaden the spectrum of information related to hydration of cement in highly alkaline conditions, calorimetric measurements were also conducted on the neat cement samples.

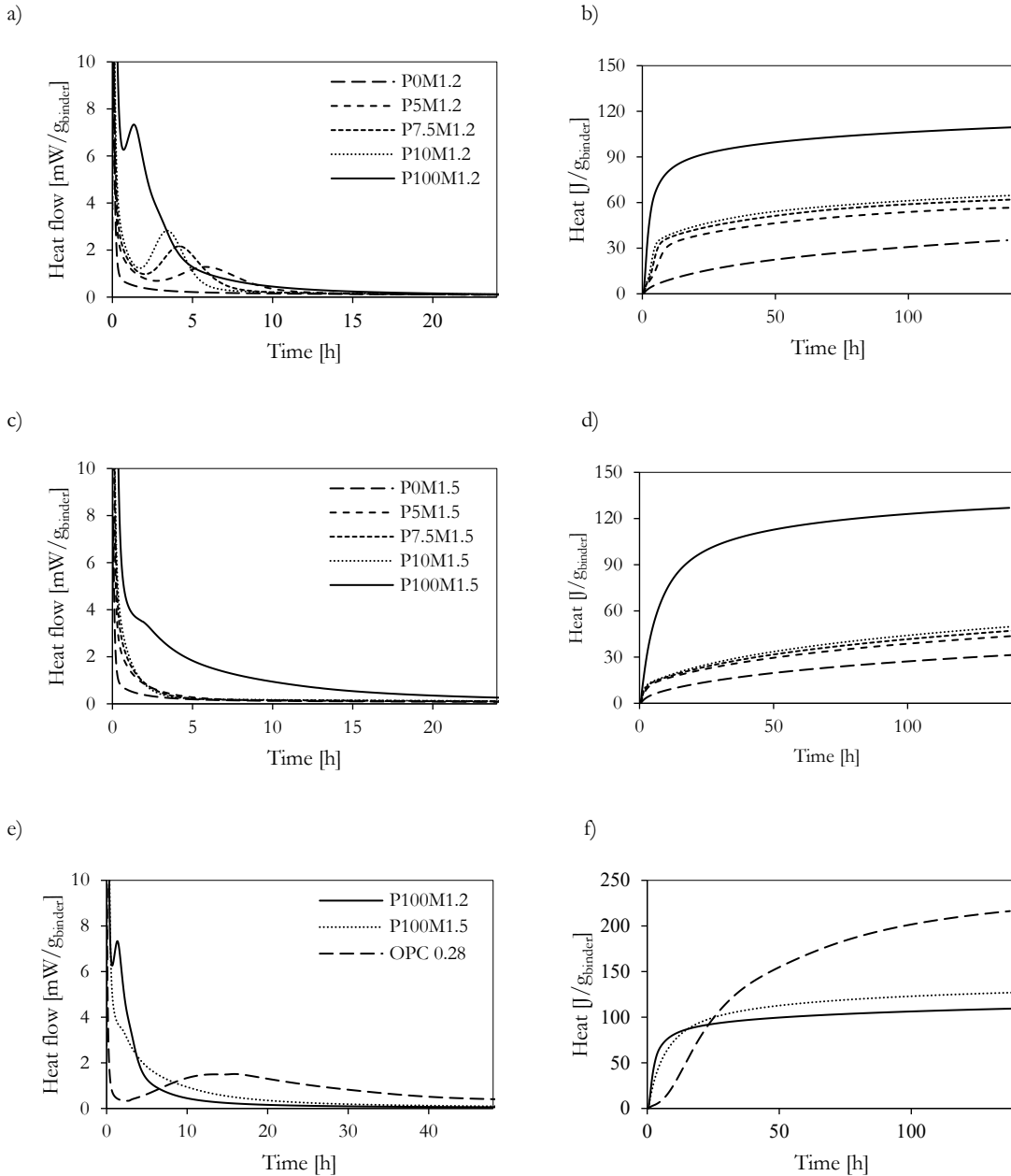


Figure 2.2: Normalized heat flow a), c), e) and total heat b), d), f) curves of alkali activated pastes (note: additional water hydrated cement paste was prepared for comparison purpose, described as OPC 0.28, where 0.28 is the water to cement ratio). Binder is defined as fly ash and cement.

Figs. 2.2e and 2.2f show the heat flow profile and cumulative heat of cement hydration with alkaline activators and water as a reference (selected $w/c = 0.28$ corresponds to w/c ratio of the alkali activated cement sample with an activator modulus 1.5), respectively. It can be seen that cement hydration is considerably accelerated in highly alkaline conditions. Due to the high pH of the used activators and the presence of silica species, the induction period is eliminated. However, the overall heat release by the end of 140 hours of curing is considerably higher in the case of cement with only water. It is concluded that hydration of cement in highly alkaline conditions is accelerated during the first few hours of curing while is drastically inhibited at later ages. Comparing the hydration curves of cement activated with solutions with a silica modulus of 1.2 and 1.5, similar conclusions can be drawn. The higher amount of heat generated at the beginning of the activation process in the sample activated with solution M1.2 results in a lower reaction degree of cement up to 140 hours than in the sample with M1.5 solution.

2.3.3 Infrared spectroscopy analysis of the activation process

The fly ash FTIR spectrum consists of vibrational bands assigned to both glassy and crystalline phases. In order to account for a large spectrum of component bands from the raw materials as well as reaction products, in this study, a straightforward approach is applied based on the identification of the “main” band position in the region $1100\text{-}800\text{ cm}^{-1}$, attributed to Si-O-T bond asymmetric stretching vibrations ($T = \text{Si, Al}$). It has been well documented that the shifts in the position of this band indicate structural changes of investigated materials, especially the polymerization degree of the silica network [58]. From Fig. 2.3a it can be seen that the band assigned to T-O stretching vibrations in the fly ash spectrum shows a broad peak at around 1033 cm^{-1} . This peak consists of a group of bands assigned to the quartz, mullite, and glassy phase. The location of the major vibrational band at low frequencies- around 1033 cm^{-1} indicates a relatively high amorphous content of fly ash used in this study [58], [59]. In dry cement, the position of the main peak is considerably shifted towards lower wavenumbers due to the different nature of the main phases. The band located at around 915 cm^{-1} is assigned to crystalline calcium silicates [60].

Two sodium silicate solutions used in this study characterized by different silica and water contents were also examined by FTIR. Previous studies on sodium silicate solutions have shown that the position of the main bands is determined by the molecular weight of units formed in the solution [61], [62]. Larger silicate structures contribute to the bands at higher

vibrational frequencies. It is also known that the size of the structural units increases with the increasing silica modulus and decreasing pH [63], [64]. In this study, both activators exhibit very high pH (see Table 2.2); hence the main peaks occur at relatively low wavenumbers, attributed to small silicate units. The infrared spectrum of these highly alkaline solutions is dominated by two-component bands near 975 and 921 cm^{-1} . Their presence is assigned to the vibrations of small linear silicate species (dimer, trimer, tetramer) and monomeric and dimeric silicate species, respectively [65]. The fact that the position of the main peak is only slightly changed for activators with different silica modulus indicates that in high alkalinity, small silicate species are dominant and only a small amount of slightly larger units can be observed in solution with a higher silica modulus. Rees et al. [49] also reported that the higher the pH of the solution, the higher silica concentration can be used to maintain the monomeric nature of silicate species. It has to be mentioned, however, that larger silicate units (oligomers) can also be present in the investigated solutions, but they are not distinct in this study due to overlapping of bands. The silicate monomers and small species (short chains) are found to participate in the dissolution process of fly ash and enhance the attainment of steady gel [49].

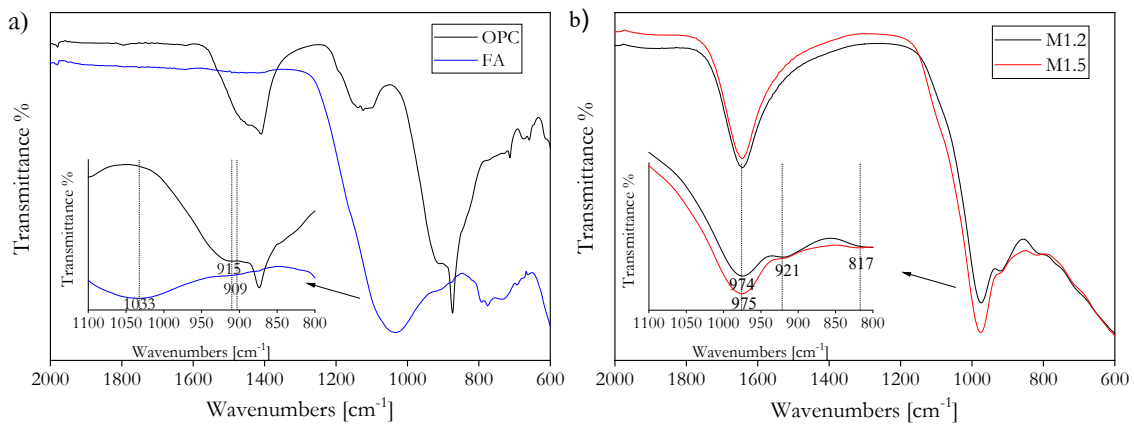


Figure 2.3: FTIR spectra of a) fly ash and cement, b) sodium silicate solutions.

The FTIR spectra of the investigated samples were collected after scheduled curing periods without any mechanical or chemical intervention in the activation process. Therefore, the analogy of the spectra shape and peak positions of early age samples spectra and spectra of sodium silicate solution used to activate samples is observed. For samples based solely on fly ash, a shift in the position of the main peak at around 973-975 cm^{-1} towards lower wavenumbers can be observed during the first 24 hours of curing. The rate of this shift seems to be not influenced by the initial silica content in the activator. Changes in the main

peak position are mainly attributed to the dissolution of fly ash, resulting in the occurrence of silica and alumina species in the solution (depolymerisation). The shift of the main peak towards higher wavenumbers observed between 24 h and 7 days is attributed to the formation of the gel network. The peak is shifted towards higher wavenumbers for the sample with higher initial availability of monomeric silica, which can promote the formation of a three-dimensional structure [66].

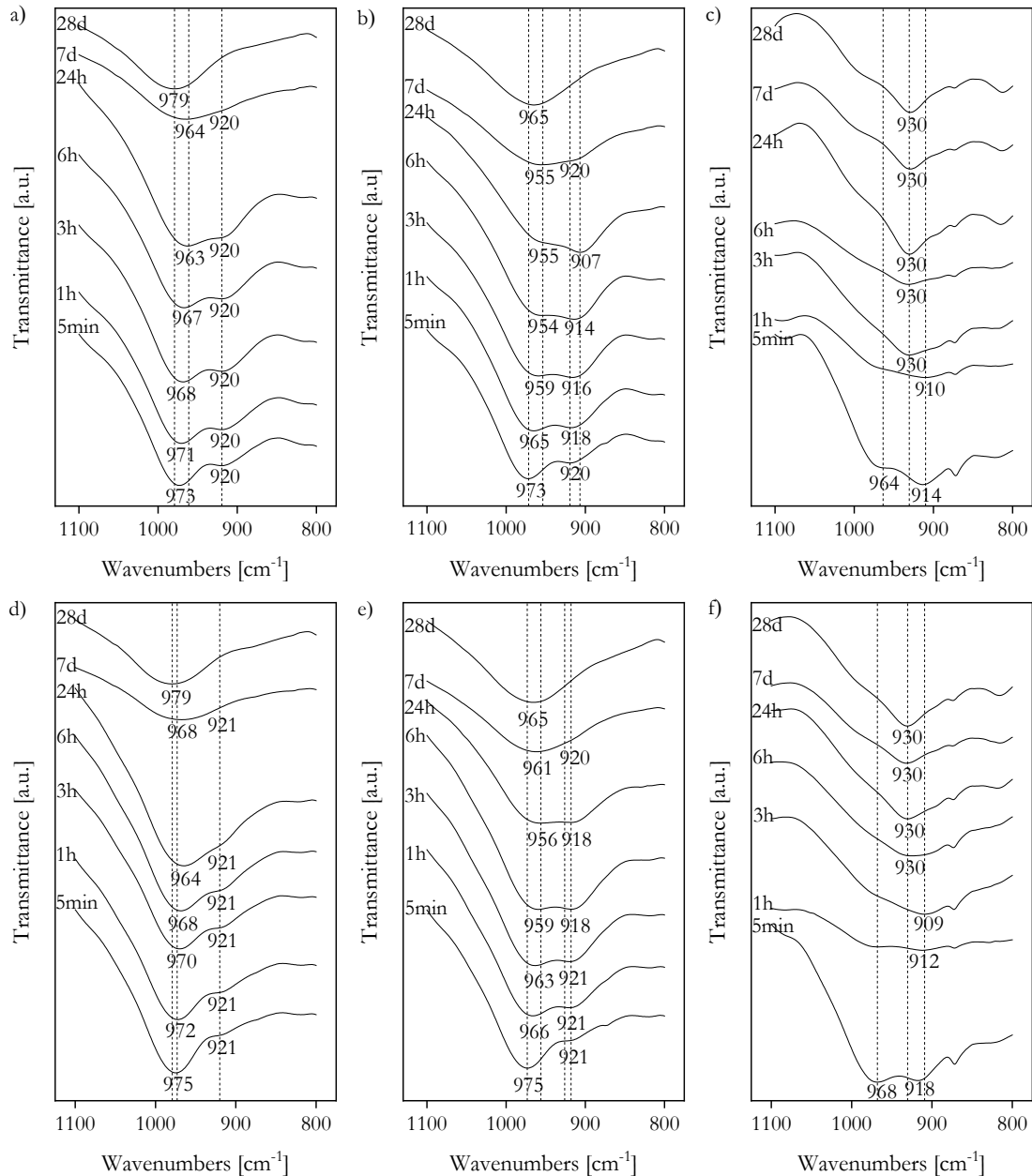


Figure 2.4: FTIR spectra of the geopolymeric pastes during activation process a) P0M1.2, b) P10M1.2, c) P100M1.2, d) P0M1.5, e) P10M1.5, f) P100M1.5.

Nevertheless, after longer curing periods (28 days) the position of the main peak becomes stable, regardless of the used activator. The influence of silica from activator becomes less prominent at later ages due to a considerably higher contribution of the silica from fly ash in products.

For hybrid systems, similar behaviour in the main peak position can be observed. However, the shift of the main band towards lower wavenumbers during the first hours of activation is more significant. The reason for this phenomenon most likely lies in the fact that another band at around 920 cm^{-1} becomes dominant. From the studies of Taylor [67], Zhang et al. [68] and Zhang et al. [69], it appears that the band located in the region $900\text{-}920\text{ cm}^{-1}$ reflects the stretching of Si-O(M, Fe) bond, where M is an alkali metal or an alkali earth metal, or Si-OH. Therefore, this behavior can indicate the formation of “primary” C-S-H phases in the presented systems, which is in line with the calorimetric measurements (Section 2.3.2). This conclusion can be further confirmed by analyzing the position of this band in sole cement-based samples (Figs. 2.4c and 2.4f). During the first few hours of activation, shifts towards lower wavenumbers (around 910 cm^{-1}) can be observed. Subsequently, after 1 hour for the sample with a lower initial silica content, and after 3 hours for the sample with a higher initial silica content, a shift towards higher wavenumbers occurs. In both cases, however, during the activation process up to 28 days, spectra are dominated by the peak at around 930 cm^{-1} , originating from unreacted phases, which confirms the limited reaction of cement in a highly alkaline medium. Differences in the rate of C-S-H phase formation with varying initial silica content in cement samples are also reflected in composite samples. Changes in the peak position for samples with a lower silica content reflect changes observed during cement activation (C-S-H precipitation), whereas in samples with higher silica dosage, the formation of C-S-H-like structures is hindered, and the mechanism of the activation process is closer to geopolymerization.

2.3.4 Microstructure

Since the previous methods show that cement addition has significant influences on the structure formation of alkali-activated fly ash-based samples, especially during the first day of the activation process, SEM images were collected from the representative samples after 24 hours of curing (Fig. 2.5). Comparison between samples based solely on fly ash, with 10 wt% of cement and based solely on cement, demonstrates densification of the structure with the increasing cement content (the cracks observed in the samples are believed to be caused

by sample preparation or the applied drying procedure). Accelerated hydration of cement in high alkalinity contributes to the substantial increase in the amount of formed products.

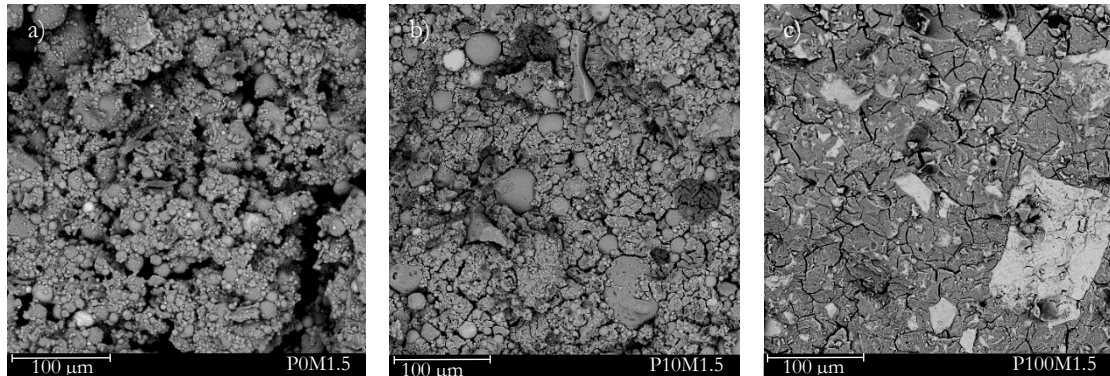


Figure 2.5: SEM micrographs of a) P0M1.5; b) P10M1.5 c) P100M1.5 after 24 hours of curing.

Based on these observations, the chemical characterization of the alkali activation products in the hybrid systems with 10 wt% of cement was performed (see Fig. 2.6a). Polished sections of the gel surrounding unreacted cement particles were examined with EDX point analysis.

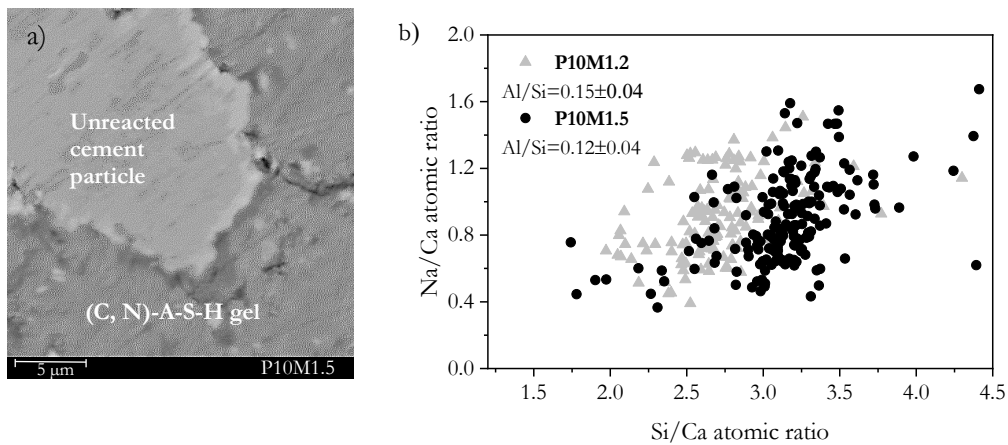


Figure 2.6: a) Backscattered electron image of the cement particle surrounded by main activation product after 24 hours of curing of the sample P10M1.5; b) Atomic Na/Ca versus Si/Ca ratios of the gel surrounding cement particles in hybrid samples after 24 h of activation.

Fig. 2.6b displays the plot of the Si/Ca atomic ratio against Na/Ca atomic ratio for gels in hybrid samples activated with sodium silicate solutions with silica moduli M1.2 and M1.5. After 24 hours of activation, the chemical composition of gels significantly varies. Nevertheless, the graphical display of atomic ratios enables defining the range of their chemical composition. To provide representative statistical information, 15 sections were investigated and from each section, 8 points were measured, resulting in 120 points (see Fig

2.6). All measurements were performed on the cracks-free areas. As expected, a higher silica content from the activator contributes to its higher content in the gel. This phenomenon is proven not only with the higher Si/Ca atomic ratio but also with the lower Al/Si atomic ratio in the sample with higher initial silica content. The phases exhibit an Al/Si atomic ratio of 0.15 and 0.12 for P10M1.2 and P10M1.5, respectively. At the same time, the Na/Ca atomic ratio remains similar regardless of the activator used, which correlates well with the fact that the same amount of Na₂O was introduced to the mixtures with both activators. These observations strongly suggest that calcium ions dissolved from the cement phases react mainly with silica species initially present in the pore solution. In general, it should be noticed that an intake of alkalis and silica from activator into these calcium-rich gels is very high. The Na/Si ratio ranging between 0.25-0.45 is substantially higher than the values of around 0.1-0.3 observed in the literature for N-A-S-H gels when similar activators were applied to activate fly ash [70], [46]. The products are also more abundant in alkalis compared to calcium-containing (N,C)-A-S-H gel with intervals of $0.0 \leq \text{CaO/SiO}_2 \leq 0.3$, $0 \leq \text{Na}_2\text{O/Al}_2\text{O}_3 \leq 1.85$, and $0.05 \leq \text{Al}_2\text{O}_3/\text{SiO}_2 \leq 0.43$ [38]. On the one hand, the high silica content in these gels suggests a higher polymerization of silica than in C-S-H phases and, therefore, better compatibility with N-A-S-H gels (three-dimensional structure of products should be maintained). On the other hand, however, the high uptake of silica and alkalis limits their availability for the formation of N-A-S-H structure.

2.3.5 Phase characterization

Fig. 2.7 shows the XRD patterns of pastes after 28 days of activation together with the patterns of the raw materials. The XRD analyses reveal that at ambient conditions, mostly amorphous phases are formed during the activation of fly ash, cement, and composite samples. The formation of amorphous products, which in geopolymers is associated with the N-A-S-H phase, is reflected in a hump between 20-40°, occurring at slightly higher values than the hump due to the amorphous phase in unreacted fly ash [60].

The XRD patterns of alkali activated cement samples show that after 28 days of curing, no crystalline portlandite is detected among hydration products. The remaining strong reflections from the alite phase confirm the limited hydration of cement after the accelerated hydration period, as reported in Section 2.3.2. Traces of monocarbonate are observed in cement-based samples, in line with the XRD measurements and phase modeling performed by Alahraiche et al. [71] on fly ash-cement composites hydrated in the presence of alkalis. As

ettringite has been reported to destabilize at high pH [71], this phase is not detected among the products. Sulphate ions are most likely bound within the amorphous C-S-H phase, as suggested by Richardson et al. [72], who investigated alkali activated cement with 30 wt% of fly ash substitution.

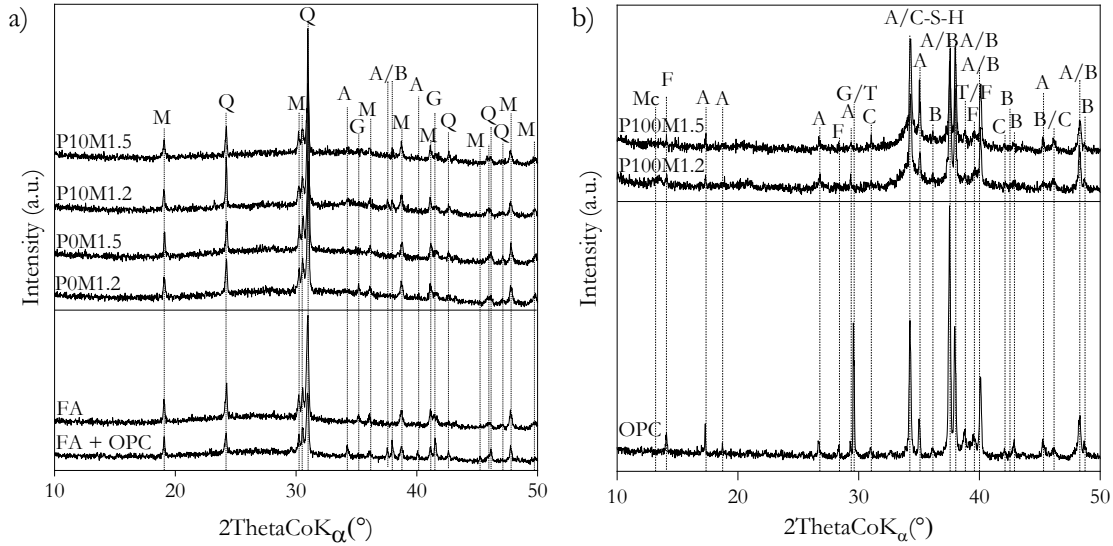


Figure 2.7: XRD diffractograms of the raw materials and activated samples a) fly ash and fly ash-cement-based pastes, b) cement-based pastes after 28 days of curing. Legend: Q - quartz, M - mullite, H - hematite, A - alite, B - belite, T - tricalcium aluminate, F - ferrite, G - gypsum, C - calcite, Mc - monocarbonate, C-S-H - calcium silicate hydrate.

The amorphous products formed during the alkali activation consist of evaporable water present in large pores (which should be removed during arresting hydration with isopropanol), loosely bound water, and tightly bound water absorbed in small pores or existing as a condensed hydroxyl group on the surface of the gel [48]. Therefore, to examine the gel formation in investigated systems, thermogravimetric analysis was performed (Fig. 8). The initial idea was to distinguish the products with loosely and tightly bound water which give a peak in the range of 50-200 °C, by applying an isothermal holding at 105 °C for 2 h during the heating process. It appears, however, that regardless of the chemical composition of the starting materials, the weight loss peak occurs at a similar temperature in all alkali activated systems. The TG curves show that more water is trapped/ bound in the cement samples compared to fly ash-based samples after 7 and 28 days of curing. This observation implies a greater ability of C(N)-S-H products to bind water. Analogously, in composite samples, more water is bound after 7 days of curing (weight loss observed in the temperature range of 105-250 °C) than in sole fly ash based samples, indicating faster

precipitation of products or/and different nature of calcium-rich phases, which are able to bind water more strongly. After 28 days, however, no substantial difference can be observed between the amount of bound water in neat fly ash samples and hybrid samples when 10 wt% of cement is used. Therefore, it can be concluded that the presence of calcium-rich products has no significant effect or even harmful effect (considering the greater ability of calcium-rich products to bind water) on the structural development of geopolymers at later ages. This effect is more prominent in the samples with lower initial silica content in the pore solution, where the formation of products with higher C/S was reported, implying the incompatibility of the gels formed. The harmful effect of cement on the formation of geopolymeric structure at later ages can be caused by a high intake of sodium ions into calcium-rich products formed at the beginning of the activation process, as was shown by EDX point analysis.

Next to the presence of cement in geopolymeric systems, the $\text{Na}_2\text{O}/\text{SiO}_2$ molar ratio in the activator highly influences the water-binding properties of these materials. A higher amount of water is bound in samples prepared from alkali solution with a higher silicate modulus, and a weight loss occurs at slightly higher temperatures, regardless of the presence of cement. Therefore, it can be concluded that more products are formed in these systems during the investigated curing periods or/and the products exhibit higher density, trapping a higher amount of water in their structure.

The analyses of cement-based samples also indicate that after 7 days of curing, the hydration of cement is very limited, as the weight loss remains almost the same for up to 28 days. Small amounts of portlandite are detected in cement samples after 7 and 28 days of hydration, which could not be observed with the XRD technique due to detection limits or low crystallinity of portlandite formed. The position of the weight loss peak assigned to portlandite dehydroxylation depends on the activator characteristics and the age of the samples and ranges between 407-430 °C. Considering that samples were cured and stored under controlled sealed conditions, a significant extent of carbonation is not expected to occur. Therefore, the presence of a weight loss peak at temperatures between 500 and 750 °C assigned to calcium carbonates in neat cement samples is likely derived from the raw material [73].

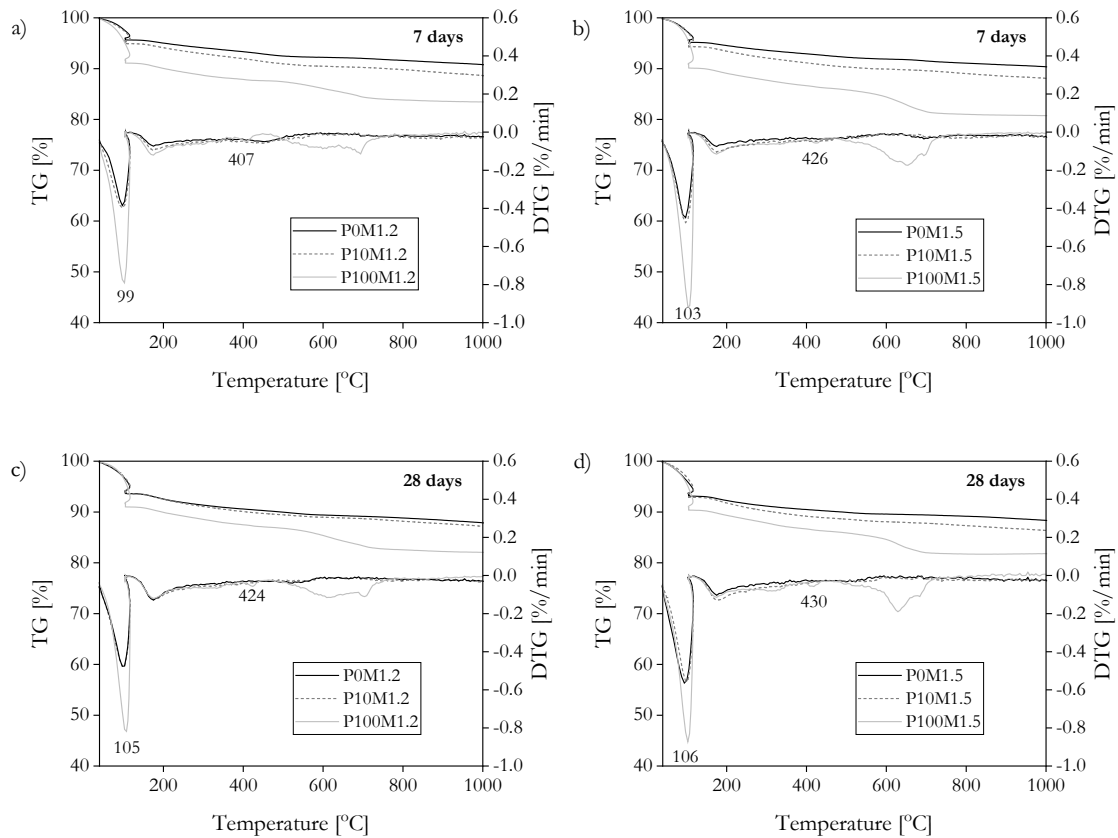


Figure 2.8: Mass loss (TG) and derivative mass loss (DTG) curves for alkali activated pastes.

2.3.6 Mechanical performance

The 7 and 28 days compressive strength of geopolymers and geopolymer composites with Portland cement are presented in Fig. 2.9. In general, it can be seen that samples with higher initial silica content in the activator fluid exhibit better mechanical performance at investigated periods, which is in line with the FTIR and thermal analyses. Next to the higher silica content, cement addition also has a positive effect on the mechanical performance of the investigated samples. Even a very small amount of cement in the binder (5 wt%) enables a dramatic increase in the 7-days compressive strength, exceeding 200 % of the values for samples based solely on fly ash.

Tailby et al. [74] assumed that in alkali-activated hybrid halloysite-cement systems cured at elevated temperatures, the competition for silicon between C-S-H and geopolymeric products occurs. Consequently, the too fast formation of the geopolymeric structure hinders cement hydration. From the present study, it appears, however, that at ambient conditions formation of calcium-rich phases is favored at the beginning of the activation process and, as a

consequence, cement highly contributes to the strength development. Nevertheless, after longer curing periods (28 days) mechanical performance of geopolymeric samples is negatively affected by the excess calcium source. Even though the compressive strength of all the samples with cement addition is higher than the reference, the rate of strength development appears to decrease with increasing cement content. It can be therefore concluded that cement addition into alkali activated fly ash-based binder has positive effects on the early-age strength development, while the amount has to be determined with caution as otherwise the long-term performance can be expensed. In this study, an optimal amount of 7.5 wt% when the activator solution M1.5 is applied and around 5 wt% with the solution M1.2 was found. Yip et al. [40] suggested that the decrease in compressive strength can be attributed to the local alterations in the Si/Al ratio caused by the leaching of Si and/or Al between calcium-rich and calcium deficient products to obtain equilibrium in the system (which might cause local depolymerisation). The present study concludes that the strength development decrease can be caused by the inhibited hydration of cement in highly alkaline conditions after 7 days of curing. Moreover, the presence of calcium-rich phases has been found to retard the structural development of hybrid binders at later ages.

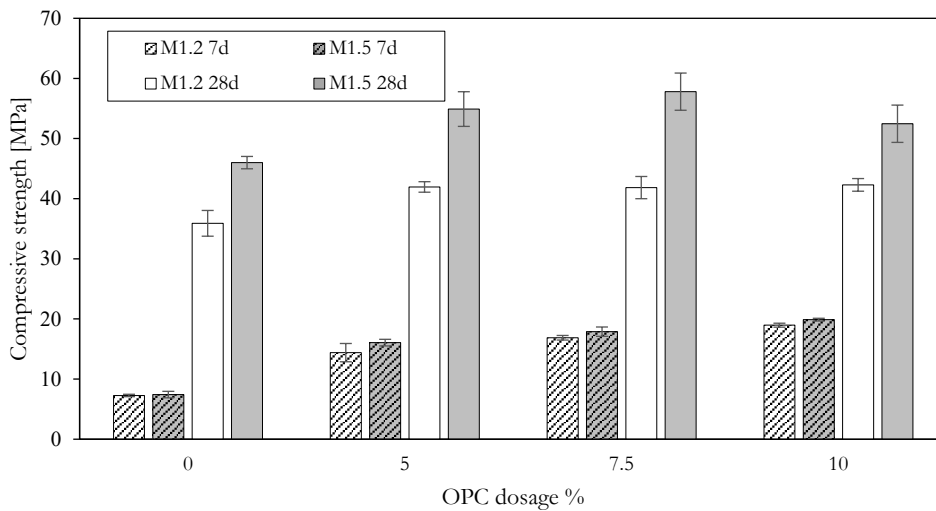


Figure 2.9: Compressive strength of geopolymeric pastes after 7 and 28 days of curing.

2.4 Conclusions

This chapter focuses on the reaction kinetics and phase evolution of alkali-activated fly ash-cement hybrid systems with varying cement content and activator molar ratio ($\text{Na}_2\text{O}/\text{SiO}_2$). Characterization of setting behaviour, activation heat, phase development, and subsequent

evaluation of the influence of these parameters on the mechanical performance was carried out by applying various techniques, including Vicat setting, isothermal calorimetry, FTIR, TG, XRD, SEM, EDX and strength tests. Based on the obtained results, the following conclusions are reached:

- Setting time of alkali activated hybrid fly ash-cement systems is considerably accelerated due to the presence of cement (5-10 wt%) and can be tailored by modifying the cement dosage and activator modulus. Retarding effect observed with increasing the silica content from the activator becomes more remarkable in the hybrid systems.
- Within 24 hours of the activation process in hybrid systems, the formation of calcium-rich gel phases is observed. These phases are characterized by a high intake of alkalis and silica.
- Kinetics of the calcium-rich gel formation is found to decrease with a higher silica content that leads to prolonged setting times. The higher initial content of silica results in the formation of (N,C)-A-S-H gel with lower Ca/Si and Al/Si atomic ratios.
- In alkali activated hybrid fly ash-cement systems with 10 wt% of cement content, only amorphous products are formed up to 28 days of ambient temperature curing. In samples based solely on cement, traces of monocarbonate are detected.
- Between 7 and 28 days of activation, the harmful impact of calcium-rich products on the gel formation is observed. This phenomenon is likely caused by the high intake of alkalis and silica into the early-age (N,C)-A-S-H gel, inhibited hydration of cement in high alkalinity, and incompatibility of the gels formed at different activation stages.
- The cement addition shows beneficial effects on the early age mechanical performance of geopolymers. All the hybrid mixtures investigated in this study exhibit better mechanical performance than pure fly ash samples after 7 and 28 days of hydration. 5 wt% and 7.5 wt% of cement content are recommended for hybrid fly ash-cement mixtures activated with sodium silicate solution with silica modulus of M1.2 and M1.5, respectively.

Hydration of potassium citrate-activated BOF slag

Basic Oxygen Furnace (BOF) slag is currently utilized with low-grade applications or landfilled. In this chapter, a novel route to upgrade BOF slag to a high-performance binder by chemical activation with tri-potassium citrate is investigated. The impact of tri-potassium citrate on hydration kinetics and phase assemblage of BOF slag is analysed with a multi-technique approach. Results reveal that the addition of tri-potassium citrate considerably enhances the reactivity of brownmillerite and accelerates the hydration of belite at early ages. The majority of brownmillerite hydrates within 24 hours, and the reaction kinetics is controlled by the activator dosage. The main products of BOF slag hydration are siliceous hydrogarnet and C-S-H gel. Acting as a strong water reducer, tri-potassium citrate enables the manufacture of slag pastes with high compressive strength (up to 75 MPa at 28 days) and low porosity. Moreover, the leaching of heavy metals from the slag pastes fulfills the Dutch Soil Quality Decree limits.

3.1 Introduction

Basic Oxygen Furnace (BOF) slag is a by-product of the conversion of iron to steel during the Linz-Donawitz process, and therefore, also called LD slag or converter slag [75]. Around 90-110 kg of BOF slag are generated per ton of steel produced, resulting in the annual production of BOF slag of about 10.4 million tons in Europe [76], [77], [78], [79]. The BOF slag is composed of CaO (30-50 wt%), SiO₂ (10-20 wt%), Fe₂O₃ (20-40 wt%), Al₂O₃ (1-7 wt%), MgO (4-10 wt%), MnO (0-4 wt%), P₂O₅ (1-3 wt%) and TiO₂ (0-2 wt%) [80], with a mineral assemblage of C₂S, C₃S, C₂(A,F), RO phase (CaO-FeO-MgO-MnO solid solution, crystallized in wuestite structure), and free lime (CaO) [76], [81], [82]. Despite the presence of C₂S/C₃S and C₂(A,F) phases, the hydraulic activity of the slag tends to be rather low,

Reproduced from:

*Kaja, A. M., Schollbach, K., Melzer, S., van der Laan, S. R., Brouwers, H. J. H., & Yu, Q. (2021). Hydration of potassium citrate-activated BOF slag. *Cement and Concrete Research*, 140, 106291.*

which hinders its application as a binder constituent [83]. The utilization of BOF slag in concrete is further limited due to the volume instability problems caused by the presence of free CaO [84] and the contamination with heavy metals [85] (especially vanadium and chromium [76], [86]).

Since C_3S is only a minor component of BOF slag (typically 0-5 wt%) [76], up to now, researchers have been mainly focusing on the activation and hydration of C_2S - the most abundant phase in the BOF slag (40-55 wt%) [87]. The C_2S phase (belite) appears in BOF slag as α' and β polymorphs. Without any treatment (physical or chemical), the early age hydraulic activity of belite is very low. The activation of BOF slag with conventional alkaline activators (like NaOH) as well as other admixtures, including $CaCl_2$, NaCl, Na_2SiO_3 , high alumina cement, and commercial accelerator, has been shown to only slightly affect the hydration of BOF slag [87], [88]. One possible reason is the stabilization of belite in the presence of impurities (Fe^{3+} , P^{5+}) [84], [89]. The impurities tend to decrease the reactivity of C_2S , and this effect is particularly visible with the high concentration of the contaminants [90].

Contrary to belite, limited attention has been paid to the second most abundant hydraulic phase in BOF slag - brownmillerite, also called srebrodolskite (~20 wt%). Whereas the hydration of belite in Portland cements contributes mainly to the late strength development (beyond 28 days), the dissolution and hydration of brownmillerite occur simultaneously with tricalcium aluminate, leading to the rapid formation of the products such as Fe-containing AFm phases and hydrogarnets [91], [92]. The extent of brownmillerite reaction is, however, significantly lower than that observed for C_3A [93]. In cement, the composition of the brownmillerite can be close to C_6A_2F but, in general, tends towards C_6AF_2 or even C_2F [94]. With an increased iron content, the reactivity of brownmillerite decreases [95]. In consequence, the hydraulic activity of brownmillerite in Fe-abundant and Al-deficient BOF slags is expected to be low. Schwarz [96] postulated that the dissolution of brownmillerite can be enhanced with the addition of citrate salts - where citrate is assumed to act via surface complexation and ligand-promoted dissolution. The formation of stable citrate complexes with iron has also been reported previously [97]. However, in the study of Möschner et al. [98], while using citric acid (up to 0.5 wt%), no experimental evidence for this phenomenon was observed. Instead, the sorption of the citrate species on the clinker surface was suggested. Nevertheless, the effect of potassium citrate - a basic salt, compared to citric acid,

can differ substantially since the behavior of citrate species as well as the dissolution rate of cementitious phases strongly depend on the pH [99], [100].

This chapter presents a novel, Portland cement-free, high-performance binder made from BOF slag and tri-potassium citrate monohydrate that plays a dual role of superplasticizer and activator of iron-containing phases. The influence of the tri-potassium citrate dosage on the phase development, microstructural and mechanical properties of BOF slag pastes is investigated using a multi-technique approach, based on quantitative XRD analysis, in-situ XRD, SEM/EDX large area phase mapping combined with PhAse Recognition and Characterization (PARC) software, thermogravimetric analysis, calorimetric measurements, porosimetry (MIP) and mechanical performance testing. In addition, leaching tests are performed on the final products in order to evaluate the environmental impact and, consequently, the potential for the utilization of BOF slag in the concrete industry.

3.2 Materials and methods

3.2.1 Materials and mix design

A representative mixture of BOF slag, collected from standard production, provided by Tata Steel (The Netherlands), was used in this study. Before the application, slag was ground using a planetary ball mill (Pulverisette 5, Fritsch) and sieved below 106 μm . Fig. 3.1 shows the particle size distribution of BOF slag after mechanical treatment as measured by laser diffraction spectroscopy (Mastersizer 2000, Malvern).

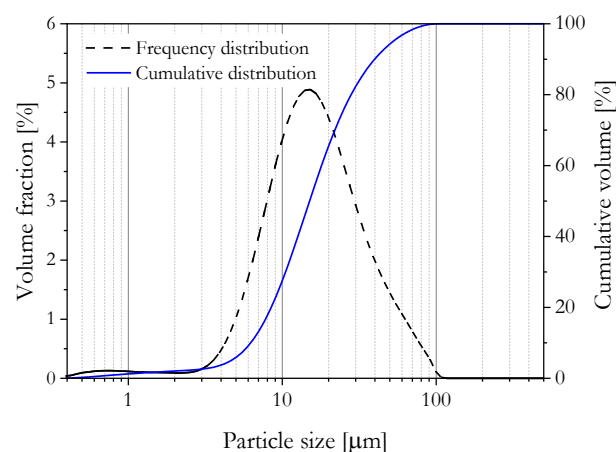


Figure 3.1: The particle size distribution of BOF slag.

The chemical and mineralogical compositions of BOF slag were determined with XRF analysis and the XRD Rietveld method and are presented in Table 3.1. The additive, tri-

potassium citrate monohydrate ($K_3C_6H_5O_7 \cdot H_2O$), was a commercially available technical grade product (GPR RECTAPUR®, purity > 99%).

Table 3.1: Mineralogical and chemical composition of BOF slag.

Mineral compound	Content [wt%]	Oxide	Content [wt%]
Brownmillerite	17.4	MgO	8.04
Magnetite	10.9	SiO ₂	13.8
C ₂ S	31.6	Al ₂ O ₃	2.44
Wuestite	21.1	CaO	39.5
Lime	0.5	P ₂ O ₅	1.67
Calcite	0.6	TiO ₂	1.45
Portlandite	1.2	V ₂ O ₅	1.05
C ₃ S	0.2	Cr ₂ O ₃	0.3
Amorphous	16.5	MnO	4.4
		Fe ₂ O ₃	29.0
		SrO	0.02
		Na ₂ O	< 0.2
		K ₂ O	< 0.01
		GOI 1000	1.41

BOF slag pastes containing tri-potassium citrate monohydrate were prepared with the water/binder ratio (w/b) of 0.16 to avoid bleeding and segregation (an exception was made for the reference sample with the w/b ratio of 0.24). In the reference sample, the w/b was chosen based on preliminary experiments in order to minimize the differences in the initial water content between the reference and activated samples, and at the same time, to enable sufficient workability for mixing and casting of the paste. Prior to the mixing, three different concentrations of potassium citrate, equivalent to 1, 2, and 3 wt% of slag, were added to the water to ensure a homogenous dispersion. The pastes were mixed for three minutes with a high-speed mixer. Subsequently, they were stored at 20 °C in plastic vials sealed with parafilm in a desiccator filled with water and sodium hydroxide pellets in order to minimize carbonation. The samples are named based on the amount of K₃-citrate added: C0, C1, C2, C3 for 0, 1, 2, 3 wt% (by mass of slag) of K₃-citrate dosage, respectively.

3.2.2 Methodology

The isothermal calorimetry and FTIR measurements were conducted according to the procedure described in Section 2.2.2.

Scanning electron microscopy (SEM) + Energy dispersive X-ray spectroscopy (EDX)

Scanning electron microscopy (SEM) measurements combined with energy-dispersive X-ray spectroscopy (EDX) analyses were performed on the pastes after 28 days of hydration. Before the measurements, pastes were cut with a saw to 2-3 mm slices, gently broken into smaller pieces, then immersed in isopropanol for 3 days and vacuum dried. The small pieces were subsequently embedded in epoxy resin, polished and coated with carbon for SEM analyses. The spectral imaging (SI) data were acquired with a JEOL JSM-7001F SEM equipped with two 30 mm² SDD detectors (Thermo Fisher Scientific) and a NORAN-System7 with NSS.3.3 software. A beam current in the focused probe of 6.2 nA and an accelerating voltage of 15 kV were used. The step size was 1 μ m, with an individual SI field comprising of 512 \times 384 pixels. For each sample, 16 fields were analyzed.

In order to observe the morphology of the hydration products, an FEI quanta 600 environmental scanning electron microscope was used to perform the SEM analyses on the 28 days hydrated pastes. Before analyses, the samples were sputtered with gold by using an Emitech K550X sputter coater (current 65 mA, coating time 20 s). Micrographs were recorded with the secondary electron detector at 5 kV at 65 000x magnification.

PhAse Recognition and Characterization (PARC)

The PhAse Recognition and Characterization (PARC) software was used to determine the chemical composition of the original slag phases and the hydration products as well as to quantify the phase composition of unhydrated, unmilled BOF slag. Detailed information about the PARC technique is provided elsewhere [101]. The data acquired with EDX mapping were processed with the PARC software by grouping each data point by its chemical composition into phases. Therefore, in contrast to the XRD Rietveld method, PARC software enables the quantification of different phases, including amorphous ones (note the resolution of 1 μ m). In order to acquire a representative chemical composition of the BOF slag phases and hydration products, an erosion filter was applied to exclude the data from the boundaries of phases. After erosion, only pixels surrounded by eight neighbouring pixels allocated to the same phase were used for analysis. The quantitative

phase analysis of BOF slag was performed on unmilled material (with the particle size between 1-2 mm) in order to minimize the error caused by the analysis of very fine particles. The densities of the converter slag phases used for the calculations of phase mass were derived from the Rietveld refinement.

X-ray diffraction (XRD)

For the quantitative XRD analysis, slag pastes were crushed in an agate mortar, and hydration was stopped with the double solvent exchange method (15 min in isopropanol, flushing with diethyl ether, 8 min drying at 40 °C in a half vacuum condition). The powders were milled with an XRD-Mill McCrone (RETSCH) and backloaded into sample holders. Corundum was used as an external standard [102]. The diffraction patterns were collected with a D4 ENDEAVOR X-ray Diffractometer equipped with a LynxEye detector and Co X-ray tube. Samples were measured on a rotating stage (with a rotation speed of 30 rpm) using a step size of 0.014° 2 θ and a time per step of 1 s for a 2 θ range of 12-80° 2 θ . The data analyses were performed with TOPAS Academic software v5.0. The ICSD codes for the crystal structures used during the Rietveld refinement are provided in Table 3.2.

Table 3.2: Structural data of the phases used for the Rietveld refinement.

Phase	ICSD
Brownmillerite	9197*
α' -C ₂ S	81097
Wuestite	67200*
C ₃ S	64759
β -C ₂ S	245074
Magnetite	20596
Lime	28905
Portlandite	202220
Hydroandradite	29247*
Katoite	9272
Pyroaurite	6295

*The structures were modified based on the PARC analyses.

In order to account for the high magnesium and manganese content in wuestite, as well as the low aluminum content and the presence of titanium in brownmillerite, the structural data sets for these phases were corrected based on the ion substitution levels derived from the PARC analyses. To calculate the absolute amounts of the phases, the G-factor method

was applied [102], [103]. The lattice and microstrain parameters were refined in the anhydrous slag and then used for the refinement of the pastes.

In-situ XRD test was performed with an X'Pert Pro PANalytical diffractometer equipped with a position-sensitive X'Celerator detector and Co X-ray tube, using an β -filter (iron foil). After 2 minutes of mixing with a high-speed mixer, the sample was inserted into the sample holder and covered with Kapton foil to minimize water evaporation and carbonation. The temperature of the sample was measured with a custom-made sample holder mounted on an Anton-Paar HTK2000 heating stage. Each diffractogram was recorded for 15 min in the range between 10 - $80^\circ 2\theta$ with a step size of $0.02 2\theta$ for up to 50 hours of hydration.

Thermogravimetry

The thermal behavior of the powdered samples (40-60 mg) was analyzed using a Jupiter STA 449 F1 Netzsch instrument. The samples were heated up to 1000°C at the rate of $5^\circ\text{C}/\text{min}$ under a nitrogen atmosphere. The amount of portlandite was quantified with a tangential method. The bound water content was determined based on the mass loss between 40°C and 500°C .

One batch leaching test

The leaching test was performed on unreacted BOF slag and 28-days cured slag pastes according to EN 12457-2 (one stage batch leaching test). Hydrated samples were crushed and sieved below 4 mm. The unreacted slag (2-4 mm) was used as is. The experiments were performed with liquid to solid ratios (L/S) of 10 using a dynamic shaker (ES SM-30, Edmund Buhler GmbH) at a constant speed of 250 rpm for 24h. Ultra-pure water ($0.055\ \mu\text{S}/\text{cm}$) was used as leachate. After 24 hours of shaking, leachates were filtered through a syringe filter (pore diameter $0.22\ \mu\text{m}$, Whatman) and acidified with concentrated HNO_3 . The solutions were analyzed with an inductively coupled plasma atomic emission spectrometer (ICP-OES, SPECTROBLUE), according to NEN 6966. The obtained element concentrations were compared with the limit values specified in the Dutch Soil Quality Decree [105].

Compressive strength

The compressive strength of the pastes was determined on cubic samples ($40 \times 40 \times 40\ \text{mm}^3$). Pastes were covered with foil and cured in the climate chamber (20°C , $\text{RH} > 95\%$)

until the testing age. The 7 and 28 days compressive strengths were determined according to EN 196-1, in three replicates for each composition.

Mercury Intrusion Porosimetry (MIP)

For Mercury Intrusion Porosimetry (MIP) measurements, after 28 days of hydration, the samples were cut into 3 mm cubic pieces, immersed in isopropanol for 7 days and subsequently dried in a desiccator for another 7 days. The AutoPore IV 9500 Micromeritics Series Mercury Porosimeter, with the maximum pressure of 228 MPa, was used for the measurements. The surface tension of mercury (γ_{Hg}) of 485 mN/m and a contact angle (θ) of 130° were adopted for the interpretation of the results [104].

3.3 Results and discussion

3.3.1 Characterization of unhydrated BOF slag

The surface exposure of potentially reactive phases of the milled, unreacted slag was evaluated with the PhASE Recognition and Characterization (PARC) analysis. The results are presented in Fig. 3.2. The phase map generated with the PARC software from SI spectra shows that even though the slag was milled and sieved (below $106 \mu\text{m}$), a part of belite and brownmillerite phases is trapped within bigger particles limiting their accessibility for the reaction.

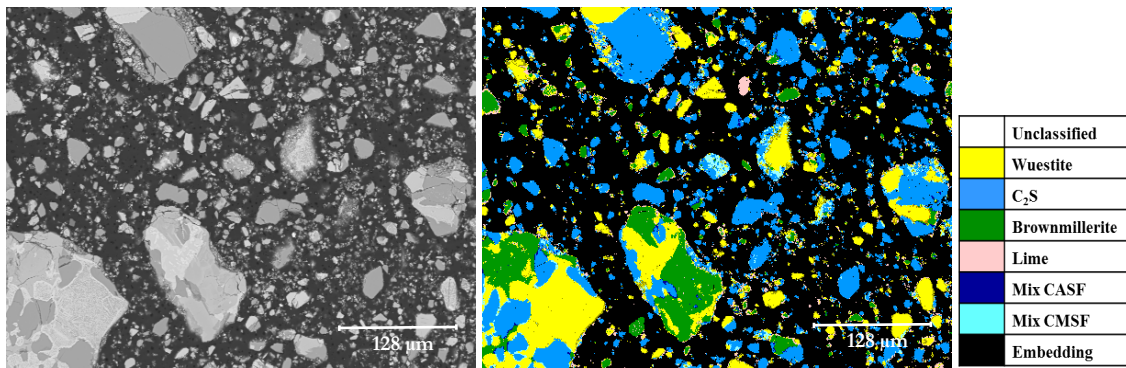


Figure 3.2: SEM image of BOF slag after milling (on the left) and corresponding color phase map (on the right) generated with PARC software based on the EDX data. Mix phases are the result of overlapping chemical information from two neighboring phases (where, C, A, M, S, F correspond to CaO, Al₂O₃, MgO, SiO₂ and Fe₂O₃/FeO, respectively).

In order to reveal the chemical composition of the amorphous slag phase, a comparison between the quantitative results of Rietveld and PARC analysis was made. In contrast to XRD Rietveld, the PARC method enables analysis of the amorphous phase and its

association with the crystalline counterpart (as the phase determination is based only on the chemical composition). A comparison of the amounts of the phases determined with PARC and XRD Rietveld (as shown in Table 3.3) indicated that part of the C₂S phase is X-ray amorphous.

Table 3.3: The comparison between the mineralogical composition of BOF slag acquired with Rietveld refinement and PARC analysis.

Mineral compound	PARC	<i>St dev</i>	Rietveld	<i>St dev</i>
Wuestite/magnetite*	30.6	4.4	32.0	1.1
C ₂ S	45.7	5.2	31.8	1.9
Srebrodolskite	14.8	2.4	17.4	0.9
Lime/portlandite/calcite*	1.1	0.6	2.3	0.2
Mix phases	5.8	0.8		
Amorphous			16.5	4.5

*Since with the PARC method, it is not possible to differentiate between lime, portlandite, and calcite as well as between wuestite and magnetite, these phases are grouped together.

By grouping the EDX data points with similar chemical composition into the phases, sum spectra can be created that give the average chemical composition of each phase (Table 3.4). In this way, the presence of minor elements in the phases can also be identified, which is particularly useful for revealing which phases contain heavy metals. The data provided in Table 3.4 indicate that chromium is mainly located in belite, and vanadium in belite and brownmillerite. It must be noted, however, that the contents of heavy metals derived from the PARC method are overestimated in comparison to XRF analysis and the presence of chromium in belite should be considered with caution (see also Chapter 6).

Table 3.4: Chemical composition of the main BOF slag phases.

Phase	Oxide													
	Na ₂ O	MgO	Al ₂ O ₃	SiO ₂	P ₂ O ₅	SO ₃	K ₂ O	CaO	TiO ₂	V ₂ O ₅	Cr ₂ O ₃	MnO	Fe ₂ O ₃	
Wuestite/magnetite	0.00	23.66	0.20	0.75	0.02	0.00	0.04	2.54	0.03	0.12	0.47	11.71	60.43	
Brownmillerite	0.04	0.65	11.22	1.81	0.07	0.01	0.08	42.31	5.14	1.51	0.38	1.26	35.01	
C ₂ S	0.15	0.28	0.54	28.19	3.38	0.15	0.11	61.41	1.19	1.11	1.22*	0.09	2.17	

* The Cr₂O₃ analysis should be treated with caution since the Cr emission spectrum overlaps with the sum peak of Ca+Si K α .

3.3.2 Isothermal calorimetry

The isothermal conduction calorimetry results from the reference paste (w/b of 0.24) and pastes containing tri-potassium citrate (w/b of 0.16) are shown in Fig. 3.3. In the absence of potassium citrate, no distinctive peak is observed, which could be assigned to the reaction

of slag phases. The heat is evolved mainly within the first 1-2 hours and most likely corresponds to the dissolution and to a small extent, the reaction of the dissolving phases (as the heat evolved in this period is higher than that observed in the presence of activator, where the main reaction occurs later). The addition of citrate leads to a distinct heat flow peak, which appears at ~ 13 h with 1 wt% potassium citrate added. Further increase of potassium citrate dosage results in the shortening of the induction period and the peak of the heat release rate occurs at approximately 8.5 h and 7.5 h, in the case of 2 wt% and 3 wt% of potassium citrate, respectively. With the increasing amount of potassium citrate, the total heat released after 200 hours of hydration increases significantly from $56 \text{ J/g}_{\text{binder}}$ in the case of the reference sample to $120 \text{ J/g}_{\text{binder}}$ when 3 wt% of potassium citrate is added.

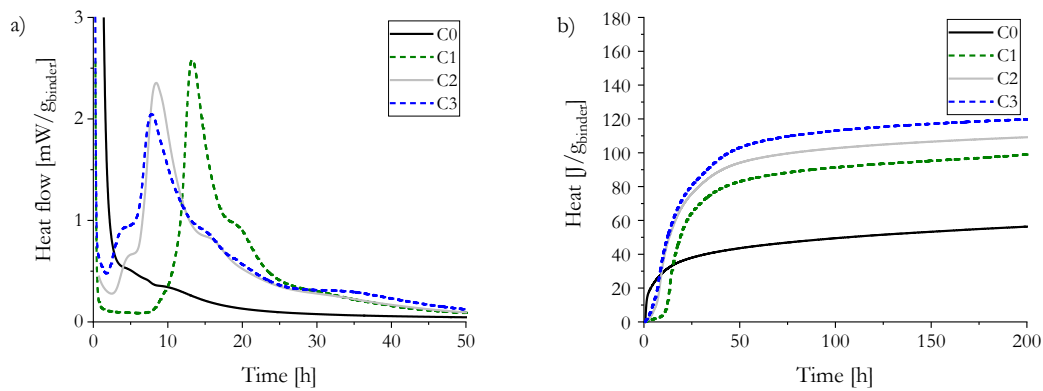


Figure 3.3: Heat flow and cumulative heat evolution of slag pastes with dosages of tri-potassium citrate varying from 0 to 3 wt%.

Even though tri-potassium citrate is usually used as a retarder of the cement/supplementary cementitious materials hydration, its role can differ depending on the applied dosage and w/b ratio. Pacanovsky et al. [106] described that in the systems based on Portland cement and silica fume, tri-potassium citrate salts demonstrate a reverse role beyond a certain dosage, switching from retarders to accelerators. Moreover, the required dosage of potassium citrate to become an accelerator decreases with a decreasing w/b ratio. In the slag system, an analogous tendency is observed. In contrast to the reference, the hydration of potassium citrate-activated samples is preceded by an induction period. At the same time, with increasing the tri-potassium citrate dosage between 1 and 3 wt%, hydration of BOF slag is accelerated, which is likely to occur with relatively high amounts of tri-potassium citrate used in this study and low w/b ratio.

3.3.3 Identification of reactive phases

In order to evaluate which reactive phases contribute to the heat release observed with the isothermal calorimetry, the early age hydration was monitored with in-situ XRD. Fig. 3.4 shows the XRD patterns recorded within the first 50 hours of hydration of the paste with 3 wt% of tri-potassium citrate. An apparent decrease in the peak intensity at $39^\circ 2\theta$ can be observed, showing that brownmillerite is the most reactive phase at the early hydration age.

The hydration of brownmillerite and other BOF slag phases was further investigated with ex-situ experiments and subsequent quantification using the XRD Rietveld method. The reference sample and the tri-potassium citrate activated samples were analyzed after 7 and 28 days of hydration and compared with the unreacted BOF slag (Table 3.5). From the XRD Rietveld analyses, it appears that hydration of brownmillerite occurs mainly up to 7 days, and its extent is highly influenced by the activator dosage. In the sample with the highest activator dosage (3 wt%), almost 70 wt% of brownmillerite undergoes reaction. Rapid hydration of brownmillerite observed with in-situ and ex-situ XRD methods corresponds well with the heat evolution detected with the isothermal calorimetry.

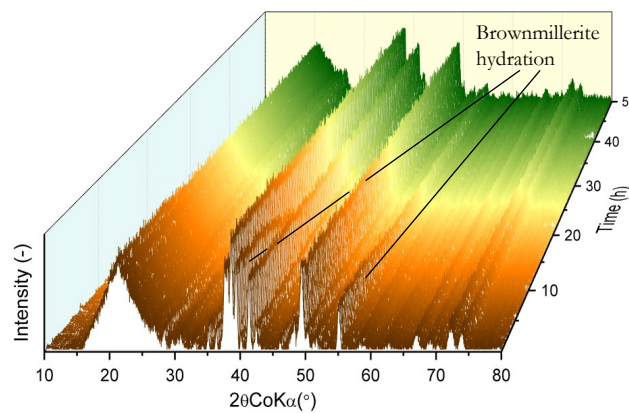


Figure 3.4: In-situ XRD patterns of the hydrating slag with 3 wt% of activator dosage, within 50 hours of hydration. The peak in the range between $15\text{-}30^\circ 2\theta$ is due to the Kapton foil and free water.

The extent of belite hydration is also affected by the presence of the activator. After 7 days of hydration, a decrease of belite content with the increasing amount of activator is observed. This effect is likely due to the higher alkalinity of the pore solution in the presence of tri-potassium citrate. The accelerated reaction of C_2S at the early hydration ages was previously reported with conventional alkaline activation [88]. After 28 days of hydration, however, the belite content is similar in all samples, with a tendency towards a higher degree of reaction in the series with 1 wt% of potassium citrate.

Table 3.5: The phase composition of the hydrated BOF slag pastes in comparison to unhydrated slag in wt%, determined by XRD-Rietveld analysis.

Phase	BOF	7 days				28 days				*St. dev.
		C0	C1	C2	C3	C0	C1	C2	C3	
Wuestite	21.1	19.5	19.4	17.9	15.3	18.4	15.9	16.5	15.9	1.1
Magnetite	10.9	11.2	11.3	11.0	11.5	11.3	10.8	10.9	11.1	0.8
C ₂ S (α' + β)	31.8	30.2	28.8	28.7	27.3	26.0	22.2	25.3	27.4	1.9
Brownmillerite	17.4	17.2	11.1	8.1	6.3	14.3	10.8	7.8	6.6	0.9
Hydrogarnet	0.0	5.3	10.8	13.3	15.1	8.7	14.0	15.0	16.2	
Portlandite	1.2	1.2 (1.7) ^a	0.5 (0.8)	0.5 (0.4)	0.3 (0.5)	1.5 (2.0)	0.7 (1.3)	0.5 (1.1)	0.4 (0.9)	0.2
Lime	0.5	0.5	0.4	0.4	0.4	0.3	0.4	0.3	0.3	0.1
Calcite	0.6	0.2	0.2	0.2	0.1	0.5	0.3	0.3	0.2	0.1
Amorphous**	16.5	18.7	23.6	29.2	35.0	26.0	33.6	33.7	34.2	4.5

^a the number in () indicates the amount of portlandite determined with thermogravimetric analysis (tangential method)

* Standard deviations are derived from 3 independent measurements of unhydrated BOF slag

**Pyroaurite is included in the amorphous phase due to its low content in hydration products and low crystallinity

Next to the brownmillerite and belite, during the investigated period, the dissolution of wuestite also takes place. Analogously to the belite phase, wuestite exhibits increased early age reactivity in the presence of an activator. Previous studies implied that the reactivity of wuestite is related to its chemical composition, especially the magnesium content [107]. In general, the higher the magnesium content, the greater the extent of wuestite dissolution is reported [108]. Moreover, it was revealed by De Windt et al. [86], by investigating the leaching properties, that the degree of wuestite dissolution depends on particle size distribution, degree of surface alteration and water to solid ratio applied (associated with the pH variation). With lower water to solid ratios, higher leaching of elements was reported. It is, therefore, likely that the observed reactivity of wuestite phase is mainly a result of surface alterations caused by the applied milling procedure, low w/b ratios as well as favorable chemical composition. It must be noted that the reactivity of wuestite observed with the XRD analysis might be slightly overestimated due to the sample preparation procedure, where the milling time must be balanced to ensure sufficient grinding of hard phases (e.g. wuestite) and to prevent the hydration products from amorphization. In contrast, the magnetite content is relatively stable in all pastes at the investigated hydration ages.

3.3.4 Hydrates assemblage

The XRD analyses revealed the presence of three crystalline hydration products: siliceous hydrogarnet, pyroaurite, and portlandite (Fig. 3.5). Formation of siliceous hydrogarnets, with the general chemical formula $\text{Ca}_3(\text{Al}_x\text{Fe}_{1-x})_2(\text{SiO}_4)_y(\text{OH})_{4(3-y)}$, was previously observed for Portland cement systems [91], [109], [110], [111]. Among iron-rich hydration products reported in the literature (including hydrogarnets, ferrihydrites, Fe-containing AFm and Fe-ettringite), hydrogarnets are the most stable iron-containing phases [92].

Since in the structure of hydrogarnet, Fe^{3+} can be substituted by Al^{3+} in octahedral positions and SiO_4^{4-} by 4OH^- in tetrahedral positions, the determination of the chemical composition of hydrogarnets becomes difficult, especially at the early hydration ages when metastable phases such as silica-free hydrogarnets (katoite) can form [92], [112].

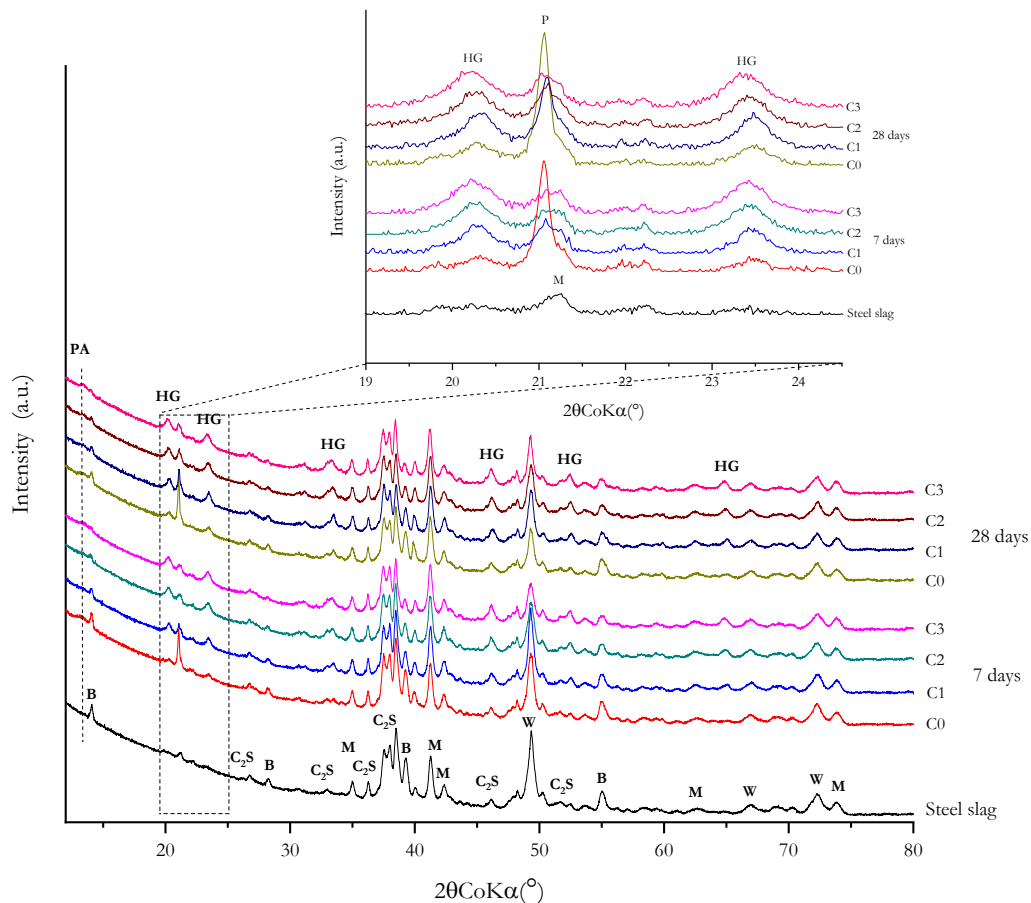


Figure 3.5: XRD patterns of BOF slag and hydrated pastes (Legend: B - Brownmillerite, C_2S - Belite, M - Magnetite, W - Wuestite, P - Portlandite, HG - Hydrogarnet, PA - Pyroaurite).

Dilnesa et al. [92] suggested the occurrence of solid solutions between hydrogarnets with low and high silica content as well as between iron and aluminum-containing end members. The occurrence of hydrogarnets with varying chemical compositions results in the broadening of XRD reflections (see Fig. 3.5). In order to provide the best possible quantification of this phase, in the Rietveld analysis, two structures, including low-silica hydrogarnet (katoite, ICSD: 9272) and high-silica hydrogarnet (hydroandradite, ICSD: 29247), were adopted. Additionally, the structure of hydroandradite was adjusted for the iron substitution with aluminum, based on the PARC analysis, assuming that hydroandradite contains most of the available iron and aluminum. The following formula $\text{Ca}_3(\text{Fe}_{0.85}, \text{Al}_{0.15})_2\text{Si}_{1.15}\text{O}_{4.6}(\text{OH})_{7.4}$ was used for the refinement. Even though at ambient conditions siliceous hydrogarnets tend to be poorly crystalline or possess a very small crystal size (as reported by [92]), resulting in extremely broad reflections, the Rietveld analysis (Table 3.5) clearly revealed that in the converter slag system, hydrogarnet is the main crystalline hydration product. The amount of the hydrogarnet formed correlates well with the extent of the brownmillerite hydration, increasing with the increased dosage of tri-potassium citrate. The SEM image presented in Fig. 3.6 provides an indication of the morphology of hydrogarnet crystals in the BOF slag paste [113], [114].

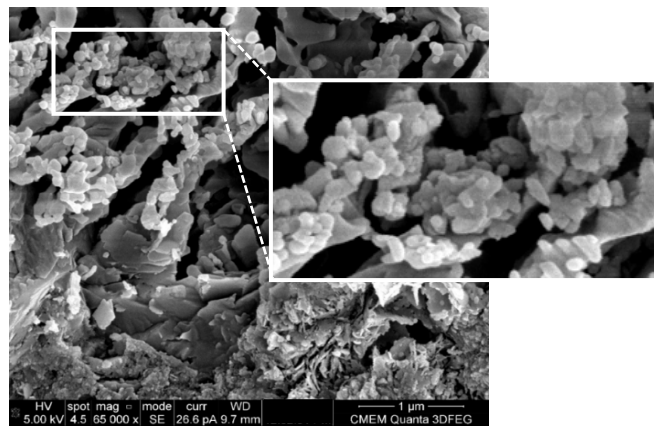


Figure 3.6: BOF slag paste hydrated with 3 wt% of tri-potassium citrate for 28 days. Applied zoom indicates the location of hydrogarnet crystals.

The formation of pyroaurite and portlandite is also observed in the XRD patterns. Pyroaurite, as a Fe-rich member of the hydrotalcite group (pyroaurite $\text{Mg}_6\text{Fe}^{3+}_2(\text{OH})_{16}[\text{CO}_3]\cdot 4\text{H}_2\text{O}$) gives a broad reflection at around $2\theta = 13.5^\circ$ whereas the strongest reflection of portlandite is located at $2\theta = 21.1^\circ$. The content of portlandite in the hydrated samples is reduced with the addition of a tri-potassium citrate activator.

The presence of hydrogarnet and other hydration products in BOF slag pastes was further confirmed with the TG-DTG analyses, as shown in Fig. 3.7. Mass loss observed in the temperature range between 200 °C and 400 °C can be assigned to the water loss from siliceous hydrogarnet [92]. In agreement with the XRD Rietveld results, the formation of siliceous hydrogarnet occurs mostly within 7 days of hydration, and its extent is greater for higher dosages of tri-potassium citrate. In this temperature range, the decomposition of pyroaurite also takes place [115]. Rozov et al. [116] reported that pyroaurite decomposes at slightly lower temperatures than Al-rich hydrotalcite; however, it follows the same sequence of steps, comprising the loss of interlayer water, the decomposition of hydroxyl groups and decomposition of carbonate anions. With the DTG method, the presence of amorphous C-S-H gel could also be identified with the main mass loss due to the water release below 200 °C. The amount of C-S-H gel formed after 7 days of hydration differs substantially between the samples, being higher for the samples with a higher activator dosage, whereas after 28 days, it is similar for all samples. This observation agrees with the rate and extent of belite hydration, as measured with the XRD Rietveld method. It can be therefore concluded that in BOF slag systems, brownmillerite hydrates (in the presence of C_2S) to form mainly siliceous hydrogarnet, whereas hydration of C_2S leads mainly to the formation of C-S-H gel.

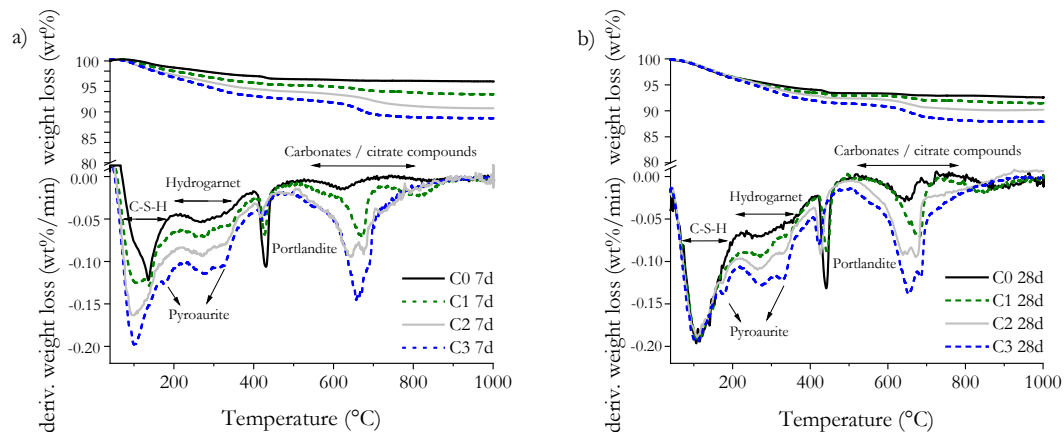


Figure 3.7: Thermal analysis (TG and DTG) of slag pastes with dosages of tri-potassium citrate varying from 0 to 3 wt% after 7 and 28 days of hydration.

It is not clear whether in the presented systems C-S-H gel can uptake Fe^{3+} . The formation of the C-S-H next to hydroandradite was found to be unavoidable even during the synthesis of siliceous hydrogarnet [91]. Whereas Labhassetwar [117] suggested the possibility of Fe^{3+} inclusion in the C-S-H gel, from the thermodynamic calculations, it appears that in the hydrated Portland cement, iron is mostly present in the siliceous hydrogarnet [92]. As in this

study alkalizing additive was used, the behavior of Fe^{3+} species similar as in alkali-activated systems should also be considered. Daux et al. [118] showed that in alkali-activated systems after the dissolution of iron-rich precursor, precipitation of Fe is much faster than precipitation of Si and Al. Fe^{3+} is found to act similarly as Ca^{2+} , removing OH^- groups due to the precipitation of hydroxides and oxyhydroxides [119]. At the same time, an indication of Al^{3+} substitution with Fe^{3+} in the aluminosilicate structure was also reported [120]. For aluminum deficient systems like LD-slag, however, no data is available.

Besides C-S-H gel and hydroandradite/pyroaurite, the mass losses due to portlandite decomposition at around 430 °C and decomposition of carbonates/citrate compounds between 600-800 °C are observed. The amount of portlandite decreases when higher activator dosages are applied, which correlates well with the XRD results. The mass loss in the temperature range between 600-800 °C is intensified with the increasing content of tri-potassium citrate. In this range, decomposition of carbonates usually takes place. It should be emphasized, however, that special care was taken during the sample curing and hydration stoppage to avoid carbonation. The samples were prepared and measured twice, leading to the same results. It is therefore proposed that citrate compounds were formed and contributed to the mass change in this temperature range. As no crystalline citrate precipitates could be identified with the XRD method, it is difficult to conclude in which form citrates are present in the system.

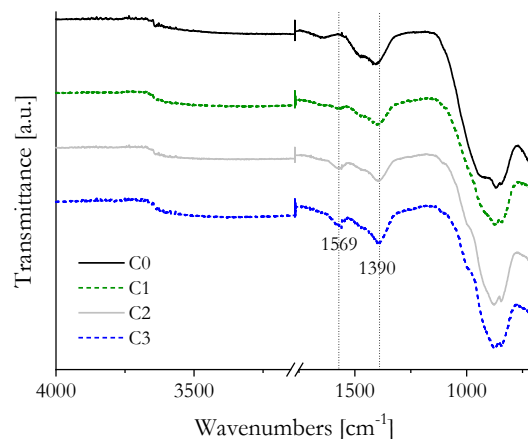


Figure 3.8: FTIR spectra of converter slag pastes after 28 days of hydration.

From the FTIR measurements (Fig. 3.8) performed on the 28 days hydrated converter slag pastes, it is clear, however, that citrate groups remain in the samples after the hydration stoppage. Therefore, their presence in the pore solution is minimal or can be excluded since, with the solvent exchange method, citrate ions would be removed with the pore solution. The infrared peaks located at 1569 and 1390 cm^{-1} are associated with the $\nu_{\text{C=O}}$ and ν_{asCOO} bands, respectively [99].

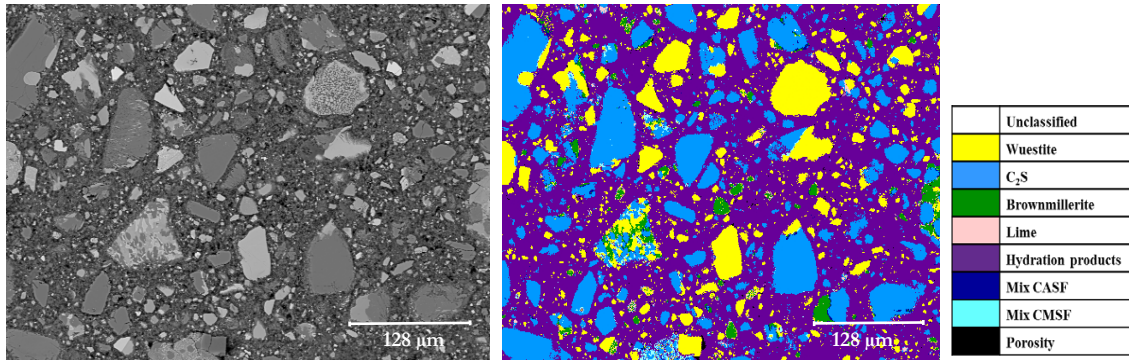


Figure 3.9: Representative BSE image of hydrated slag paste with tri-potassium citrate dosage of 1 wt%.

In order to determine the chemical composition of the hydration products, the PARC software was used. Fig. 3.9 shows an example of phase identification in the sample activated with 1 wt% of tri-potassium citrate after 28 days of curing.

In the PARC analysis, the individual phases of the hydration products could not be established due to the small crystal size of hydroandradite that is very well intermixed with C-S-H gel. Nevertheless, the averaged ratios of certain elements within the hydration products can be used to describe the differences between the chemical compositions of the products in the samples hydrated with varying dosages of tri-potassium citrate. Figure 3.10 shows the molar ratios of Al/Si and V/Si vs. Ca/Si ratio. The results correspond well with the findings described with the Rietveld analysis. With the increasing tri-potassium citrate dosage, Al/Si ratio and Ca/Si ratio (Fig. 3.10a) proportionally increase, confirming the enhanced reactivity of the brownmillerite in the presence of activator (as brownmillerite is the only source of aluminum). Since brownmillerite is highly contaminated with vanadium (see Table 3.4), vanadium content in the hydration products was also investigated. As shown in Fig. 3.10b for vanadium, a similar trend was observed as for aluminum, showing that vanadium was not removed from the sample during the hydration stoppage procedure, which indicates that it is most likely immobilized within the hydration products.

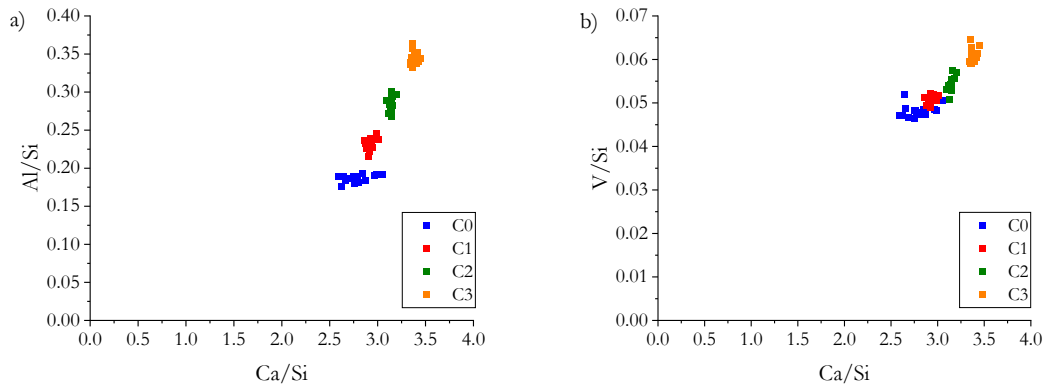


Figure 3.10: Molar ratios a) Al/Si vs. Ca/Si and b) V/Si vs. Ca/Si of the hydration products in the samples with varying dosages of tri-potassium citrate (0 to 3 wt%), hydrated for 28 days (each dot represents averaged EDX data from the SI field of 512×384 pixels).

3.3.5 Microstructure and mechanical properties

Given that the addition of tri-potassium citrate considerably reduces the water demand of the slag pastes, low porosity and high mechanical performance were expected for the activated samples. The MIP results of the slag pastes after 28 days of hydration are shown in Fig. 3.11. The higher water requirement of the reference sample in order to obtain a similar consistency of all investigated pastes resulted in a clearly higher porosity, as presented in Fig. 11, and, in consequence, low mechanical performance ~ 19 MPa at 28 days (Fig. 3.12). For the potassium citrate activated samples, the capillary porosity is strongly reduced, and the cumulative porosity decreases with the increased amount of activator, which is in agreement with the higher amounts of hydration products observed with the thermogravimetric method and XRD Rietveld analysis.

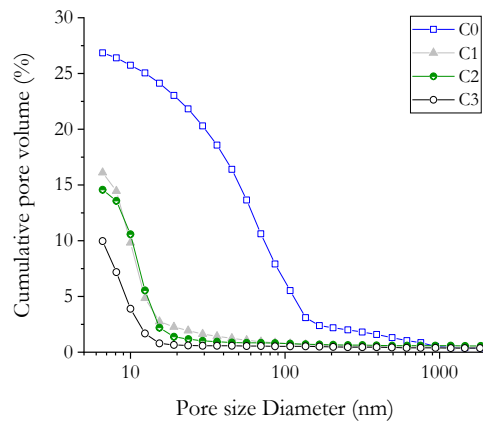


Figure 3.11: The cumulative pore volume of converter slag pastes after 28 days of hydration.

The changes in the porosity, however, do not reflect the changes in mechanical performance. Whereas at 7 days of hydration, the mechanical performance is improved with the increased activator dosage, at 28 days, the optimum dosage of potassium citrate is equal to 1 wt%, resulting in compressive strength of 75 MPa. Further increase of activator amount results in the decrease of compressive strength to 63 MPa and 60 MPa for activator dosage of 2 wt% and 3 wt%, respectively.

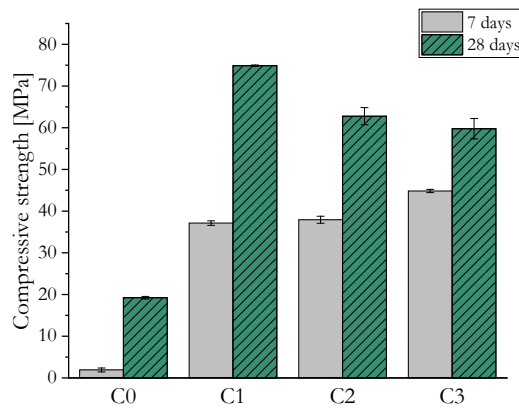


Figure 3.12: Compressive strength of the converter slag pastes with dosages of tri-potassium citrate varying from 0 to 3 wt% after 7 and 28 days of hydration.

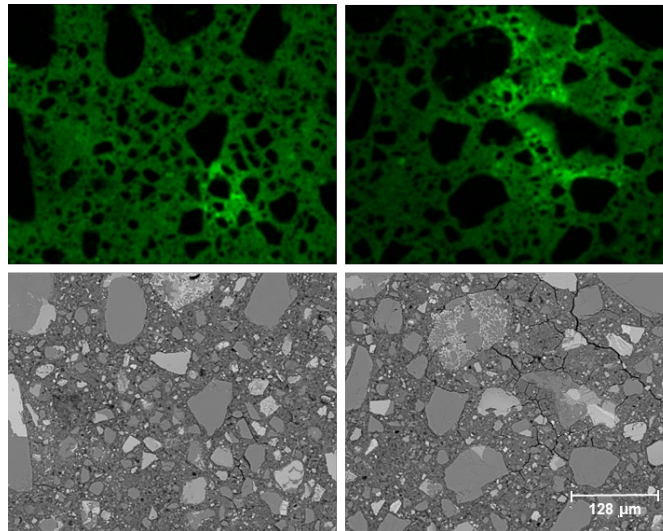


Figure 3.13: Potassium distribution (derived from EDX mapping analysis) in the hydrated slag paste (C3) and the corresponding grey-scale image of the investigated area.

From Fig. 3.13, showing the potassium distribution in the hydrated paste, it is clear that cracks have been formed in the areas highly enriched in potassium. It is therefore postulated that the decrease of the compressive strength observed for the pastes with the increasing

activator dosage is a result of the incompatibility of the C-S-H gel and the potassium-enriched gel. The presence of cracks in alkali-activated materials can be caused by the reorganization of the alkali products to form a denser gel, autogenous shrinkage, or the differences in the kinetics of the formation of the gels [38], [121]. Furthermore, the slightly greater extent of belite hydration in the sample with 1 wt% of potassium citrate, as revealed with the Rietveld XRD method, is an additional factor contributing to the improved strength of this sample.

3.3.6 Environmental impact

The BOF slag used in this study contains chromium (Cr) and vanadium (V) (see Table 3.1). As shown in Table 3.4, Cr and V are mostly incorporated in the reactive slag phases (belite and brownmillerite), implying a potential risk of leaching of those elements during the service life of BOF slag-based materials.

Table 3.6: Leaching of inorganic contaminants measured by one stage batch leaching test and the SQD limit values.

Element	Unshaped material (SQD)	BOF slag	C0	C1	C2	C3
	mg/kg	mg/kg	mg/kg	mg/kg	mg/kg	mg/kg
Antimony (Sb)	0.32	bdl	0.16	0.15	0.17	0.15
Arsenic (As)	0.90	0.02	0.10	0.12	0.10	0.10
Cadmium (Cd)	0.04	bdl	bdl	bdl	bdl	bdl
Chromium (Cr)	0.63	0.28	0.03	0.05	0.01	0.03
Cobalt (Co)	0.54	bdl	bdl	bdl	bdl	bdl
Coper (Cu)	0.90	bdl	bdl	bdl	bdl	bdl
Lead (Pb)	2.30	bdl	bdl	bdl	bdl	bdl
Molybdenum (Mo)	1.00	0.02	bdl	bdl	bdl	bdl
Nickel (Ni)	0.44	bdl	bdl	bdl	bdl	bdl
Tin (Sn)	0.40	bdl	bdl	bdl	bdl	bdl
Vanadium (V)	1.80	3.78	0.10	0.13	0.09	0.18
Zinc (Zn)	4.50	bdl	0.12	0.11	0.13	0.13

*bdl- below detection limit.

The Dutch Soil Quality Decree (SQD) [105] specifies the limit values for leaching of environmentally sensitive elements from the materials in civil applications. In this study, the one batch leaching test was performed in order to evaluate the environmental impact of the

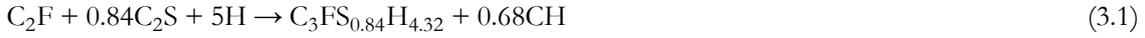
raw material as well as the paste samples after 28 days of hydration. The results are shown in Table 3.6. For non-treated BOF slag, high leaching of vanadium is observed, exceeding twice the limit value specified in the SQD legislation, which is commonly reported for BOF slag [76]. Similarly, the leaching of chromium, second most abundant heavy metal in slag, is detected, however, falls below the limit level. The leaching of heavy metals from all the 28-days BOF slag pastes is very limited.

The minor leaching values of Cr and V from the converter slag pastes together with the high contents of vanadium in the reaction products, as shown in Fig. 3.10b, clearly show that heavy metals are very well retained within the hydrated slag matrix. From the literature, it appears that the C-S-H gel can immobilize Cr, whereas immobilization of V in the C-S-H phase remains questionable [122], [123], [124]. Hydroandradite $A_3B_2(SiO_4)_{3-x}(OH)_{4x}$ (as a member of the hydrogarnet family) also possesses a high capacity to immobilize heavy metals. The Cr^{3+} and V^{3+} can occupy the B site in hydroandradite, substituting trivalent cations (Fe^{3+} and Al^{3+}). At higher oxidation states, chromium and vanadium can potentially substitute the hydroxyls ($H_4O_4^+$) in the form of oxyanions (CrO_4^{2-} , VO_4^{3-}). The immobilization of heavy metals in hydrogarnets has also been observed in previous studies [113], [125], [126]. Nonetheless, when samples are exposed to CO_2 , the drop of pH can lead to an increased release of vanadium [76]. Therefore, further investigation is required in order to evaluate the influence of the materials aging and the neutralization effects on the retention of contaminants in the BOF slag hydration products.

3.4 BOF slag hydration: theoretical water demand and chemical shrinkage

BOF slag contains C_2S and C_2F (see Table 3.7), which render its cementitious properties. In contrast to Ordinary Portland Cement, in BOF slag, C_2S is the most abundant phase, and only negligible quantities of C_3S are usually observed. This appears as one of the main reasons for the late reactivity of slag. Furthermore, slag contains around 30 wt% of relatively inert phases, including magnetite and wuestite. The presence of these phases not only affects the total reactivity of slag but also increases its mass (with the density of about 3.85 g/cm^3 for slag vs. 3.15 g/cm^3 for cement). The phase composition and slag fineness determine the water demand. The theoretical water demand needed for the full hydration of slag (assuming

that C_2S and C_2F are the only reactive phases) is calculated according to the following reactions [127]:



whereby the composition of hydrogarnet was modified according to [92]. Assuming that the amorphous phase in slag accounts mostly for the XRD-amorphous C_2S (as was earlier revealed in this thesis with a comparison between XRD Rietveld analysis and PARC analysis, see Section 3.3.1), the calculated water demand, expressed as water/slag mass ratio, is 0.20.

Table 3.7: Mineralogical composition of BOF slag and phase properties.

Phase	Mass content in BOF slag [wt%]	Density (TOPAS) [g/cm ³]	Molar mass of pure phases [g/mole]	Molar volume [cm ³ /mole]
Wuestite	21.1	4.600	71.85	15.62
Magnetite	10.9	5.122	55.85	10.90
C_2S (α' + β)	31.8	3.296	172.24	52.26
C_2F	17.4	3.810	271.85	71.35
Portlandite	1.2	2.261	74.09	32.77
Lime	0.5	3.431	56.08	16.34
Calcite	0.6	2.763	100.09	36.23
Amorphous	16.5			
Hydrogarnet		3.100	456.22	147.17
C-S-H		2.25*	213.09	94.58

*The value is taken from [127].

Assuming that C_2S and C_2F are the only reactive phases in BOF slag, the total chemical shrinkage can be calculated based on proposed reactions and data presented in Table 3.7. After complete hydration of BOF slag, the total chemical shrinkage is 4.77 ml/100 g_{slag}, which translates to 10% volume reduction. This value is substantially lower than that reported for OPC (6-9 ml/100 g_{cement}) [128], [129] or GGBFS slag (11-15 ml/100 g_{slag}) [129]. It has to be noted, however, that BOF slag contains inert phases. When the chemical shrinkage is normalized to the content of reactive phases (C_2S and C_2F) in BOF slag, the shrinkage value is increased to 7.26 ml/100g_{reactive phases}, similar to that observed for OPC. In Fig. 3.14, the measured phase composition of BOF slag hydrated for 28 days (Section 3.3.3,

Table 3.5, sample C0) is presented. Due to the fact that amorphous content from original slag and amorphous content due to precipitation of C-S-H gel could not be distinguished in our study, the amount of C-S-H gel was determined based on the bound water content (from thermogravimetric analysis) in 28 days-hydrated sample. Firstly, the amount of water bound in hydrogarnet and portlandite was calculated, and then, all the remaining water was assumed to be incorporated in C-S-H gel. The calculated amount of C-S-H gel was subsequently subtracted from the total amorphous content in 28 days-hydrated paste to estimate the content of unreacted XRD-amorphous C_2S .

To verify the proposed reactions, in Fig 3.15, the calculated phase composition of hydrated BOF slag is presented. The hydration degree of $\alpha = 0.3$ is used (based on the reaction degree of the C_2S phase after 28 days, as shown in Fig. 3.14).

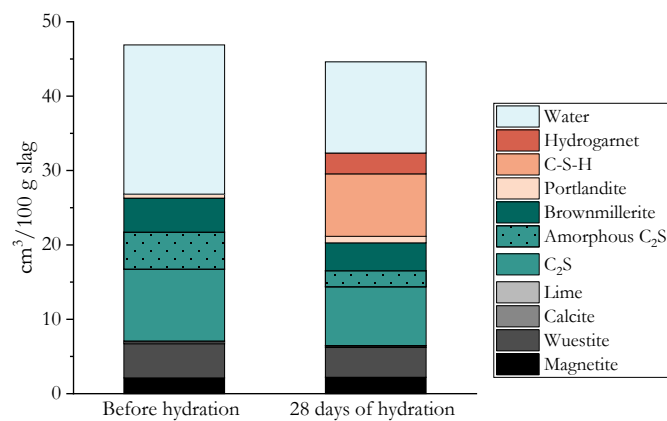


Figure 3.14: Composition of BOF slag paste before and after 28 days of hydration (measured).

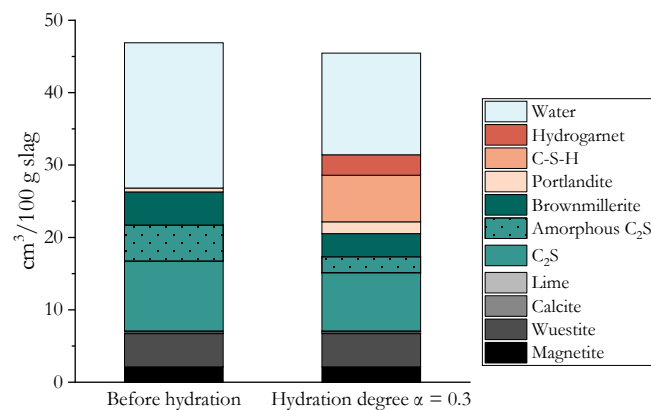


Figure 3.15: Composition of BOF slag paste before hydration and at the hydration degree of $\alpha = 0.3$ (modeled).

The comparison of Figures 3.14 and 3.15 reveals some discrepancies between the volume ratios of the hydration products calculated according to the proposed reactions and their actual quantities in slag pastes after 28 days of hydration. One of the main reasons is the difference in hydration kinetics of C_2S and C_2F phases. Moreover, the following factors must be considered when modeling the hydration of BOF slag:

- Hydrogarnets form a range of solid solutions. Their composition may vary with hydration progress. Hydrogarnets possess poorly crystalline structures at ambient conditions, and therefore the quantitative interpretation with XRD method may be erroneous.
- Amorphous iron (III) hydroxides are likely to form at the early stages of BOF slag hydration.
- Partial dissolution of wuestite occurs during the hydration of BOF slag.
- Hydrotalcite is one of the hydration products when BOF slag is partially carbonated.
- Quantitative analysis of the amorphous phase is required (likely it is not pure C_2S).
- The impurities in the slag phases affect their reactivity.
- The amount of the bound water after hydration stoppage with isopropanol tends to be overestimated, where only about 75% of water is exchanged [130].

3.5 Conclusions

This chapter presents a novel concept to upgrade BOF slag to a high-performance cementitious binder in the concrete industry. With the aim to activate iron-containing phases, a tri-potassium citrate monohydrate additive was applied to produce slag pastes, and the optimum dosage was evaluated. One additive-free sample was also prepared for comparison. The experimental investigation leads to the following conclusions:

- K_3 -citrate promotes the dissolution and hydration of brownmillerite phase. The majority of brownmillerite is hydrated within 24 hours, and the reaction rate is controlled by the activator dosage. The degree of brownmillerite hydration after 28 days increases with the increasing activator dosage.
- In the presence of an activator, hydration of belite and wuestite is accelerated at the early ages. The extent of belite hydration after 28 days shows the maximum in this study with the addition of 1 wt% of potassium citrate.

- The main reaction products of BOF slag hydration are hydroandradite, pyroaurite, and C-S-H gel. Most likely, their high capacity to immobilize heavy metals prevents the leaching of chromium and vanadium from 28 days hydrated pastes.
- The addition of K₃-citrate significantly reduces the water demand of slag pastes. The superplasticizing function of the tri-potassium citrate additive is crucial, enabling the production of converter slag pastes with low porosity (between 10-16%, depending on the activator dosage) and high compressive strength up to 75 MPa after 28 days of hydration.

The optimization of BOF slag hydration kinetics

In this chapter, the early age hydration kinetics of BOF slag is investigated. Isothermal calorimetry and in-situ X-ray diffraction (XRD) are used to examine the effects of K_3 -citrate concentration and nanosilica addition on slag reactivity. The results reveal that brownmillerite is the most reactive slag phase during the first 24 hours of hydration. The kinetics of brownmillerite hydration is controlled by K_3 -citrate dosage, and the reaction is strongly accelerated with highly concentrated solutions (0.6 M). A similar phenomenon is reported for amorphous C_2S at the early hydration stages, but the adverse effect is observed in the long term. Among hydration products, crystalline siliceous hydrogarnet is identified. Precipitation of hydrogarnet (as observed with the XRD analysis) coincides with the occurrence of a shoulder in the heat flow curves after the heat flow maximum due to brownmillerite dissolution. It is shown that nanosilica slightly delays the hydration of brownmillerite while enhancing the precipitation of C-S-H gel. In consequence, the early age mechanical properties of BOF slag mortars with nanosilica addition are improved.

4.1 Introduction

In cement systems, the reaction of brownmillerite takes place simultaneously with the reaction of C_3A at the very early hydration stages, while the reaction of C_2S contributes to the late strength development. Due to the late hydraulic activity of C_2S , early age mechanical properties of BOF slag-based materials might be insufficient for practical applications. In the previous chapter, it was shown that the chemical activation of BOF slag with potassium citrate enables the increase of the overall hydration degree of the hydraulic phases in BOF slag, which, together with the superplasticizing effect of potassium citrate, lead to the superior mechanical properties of BOF slag pastes, up to 75 MPa, after 28 days of hydration.

Reproduced from:

Kaja, A. M., Melzer, S., Brouwers, H. J. H., & Yu, Q. L. On the optimization of BOF slag hydration kinetics. Submitted.

However, the impact of the early age phase development on mechanical properties has not yet been investigated.

A commonly applied strategy to increase the early-age strength development of hydrating cement and its composites with slag or pozzolanic materials is the addition of nanomaterials, particularly nanosilica [131], [132]. Due to the amorphous nature and high specific surface area, nano-silica (nS) features a very high pozzolanic activity [133], [134], [135]. The accelerating function of nS is attributed to the provision of additional nucleation sites and, as revealed more recently [136], to the rapid depletion of calcium ions from the pore solution. Nano-silica contributes not only to early strength development but also causes structural densification [137], [138], [139], [140]. The structural refinement in the presence of nano-silica and the consequent durability improvement can be crucial for BOF slag-based systems, which typically contain heavy metals (mainly vanadium and chromium) [141], [76], [86]. In the BOF slag system, nano-silica can potentially strengthen the structures of C-S-H gel and siliceous hydrogarnet - the main hydration products, which presumably host heavy metals [92], [141].

Consequently, this chapter aims to investigate the combined effects of nanosilica addition and tri-potassium citrate concentration on the early age hydration of BOF slag. The reaction kinetics and early phase assemblage, analysed with in-situ and ex-situ XRD measurements, isothermal calorimetry and thermogravimetric analyses, are related to the mechanical properties of BOF slag mortars. This strategy is used to optimize the strength development of slag-based materials and, at the same time, to increase their durability.

4.2 Experimental

4.2.1 Materials

In this study, the BOF slag (2-5.6 mm grains) was ground with a vibratory disc mill (RS 300, Retsch) to the fineness characterized by the particle size distribution presented in Fig. 4.1, as measured with the laser diffraction spectroscopy method (Mastersizer 2000, Malvern).

The BOF slag was chemically and mineralogically analysed with the X-ray fluorescence (XRF) and the quantitative X-ray diffractometry (XRD), respectively. The results are presented in Table 4.1. The X-ray amorphous content in the BOF slag, most likely, partly

resulting from the grinding procedure accounts mostly for the C_2S phase, as shown in the previous chapter.

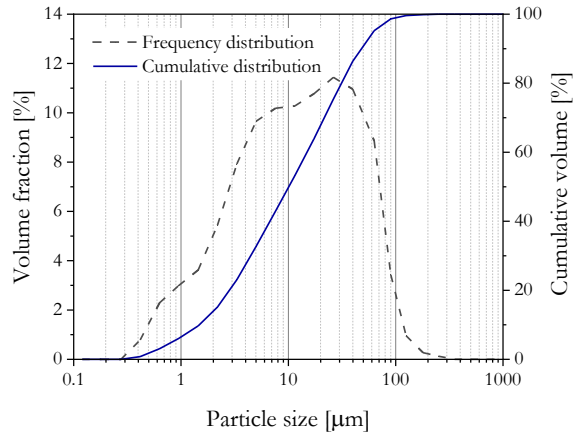


Figure 4.1: The frequency and cumulative distribution of the particle size of the slag powder.

Table 4.1: Chemical and mineralogical characteristics of BOF slag.

Mineral compound	Content [wt%]	Oxide	Content [wt%]
Brownmillerite	20.8	MgO	6.0
Magnetite	9.7	SiO ₂	12.0
C ₂ S	30.8	Al ₂ O ₃	3.2
Wuestite	19.7	CaO	41.0
Lime	1.1	P ₂ O ₅	1.4
Calcite	0.3	TiO ₂	1.1
Portlandite	0.6	V ₂ O ₅	1.1
C ₃ S	0.7	Cr ₂ O ₃	0.3
Amorphous	16.3	MnO	4.7
		Fe ₂ O ₃	29.0
		GOI 1000	0.14

Nanosilica, with 99.7% purity, was obtained through the dissolution of olivine (as described in detail in [142], [143]). The specific surface area (measured with BET method) of the synthesized nano-silica was about 400 m²/g and the specific density of 2.0 g/cm³. Tri-potassium citrate monohydrate (K₃C₆H₅O₇·H₂O, GPR RECTAPUR®, purity > 99%) was employed with a dual role of activator and superplasticizer. The CEN-standard sand was used for the preparation of mortars.

4.2.2 Mix design and sample preparation

The BOF slag pastes with and without the addition of nanosilica were prepared according to the mix design shown in Table 4.2. Nanosilica was applied by substituting 2 vol% of the slag. This relatively low dosage of nS was selected considering the high specific surface area (400 m²/g) of nS and the content of the potentially reactive phases in BOF slag [144]. The concentrations of tri-potassium citrate were chosen based on the findings from the previous chapter.

Table 4.2: The compositions of the mixtures for the preparation of the paste.

Sample ID	BOF slag [g]	nS (olivine) [g]	Water [g]	Activator [M]	w/b (mass ratio)	w/b (volume ratio)
C0.2	100	-	18	0.2	0.180	0.66
C0.6	100	-	18	0.6	0.180	0.66
C0.2nS2	98	1.087	18	0.2	0.184	0.66
C0.6nS2	98	1.087	18	0.6	0.184	0.66

For the preparation of pastes, nanosilica was firstly dispersed in 2/3 of water volume using the Hielscher UP400S ultrasonic device (15 min, with an amplitude of 75%). The temperature of the solutions was controlled with the ice water bath and kept at the level of 21±0.2 °C before application. The tri-potassium citrate monohydrate was dissolved in the remaining water. Both solutions were mixed with slag for 3 min using a high-speed mixer. Pastes were subsequently poured in the polyethylene vials and sealed cured (20 °C, RH > 95%) until the designed testing ages.

For the compressive strength evaluation, mortar prisms were prepared. To ensure sufficient workability of mortars (S4, according to EN 206-1), an additional amount of water was added, resulting in a water/binder mass ratio of 0.25. The sand content was adjusted to obtain a similar paste to sand volumetric ratio as for standard cement mortars, described in EN 196-1 (with a density of slag of about 3.85 g/cm³ vs. density of Portland cement equal to 3.15 g/cm³). In consequence, a sand to slag mass ratio of 2 was used. Mortars were prepared using a Hobart mixer following the procedure described in EN 196-1 but with extended mixing time (a total mixing time of 10 minutes was employed). Due to the high density of slag and the limited/late reactivity of the slag phases, bleeding problems were encountered during the samples' preparation. The impact of this phenomenon on the final

results should be considered and requires further investigation as some signs of bleeding were also observed on the paste level.

4.2.3 Methodology

The compressive strength and thermogravimetric measurements were conducted according to the procedures described in Section 2.2.2 and Section 3.2.2, respectively.

Isothermal calorimetry

The heat flow and cumulative heat release from the reacting BOF slag were monitored with an isothermal conduction calorimeter (TAM Air, Thermometric). The external mixing method was applied. Firstly, the tri-potassium citrate solution was prepared, and nanosilica was dispersed in water with an ultrasonic device. Then, both solutions were mixed with BOF slag for 2 min. Pastes were subsequently transferred to the glass ampoules and loaded into the calorimeter. The measurement temperature was set to 20 °C. For the evaluation of the total heat release, the integration of the heat flow curve was made from 45 min after the sample insertion, when the measurement conditions were stabilized.

X-ray diffraction (XRD)

Changes in the early age phase composition of the hydrating BOF slag pastes were monitored with the in-situ XRD method within the first 24 hours of hydration.

Table 4.3: Instrumental parameters for in-situ and ex-situ XRD measurements.

Parameter	Value	
	In-situ XRD	XRD on powder samples
Device	X'Pert Pro PANalytical	D4, Bruker AXS
X-ray tube	Co	Co
Voltage/Current	35 kV/45 mA	40 kV/40 mA
Detector	PIXcel ^{3D}	LynxEye
Scan range	10-70 °2θ	10-80 °2θ
Step size	0.026 °2θ	0.014 °2θ
Time per step	0.41 s	1 s

An X'Pert Pro PANalytical diffractometer in theta-theta geometry was used. For the preparation of pastes, the mixing procedure described in Section 4.2.2 was employed. Pastes were subsequently placed in the sample holders, flattened with a spatula and covered with a Kapton foil to minimize the water evaporation and CO₂ ingress. The measurements were

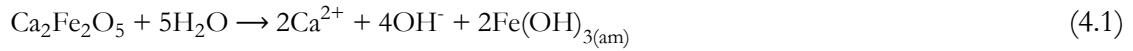
carried out with the settings listed in Table 4.3. Each diffraction pattern was recorded for about 15 min. At later hydration stages, the hydration of BOF slag pastes was arrested with the solvent exchange method (isopropanol, diethyl ether [145]). The XRD measurements were performed on the powder samples using a Bruker D4 X-ray diffractometer.

XRD interpretation

Quantitative phase analysis was performed by means of Rietveld refinement using the TOPAS Academic software v5.0. The external standard method (corundum) was employed. This method was chosen in order to be able to quantify phases independently, which is especially important when precipitating products reveal low crystallinity. The mass absorption coefficients of pastes were calculated based on the International Tables of Crystallography [146]. The crystal structures used for the Rietveld refinement are catalogued in the previous chapter (Table 3.2). The lattice parameters, crystallite size and microstrain of the slag phases were determined on anhydrous slag and then used unrefined for the phase quantification in hydrating slag. The broad XRD hump caused by the Kapton film, free water and amorphous content was modeled by introducing individual peaks. In order to account for the changes in the phase contents, the peak areas were refined, whereas the positions of the peaks were kept fixed. With the in-situ XRD method, only the pastes with 0.2 M K_3 -citrate were investigated. Due to the high liquidity of the pastes with 0.6 M K_3 -citrate and strongly alkaline pH of the pore solution, slight bleeding and deposition of carbonates (caused by partial destruction of the Kapton foil) were observed on the surface of the samples. It should be noted that these factors might affect the quantitative interpretation of the results.

Heat flow calculation

To validate the findings regarding the early age reactions taking place in BOF slag pastes obtained with calorimetry and in-situ XRD, the measured heat flow curves from the isothermal calorimeter were compared with the heat flows calculated from the in-situ XRD experiments [147]. This method enables verification of the contribution of the dissolution/precipitation processes assigned to the particular phase in BOF slag to the overall heat release during the investigated period of the hydration. Based on the previous studies [148], [149], the following equation was used to describe the reaction of brownmillerite, knowing that the composition of brownmillerite in BOF slag is slightly closer to C_2F than to C_4AF [101]:



$$\Delta H_{\text{R}(\text{C}_2\text{F})} = -429.21 \text{ [J/g]}$$

The precipitation of iron (III) hydroxide was assumed to take place during the first hours of hydration, as indicated in [150], [151], and later confirmed by Dilnesa et al. [91] for the C₄AF phase. During the hydration of C₂F, similar behaviour is expected. The formation of iron (III) hydroxides was previously observed in the hydrated C₂F phase [152].

Table 4.4: Enthalpies of formation used for the calculation of the heat flow.

Phase/ species	ΔH_f [kJ/mol]	Reference
Ca ₂ Fe ₂ O ₅	-2124.22	<i>Recalculated from</i> [153]
H ₂ O	-285.88	[154]
Ca ²⁺	-543.07	[154]
OH ⁻	-230.01	[154]
Fe(OH) _{3(am)}	-832	[154]

The enthalpy of the C₂F reaction was determined using the thermodynamic data listed in Table 4.4. In the next step, the heat flow was calculated according to equation (4.2) [148]. For the calculations, the phase contents derived from XRD measurements were smoothed with a Fourier filter [147].

$$\text{HF}_i(t) = \frac{dc_i(t)}{dt} \cdot \Delta H_{\text{R}(i)} \quad (4.2)$$

Where:

HF_i(t) the heat flow of phase i [mW/g] at the time t [h]

c_i(t) the content of phase i [wt%] at the time t [h]

ΔH_{R(i)} the enthalpy of reaction of phase i [J/g]

4.3 Results and discussion

4.3.1 Hydration kinetics

The hydration kinetics of BOF slag is strongly affected by the dosage of tri-potassium citrate, as already shown in more detail in the previous chapter. From Fig. 4.2, it can be seen that the change of K₃-citrate concentration from 0.2 M to 0.6 M results in the elimination of the induction period, which lasts about 4 hours for paste with 0.2 M K₃-citrate. The shape of

the "main peak" of the heat flow curve, associated with the reaction of BOF slag phases, is broader for a higher activator dosage, and the total amount of the heat released after 24 hours becomes slightly higher than for paste with 0.2 M citrate. With the addition of 2 vol% of nanosilica, for both K_3 -citrate concentrations, the hydration of BOF slag is delayed.

The retarding effect of nanosilica observed in our systems contradicts the accelerating function of nS in Portland cement systems [155]. During the hydration of Portland cement, nanosilica accelerates the reaction by offering additional nucleation sites and/or boosting the depletion of calcium ions from the pore solution. However, these effects seem to be outbalanced by other phenomena when BOF slag is activated by K_3 -citrate. One of the postulates is that potassium citrate interacts with nanosilica, and therefore, its availability to enhance the dissolution of BOF slag phases is lowered. Since at the early hydration stages, the pH of the pore solution of BOF slag paste is strongly affected by the K_3 -citrate dosage (ranging from ~ 12.8 for 0.1 M to 13.4 for 0.6 M during the first 30 minutes of hydration, see Chapter 5), the retardation effect can also be caused by a slight decrease of pH in the presence of nanosilica.

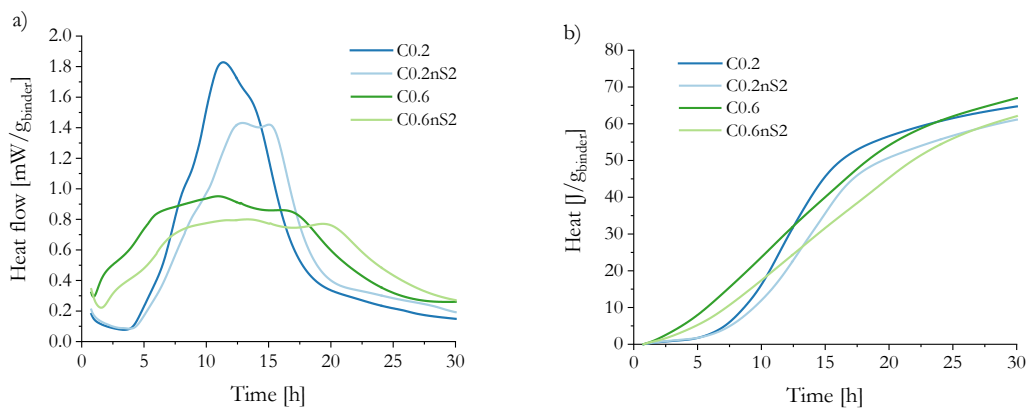


Figure 4.2: The isothermal calorimetry results of the investigated mixtures a) heat flow, and b) cumulative heat.

4.3.2 Phase assemblage

The changes in the phase composition of BOF slag pastes upon hydration are presented in Table 4.5. The quantitative XRD analyses reveal that at the early hydration stages, brownmillerite is the most reactive phase in BOF slag. The reaction of brownmillerite occurs mainly within the first day of hydration regardless of the concentration of potassium citrate. A greater extent of brownmillerite reaction is observed for the pastes with 0.6 M K_3 -citrate

than pastes with 0.2 M K₃-citrate. The addition of nanosilica results in a slightly delayed dissolution of this phase.

Next to brownmillerite, partial dissolution of wuestite is observed, in agreement with the finding from the previous chapter. In all pastes, the magnetite is relatively inert during the investigated hydration period. The crystalline C₂S reacts to a limited extent within 28 days of hydration, showing a slightly higher reaction degree when a lower dosage of K₃-citrate is applied. The main crystalline product of BOF slag hydration is siliceous hydrogarnet (Hg). Additionally, the formation of pyroaurite (Mg₆Fe³⁺₂(OH)₁₆[CO₃]·4H₂O) was detected with a broad reflection at 2θ = 13.5°. Due to very low contents and poorly crystalline structure of this phase, it is not included in Table 4.5.

Table 4.5: The phase composition of the BOF slag pastes after selected hydration periods.

	Time (day)	C ₂ (A,F)	C ₂ S	C ₃ S	Wuestite	Magnetite	Lime	CH	Cc	Hg	Am
C0.2	0	20.8	30.8	0.7	19.7	9.7	1.1	0.6	0.3	0.0	16.3
	1	10.2	29.2	0.7	17.5	9.0	0.5	1.1	0.1	10.5	26.4
	3	9.8	28.7	0.7	16.7	8.5	0.6	1.3	0.1	10.9	28.9
	7	10.2	27.7	0.7	16.8	8.7	0.6	1.7	0.2	11.0	29.3
	28	9.7	22.5	0.5	18.5	8.6	0.5	2.1	0.3	12.7	33.4
C0.2nS2	0	20.6	30.5	0.7	19.5	9.6	1.1	0.6	0.3	0.0	16.1
	1	10.9	29.8	0.7	16.8	8.9	0.6	0.8	0.2	8.8	27.8
	3	10.7	30.8	0.7	15.8	8.7	0.5	0.9	0.2	9.0	28.8
	7	10.1	28.5	0.8	16.1	8.7	0.5	0.9	0.2	9.8	31.1
	28	9.6	24.7	0.7	16.9	8.8	0.5	1.1	0.3	11.2	34.0
C0.6	0	20.8	30.8	0.7	19.7	9.7	1.1	0.6	0.3	0.0	16.3
	1	6.5	27.6	1.1	16.9	8.4	0.4	1.0	0.4	10.9	33.4
	3	5.4	28.1	0.8	13.9	8.5	0.5	1.0	0.2	13.4	36.3
	7	5.6	27.9	0.8	13.2	8.4	0.4	1.2	0.1	14.1	36.9
	28	4.8	26.3	0.7	11.9	8.3	0.3	1.8	0.2	15.5	39.5
C0.6nS2	0	20.6	30.5	0.7	19.5	9.6	1.1	0.6	0.3	0.0	16.1
	1	7.0	29.6	0.7	16.4	8.5	0.4	0.6	0.2	7.8	35.4
	3	5.7	28.5	0.8	15.1	8.5	0.5	0.6	0.2	11.4	36.8
	7	5.4	28.1	0.7	13.8	8.6	0.4	0.7	0.2	12.2	38.4
	28	5.0	26.2	0.8	13.1	8.4	0.5	0.7	0.3	13.3	40.9

4.3.3 Hydration of brownmillerite

Since brownmillerite is the most reactive crystalline phase in the examined systems and its reaction occurs mostly during the first 24 hours of hydration, the reaction kinetics of this phase becomes crucial for the setting time of pastes and their early age mechanical properties.

In-situ XRD experiments were carried out to reveal the impact of nanosilica addition on the reaction kinetics of brownmillerite.

Fig. 4.3 shows the phase evolution in hydrating BOF slag paste with 0.2 M potassium citrate with and without the addition of nanosilica. It can be seen that brownmillerite shows the highest reactivity among other phases and that the precipitation of hydrogarnets follows its hydration. A slight delay is observed in the system with nanosilica. Similar behaviour is expected for BOF slag paste with 0.6 M K_3 -citrate. Calorimetry data indicate that the dissolution of brownmillerite in that system starts immediately after contact with water.

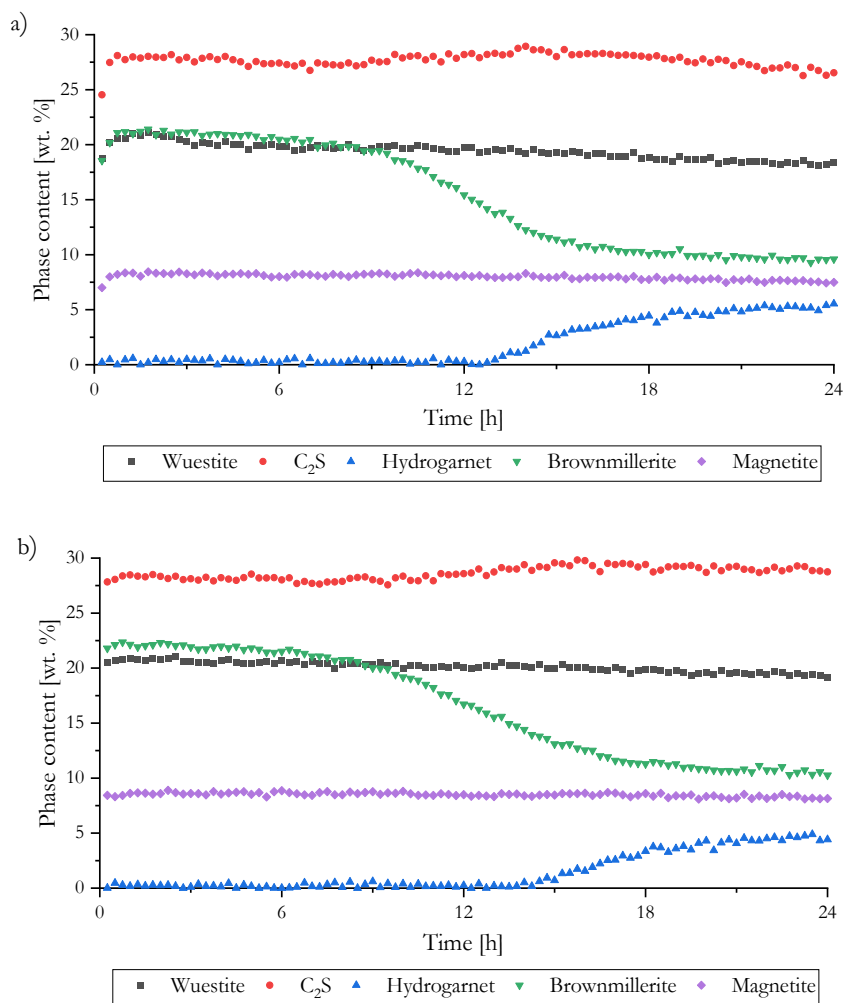


Figure 4.3: Phase development for BOF slag pastes a) C0.2, and b) C0.2nS2, derived from the in-situ XRD measurements.

A comparison between the calorimetry and in-situ XRD results (Fig. 4.4) shows that the shoulder on the heat flow curve on the right side of the main reaction peak (at around 13

hours for paste without nS and 15 hours for paste with nS) coincides well with the precipitation of hydrogarnets. The exact composition of hydrogarnets ($\text{Ca}_3(\text{Al}_x\text{Fe}_{1-x})_2(\text{SiO}_4)_y(\text{OH})_{4(3-y)}$) is difficult to establish as it can form a range of solid solution compositions [92]. A gradual uptake of SiO_4^{4-} in the structure of hydrogarnets is commonly observed [112]. Therefore, simplifications are required for the quantification of this phase, as described in [141]. The presented data show clear evidence for the formation of hydrogarnets in the investigated BOF slag systems. However, further studies are required to better understand the exact nature of this hydration product. Interestingly, the precipitation of crystalline hydrogarnets was not observed in the previous studies on the early hydration of synthesized brownmillerite [148], [149]. Even though it was shown that the majority of brownmillerite underwent dissolution during the initial 24 hours of hydration (either with or without the presence of gypsum), the formation of silicon-free hydrogarnet (katoite) was not observed. On the other hand, for Portland cement paste, the precipitation of hydrogarnets was detected between 16 and 24 hours of hydration [91]. This behavior indicates that the presence of silicate ions and/or pH of the pore solution are critical factors for the precipitation of crystalline hydrogarnets (at the early hydration stages). For matured Portland cement systems, siliceous hydrogarnets are considered the most stable iron-containing hydrates, being the reaction products of brownmillerite and $\text{C}_2\text{S}/\text{C}_3\text{S}$ [127], [111].

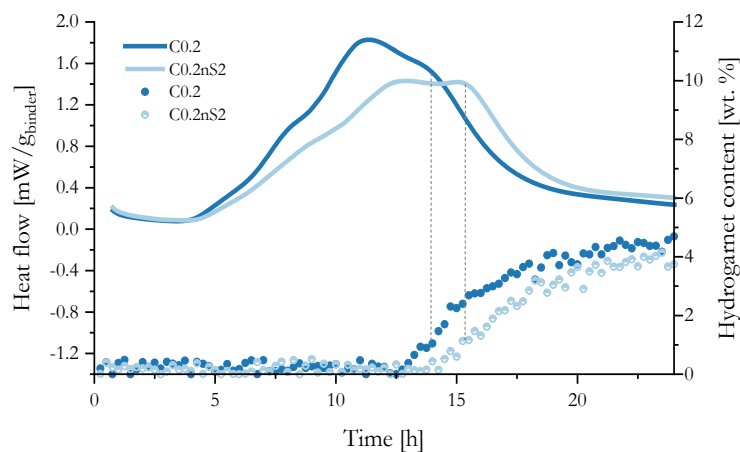


Figure 4.4: Heat flow curves derived from the calorimetry measurements and hydrogarnet content during hydration of slag in C0.2 and C0.2nS2.

4.3.4 Hydration of silicate

Since part of C_2S in BOF slag is XRD-amorphous (see Chapter 3), and its potential reaction is not detectable with the XRD method, the heat flow curves from calorimetric

measurements were compared with the curves calculated from in-situ XRD data. The brownmillerite was considered the only hydrating crystalline phase during the first 24 hours of hydration (see Fig. 4.3). The slight dissolution of other crystalline phases (as shown in Table 4.5) was not taken into account, being assigned mostly to the initial dissolution (after contact with water), which is not analysed in this study. Fig. 4.5 reveals good agreement between the measured and calculated heat flow curves for pastes with 0.2 M of potassium citrate. The satisfactory correspondence regarding the positions (time) and shapes of the curves confirms that the evolved heat is mainly due to the reaction of brownmillerite. The difference between the measured and calculated heat can be explained by the presence of aluminum in brownmillerite (which is not considered in the proposed reaction) but also likely originates from the dissolution of amorphous C_2S and precipitation of hydrogarnet. It is generally accepted that α' - C_2S polymorph, which coexists in BOF slag with β - C_2S (commonly observed in Portland cement), reveals higher reactivity than the β -polymorph. Knowing that the potassium citrate is boosting the pH of the pore solution (see Chapter 5), the early age dissolution of this phase is expected to occur, especially in samples with 0.6 M K_3 -citrate [87].

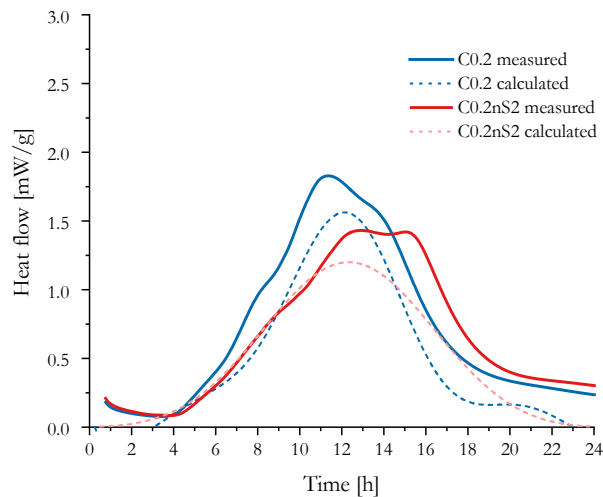


Figure 4.5: The comparison of the heat flow of hydrating BOF slag pastes measured with isothermal calorimetry and the heat flow calculated from the reaction of C_2F based on the in-situ XRD data.

To further support this hypothesis, thermogravimetric measurements were conducted. The mass loss due to the dehydration of C-S-H gel after selected hydration times was used to indicate the differences in the extent of C_2S reaction in the investigated pastes. Similarly, the

precipitation of hydrogarnets, resulting from the reaction of brownmillerite (and C_2S), was followed. An exemplary DTG curve is shown in Fig. 4.6a.

For the hydrated BOF slag, the mass loss occurs due to the decomposition of C-S-H gel, hydrogarnets, pyroaurite, portlandite, and carbonates/citrate compounds. It is widely reported that the dehydration of C-S-H gel in cement paste takes place within a broad temperature range (up to 400/500 °C), with the main water release at around 100 °C [156], [157]. For the gel products of alkali activation, with aluminum and alkali metals in the structure, the water loss is observed within a similar temperature range [158]. At the same time, depending on the chemical composition, the decomposition of hydrogarnets occurs between 200-400 °C [92]. Pyroaurite decomposes between 180 and 410 °C [116] and portlandite between 400 and 500 °C [145]. Overlapping of the temperature ranges in which the water is released from different hydration products precludes the quantitative analysis of the results. Nevertheless, based on the literature and the shape of DTG curves observed for hydrated BOF slag, the temperature intervals assigned to the water loss from different hydration products were selected to demonstrate the differences in the hydration kinetics of slag phases. As presented in Fig. 4.6a, it was assumed that mass loss between 40-180 °C originates mostly from the dehydration of C-S-H gel, whereas between 180-410 °C from the dehydration of hydrogarnet and, to a smaller extent, pyroaurite. Additionally, the total mass loss due to the water release was analysed in the range between 40 and 500 °C, as recommended in [145]. It has to be noted, however, that the presented temperature ranges cannot be exclusively assigned to the decomposition of a particular hydration product (e.g., decomposition of C-S-H gel takes place up to 500 °C) and therefore have only indicative character.

From Fig. 4.6b, it can be seen that the mass loss between 40 and 180 °C is generally higher for BOF slag pastes with 0.6 M of K_3 -citrate during the first 7 days of hydration, indicating a greater extent of C_2S reaction in these samples. This behaviour can be directly related to the higher pH of the pore solution during the early hydration of BOF slag in pastes with 0.6 M of K_3 -citrate in comparison to the pastes with 0.2 M of K_3 -citrate [159]. Furthermore, the addition of nanosilica results in the enhanced precipitation of C-S-H gel. This observation strongly suggests that nanosilica is consumed in the pozzolanic reaction, resulting in lower portlandite contents (as shown in Table 4.5), rather than being incorporated in the structure of hydrogarnet.

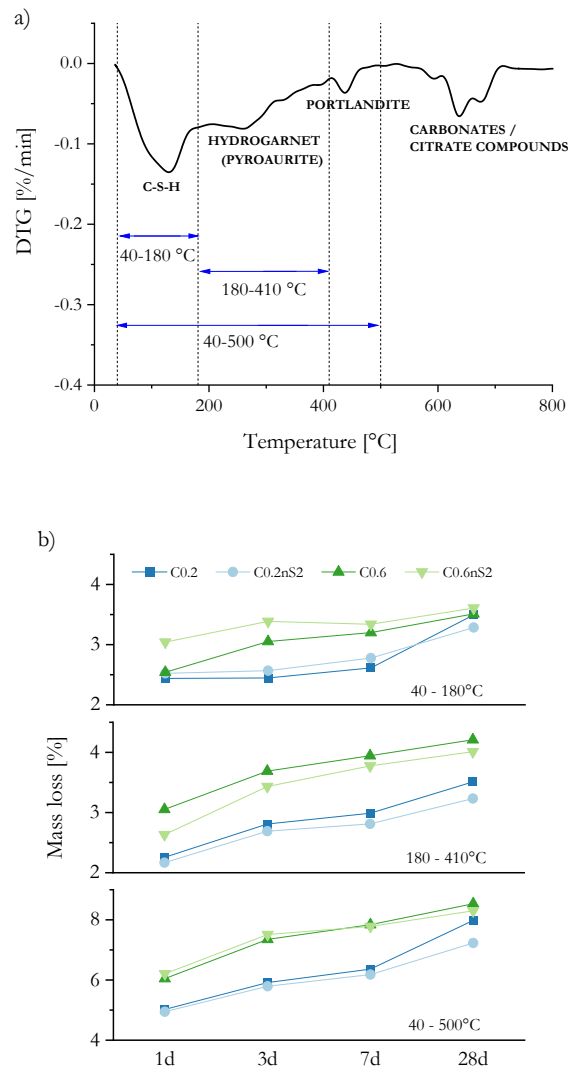


Figure 4.6: The thermogravimetric results showing a) the exemplary DTG curve of hydrated BOF slag b) the mass loss from BOF slag pastes due to the water release within the selected temperature intervals.

However, the accelerating effects of pH and likely also nS addition are less pronounced after 28 days of hydration, which is especially evident for the pastes with 0.2 M of K_3 -citrate, in which a higher mass loss is observed for the sample without nanosilica. Similarly, the differences in the mass loss between the pastes with the different dosages of potassium citrate are minimized or eliminated at this age. From the abovementioned observations it can be concluded that the enhanced early age hydration of C_2S adversely affects the late reaction of this phase.

The mass losses in the temperature range between 180 and 410 °C, mostly due to dehydration of hydrogarnets, correlate well with the findings from the XRD analyses. The

mass loss is substantially higher for the pastes with 0.6 M of K_3 -citrate than for pastes with 0.2 M of K_3 -citrate. For both activator dosages, the delayed reaction of brownmillerite and consequent precipitation of hydrogarnets are also reflected in the presence of nanosilica.

At the same time, the total mass loss due to the water release from the hydration products shows the combination of the two opposite effects of nanosilica, which enhances the precipitation of C-S-H gel while having a negative impact on the hydration of brownmillerite at the early hydration ages. In consequence, no substantial differences in the bound water content between the reference samples and the samples containing nanosilica are observed. Nonetheless, it is worth mentioning that after 28 days of hydration, the samples without nanosilica addition tend to contain more chemically bound water.

4.3.5 Mechanical performance

In the previous chapter, it was shown that the BOF slag paste can reach a strength of up to 75 MPa after 28 days of hydration (when 0.2 M potassium citrate is applied) [160]. However, it has been often reported that for alkali/chemically activated binders, the transition from paste to mortar causes a significant decline in performance due to higher water demand [161]. In this study, the mechanical performance was investigated on the mortar samples, and therefore, additional water had to be added to the mixtures to provide sufficient flowability. In consequence, the potassium citrate solutions were diluted, and the kinetics of BOF slag hydration was affected. Nevertheless, the observed changes in the mechanical performance provide significant insight into the effects of early slag hydration kinetics on the later phase development, especially the hydration of C_2S (the most abundant phase in BOF slag).

Fig. 4.7 shows the compressive strength results for the BOF slag mortars. The mortars with 0.6 M potassium citrate reveal accelerated strength development in comparison to the mortars with 0.2 M K_3 -citrate. After 3 and 7 days of curing, the difference in the strength of 64% and 35% is observed, respectively. After 28 days, however, higher compressive strength is reported for mortars with a lower concentration of potassium citrate. The addition of nanosilica improves the compressive strength of mortars with 0.6 M K_3 -citrate after all the investigated curing periods. For mortars with 0.2 M K_3 -citrate, strength increase is observed after 3 and 7 days, while after 28 days, mortars with nanosilica show a decline in strength compared to the reference samples.

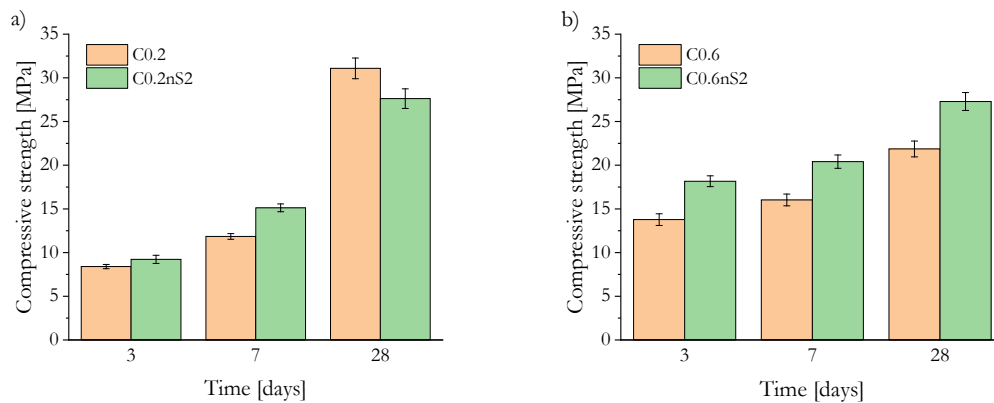


Figure 4.7: The compressive strength of BOF slag mortars after selected curing periods.

The XRD and thermogravimetric analyses on pastes disclose that nanosilica delays the hydration of brownmillerite and enhances the precipitation of C-S-H gel. Furthermore, it is revealed that in the pastes with 0.6 M of K_3 -citrate, the early hydration of amorphous C_2S is promoted. The improved early-age performance of BOF slag mortars with the higher activator dosage and with nS addition at the early hydration stages indicates that the C-S-H gel is a principal strength-giving phase, whereas hydrogarnets have a lesser impact on the mechanical properties of BOF slag mortars. Furthermore, the increased early age reactivity of C_2S seems to have a negative influence on its overall hydration degree, and therefore, after 28 days of hydration, the highest mechanical performance is observed for the mortar without nanosilica and with a low concentration of K_3 -citrate.

4.4 Conclusions

This chapter focuses on the early age hydration of BOF slag. Special attention is paid to the impact of nanosilica and K_3 -citrate concentration on the hydration kinetics of the slag phases. The compositional changes in the slag pastes are related to the mechanical properties of mortars. The following conclusions are reached.

- The early hydration of BOF slag activated with K_3 -citrate is dominated by the reaction of brownmillerite and, to a lesser extent, of amorphous C_2S , leading primarily to the formation of hydrogarnets and C-S-H gel.
- The kinetics of the brownmillerite reaction can be controlled by adjusting the dosage of potassium citrate (where hydration is accelerated about by 4 hours for samples with 0.6 M K_3 -citrate compared to the samples with 0.2 M K_3 -citrate).

- Highly concentrated solutions of K_3 -citrate increase the early age reactivity of C_2S .
- Silica nanoparticles (at the dosage of 2 vol%) delay the reaction of brownmillerite while enhancing the formation of C-S-H gel.
- Mortars with nS addition and highly concentrated potassium citrate solutions (0.6 M) exhibit improved early age mechanical properties. Increased compressive strength is associated with the accelerated hydration of C_2S / precipitation of C-S-H gel. However, the accelerated early reaction of C_2S has an adverse effect on its late reactivity resulting in limited strength development up to 28 days

Effects of carbonation on the retention of heavy metals in chemically activated BOF slag pastes

Basic Oxygen Furnace slag contains heavy metals, including vanadium, chromium and molybdenum. The leachability of these elements determines the industrial applicability of slag-based building products. This chapter investigates the post-carbonation leaching of heavy metals from activated BOF slag pastes, with the focus on the activator dosage and type (sodium and potassium citrate). Results reveal that the high extent of brownmillerite hydration boosts the leachability of heavy metals, as its hydration product - hydrogarnet, is less stable upon carbonation. With two leaching procedures, it is demonstrated that the carbonation resistance of pastes becomes the main attribute in preventing the leaching of heavy metals. It can be enhanced by optimising the activator dosage to facilitate the hydration of C_2S and consequent structural densification.

5.1 Introduction

Even though concrete technology offers a promising field for BOF slag utilization, its application as a binder constituent seems thus far precluded, mainly due to contamination with heavy metals and low reactivity [83], [85]. In BOF slag, C_2S and $C_2(A,F)$ are potentially the most reactive, but at the same time, they are reported to be the host phases for vanadium and $C_2(A,F)$ also for chromium [101], [162], [163].

In order to evaluate the hazardous impact of BOF slag on the environment, many studies focus on the leaching of heavy metals from the original material. In general, it is shown that non-weathered slags release relatively low quantities of vanadium and chromium [164], [165]. According to Chaurand et al. [163], [166], in BOF slag chromium is present as Cr(III)

Reproduced from:

Kaja, A. M., Delsing, A., van der Laan, S. R., Brouwers, H. J. H., & Yu, Q. L. Effects of carbonation on the retention of heavy metals in chemically activated BOF slag pastes. Submitted.

(octahedral coordination) which is less mobile and less toxic than Cr(VI) and remains at this oxidation state during leaching. In consequence, the release of Cr from BOF slag is minor. The leaching values of vanadium are usually higher than those of chromium. Nonetheless, they often fall below the standardized limits for heavy metals leaching [105], as at highly alkaline conditions (e.g., in the presence of portlandite) vanadium is relatively immobile [76].

The weathering, however, greatly affects the release of heavy metals from BOF slags. Costa et al. [167] showed that while leaching of chromium remains the same or becomes slightly reduced after carbonation, leaching of vanadium from carbonated slag can increase even 500 times. In BOF slag, vanadium predominately prevails at V(IV) and V(V) [163], [168]. However, during natural ageing, V(IV) is oxidized to V(V), being the most toxic oxidation state [163], [166]. Significant release of vanadium from BOF slag after carbonation coincidences mainly with the pH drop caused by the reaction of portlandite with CO₂ [169].

The leaching behavior of the non-hydrated, loose slag powder cannot be directly transferred to the leaching behaviour of slag-based shaped building materials. In Chapter 3, it is demonstrated that the problem of low reactivity of slag can be overcome with the addition of tri-potassium citrate. Chemical activation significantly enhances the hydration of BOF slag, and as a consequence, high-end performance building products can be manufactured. In the proposed activation process, the reaction of the most contaminated phases - brownmillerite and belite takes place, resulting in the formation of siliceous hydrogarnet and C-S-H gel (see Chapter 3). These hydration products are known to reveal high capacities for heavy metals immobilization. Hydroandradites $\text{Ca}_3(\text{Al}_x\text{Fe}_{1-x})_2(\text{SiO}_4)_y(\text{OH})_{4(3-y)}$, belonging to the hydrogarnet group, can incorporate heavy metals in their structure by substituting aluminum/iron in octahedral positions or hydroxyls ($\text{H}_4\text{O}_4^{4-}$) in tetrahedral positions. Accordingly, in hydrogarnets, chromium (III) substitutes iron/aluminum [125], and chromium (VI), in the form of oxyanions (chromate (CrO_4^{2-})), substitutes hydroxyls [113]. With a similar size as chromium oxyanions, vanadium oxyanions (VO_4^{3-}) could also potentially replace the hydroxyls in hydrogarnets structure. However, this would require charge balancing. Vollpracht et al. [123] suggested that in hydrating cement, vanadium oxyanions are adsorbed on the C-S-H gel. Immobilization of chromium in C-S-H gel by means of Si substitution is also sometimes proposed [122], [170], [171].

The high immobilization potential of BOF slag hydration products was confirmed in Chapter 3. Well-sealed samples of chemically activated BOF slag did not reveal leaching

problems even though the phases containing heavy metals underwent hydration. However, similarly as observed in the raw BOF slag, the carbonation of hydration products can lead to the increased release of heavy metals. Upon carbonation, changes in the phase composition occur and are accompanied by a significant pH reduction. The C-S-H gel and hydroandradite (phases that are potentially hosting heavy metals in the hydrated BOF slag) are known to undergo carbonation. The reaction of C-S-H gel with CO₂ leads to the formation of calcite and amorphous silica [172], [173]. Carbonation of hydrogarnets also takes place, as predicted with thermodynamic modeling [174]. The data are however, limited and mainly focused on the carbonation of Al-based hydrogarnets.

Regarding the release of heavy metals from the shaped BOF slag-based products, carbonation resistance, defined as the depth where the compositional changes and the drop of pH occur, may become a crucial factor controlling the applicability of these materials. Therefore, the extent and impact of carbonation on the leaching of heavy metals need to be evaluated, considering not only the release of heavy metals from the dissolving phases but also the possibility of their further immobilization in the newly formed carbonation products.

Following the above discussion, this chapter focuses on the hydration of newly designed chemically activated BOF slag-based materials and their resistance to carbonation in order to evaluate the retention of heavy metals during their service life. For the representativeness of this study, two types of citrate-based activators (with varying concentrations) and two leaching procedures are employed. To account for the chemical and physical factors affecting the release of heavy metals, the leaching from unshaped and shaped slag pastes is analysed before and after carbonation in the context of reactivity of the slag phases, hydration products, carbonation resistance of pastes and compositional changes induced by the carbonation. The results demonstrate that the leaching of heavy metals from BOF slag pastes increases significantly after carbonation, mainly due to the decomposition of hydrogarnets and C-S-H gel. Nevertheless, the current observations show that this effect can be minimised by optimising the initial mix design. Higher hydration degrees of C₂S after 90 days of curing in pastes with 0.1 M and 0.2 M solutions of citrate salts than in pastes with more concentrated solutions lead to microstructural densification and consequent improvement of the carbonation resistance.

5.2 Experimental

5.2.1 Materials

The BOF slag was ground prior to the application, and the particle size distribution is shown in Fig. 5.1, as measured with laser diffraction spectroscopy (Mastersizer 2000, Malvern).

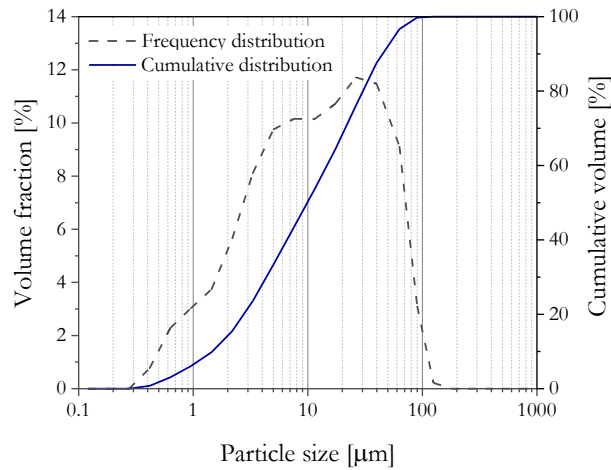


Figure 5.1: The particle size distribution of BOF slag.

The chemical and mineralogical compositions were determined respectively with X-ray fluorescence (XRF) and X-ray diffraction (XRD) with quantitative Rietveld refinement, as described in more detail in the methodology section. The results are presented in Table 5.1.

Table 5.1: Oxide and phase composition of BOF slag.

Mineral compound	Content [wt%]	Oxide	Content [wt%]
Brownmillerite	21.6	MgO	6.0
Magnetite	11.3	SiO ₂	11.9
C ₂ S*	32.1	Al ₂ O ₃	3.2
Wuestite	20.6	CaO	41.0
Lime	1.1	P ₂ O ₅	1.4
Calcite	0.3	TiO ₂	1.1
Portlandite	0.5	V ₂ O ₅	1.1
C ₃ S	0.9	Cr ₂ O ₃	0.3
Amorphous	11.6	MnO	4.7
		Fe ₂ O ₃	29.1
		GOI 1000	0.01

* Polymorphs of C₂S are reported combined with a single value.

The distribution of heavy metals within the BOF slag phases, as determined with electron probe microanalysis (EPMA), is presented in Table 5.2. The measurements were performed with a Cameca SX 100 microprobe, using an accelerating voltage of 15 kV (a minimum of 19 points per phase were analysed on 10 different slag fragments).

Table 5.2: Chemical composition of the phases containing heavy metals, derived from EPMA analyses (wt%) including the 1sigma variation in the elements of interest, Cr and V.

Mineral	MgO	Al ₂ O ₃	SiO ₂	P ₂ O ₅	CaO	TiO ₂	V ₂ O ₃	σ	Cr ₂ O ₃	σ	MnO	FeO/ Fe ₂ O ₃ *	Total
C ₂ S	0.2	0.9	28.9	3.8	61.5	0.6	0.8	0.4	0.0	0.0	0.2	1.1	97.9
Wuestite	24.5	0.2	0.0	0.0	2.5	0.0	0.1	0.1	0.8	0.3	11.9	59.1	99.2
Brownmillerite	4.0	9.2	4.3	0.4	40.3	5.2	1.7	0.8	0.7	0.7	2.3	31.4*	99.4

To activate the BOF slag phases, potassium and sodium salts of citric acid were applied in this study. Technical grade products were used, tri-potassium citrate monohydrate (K₃C₆H₅O₇·H₂O) (GPR RECTAPUR[®]) and tri-sodium citrate dihydrate (Na₃C₆H₅O₇·2H₂O), both with > 99% purity.

5.2.2 Methodology

5.2.2.1 Mix design and sample preparation

Table 5.3: Mix design of the BOF slag pastes.

Sample description	BOF slag [g]	Water [g]	Tri-potassium citrate monohydrate [M]	Tri-sodium citrate dihydrate [M]	w/b	Flowability [mm]
K0.1	100	18	0.1		0.18	160
K0.2	100	18	0.2		0.18	240
K0.4	100	18	0.4		0.18	250
K0.6	100	18	0.6		0.18	280
Na0.1	100	18		0.1	0.18	150
Na0.2	100	18		0.2	0.18	200
Na0.4	100	18		0.4	0.18	220
Na0.6	100	18		0.6	0.18	250

Two series of BOF slag pastes with increasing content of sodium and potassium citrate were prepared and analysed in this study. The concentrations of the citrate salts were selected based on the finding presented in Chapter 3. Water to binder ratio (w/b) of 0.18 was applied

for all mixtures. The detailed mix proportions are presented in Table 5.3. The activators were firstly dissolved in water to obtain the designed molarity. Solutions were subsequently mixed with slag powder using a high-speed mixer for 3 min.

Owing to the superplasticizing properties of citrate salts and a broad range of concentrations investigated in this study, slight bleeding was observed for some samples, which was attributed to the high dosage of superplasticizer and/or late reaction of BOF slag (see calorimetry results). This, however, did not have a substantial impact on the results, as revealed e.g. with the compressive strength test. The water amount was kept fixed as the spacing factor plays a vital role in the hydration of the C₂S phase [112]. The flowability of pastes, measured using a Hägermann cone, is presented in Table 5.3.

5.2.2.2 Evaluation of the hydration process

The isothermal calorimetry measurements were conducted according to the procedure described in Section 2.2.2. The thermogravimetric, XRD and compressive strength measurements were performed following the descriptions presented in Section 3.2.2.

Pore solution analysis

Pore solutions were extracted from the fresh pastes after 30 and 60 min of hydration with pressure filtration. In order to remove possibly remaining solids, the solutions were subsequently filtered through a 0.22 µm membrane filter before the analyses. The concentration of OH⁻ was determined via titration against hydrochloride acid (0.1 mol/L), as described in [175]. The solutions were analysed with an ion chromatograph (Thermo scientific Dionex 1100, conductivity measurement), and after acidification with concentrated HNO₃, with inductively coupled plasma atomic emission spectrometer (ICP-OES, SPECTROBLUE). The multi-element standards IV and VI from Merck were used for the calibrations.

The concentration of citrates was determined with an ion chromatograph equipped with ion-exchange column AS9-HS (2 x 250 mm). The 25 mM sodium carbonate (Na₂CO₃) / 12 mM sodium bicarbonate (NaHCO₃) was used as an eluent. Citrate ions were detected via suppressed conductivity (Thermo scientific Diones AERS 500, 2 mm). The external standards for the calibration (200, 100, 50, 20, 10, 5, 2,1 and 0.5 mg/l) were prepared from the citrate standard for IC (Merck, 1000±5 mg/l).

5.2.2.3 Carbonation resistance and heavy metals retention

To evaluate the post-carbonation leaching behaviour, the leaching tests were performed on hydrated BOF slag pastes before and after carbonation curing. Two leaching tests were selected, the tank leaching test (EA NEN 7375:2004) [176] and the one batch leaching test (EN 12457) [177]. The BOF slag pastes were prepared with the same procedure as for the compressive strength determination. The first series of pastes (for the tank test) was cast in cubic moulds ($40 \times 40 \times 40 \text{ mm}^3$) and covered with foil to prevent moisture loss and carbonation. After 24 hours, samples were demoulded and sealed with foil and adhesive tape. The second series of pastes (for the one batch leaching test) was cast in cylindrical polyethylene vessels sealed with parafilm. All the samples were cured in the climate chamber ($20 \text{ }^\circ\text{C}$, $\text{RH} > 95\%$) for 90 days before testing. After the designed hydration period, cylindrical pastes were crushed and sieved in two fractions, the first fraction of 2-4 mm (G) and the second fraction $< 0.2 \text{ mm}$ (P). These fractions were selected to determine the factors affecting the leaching properties and at the same time, to meet the requirements of EN 12457-2 standard, which specifies the particle size range between 0 and 4 mm. To evaluate the compositional changes in the original slag and slag pastes upon carbonation, the thermogravimetric analyses and XRD measurements were performed on this fraction after carbonation.

Carbonation

The hydrated pastes and raw BOF slag were inserted into the carbonation chamber for 3 months. The conditions of carbonation curing: 3% CO_2 and $\text{RH} = 65\%$ were chosen based on the previous studies in order to mimic the natural carbonation and to enable reasonable time of the experiments [172], [178]. Phenolphthalein was used as a pH indicator to estimate the carbonation depth.

Leaching of heavy metals

The tank leaching test was performed according to EA NEN 7375:2004 standard. It should be noted that the size of the samples ($40 \times 40 \times 40 \text{ mm}^3$) was slightly below the limits specified by the standard, where the minimal size of two sample dimensions should be higher than 40 mm. Following the standard procedure, the carbonated and uncarbonated pastes were immersed in ultra-pure water (0.055 uS/cm) in sealed containers in a way that all sides were in contact with water. The eluates were exchanged periodically as specified in

the standard for up to 64 days. Similarly, crushed samples and original slag were analysed before and after carbonation curing by subjecting them to the one stage batch leaching test according to EN 12457-2. The L/S ratio of 10 was applied in all cases. The samples were inserted in plastic containers with ultra-pure water and shaken at a speed of 250 rpm for 24h using a dynamic shaker (ES SM-30, Edmund Buhler GmbH). The eluates were filtered through a 0.22 μm membrane filter and the pH was measured with a pH meter (Volcraft) calibrated with the 3-point procedure (with the accuracy of ± 0.2 pH). To determine the leaching of heavy metals, the eluates were acidified with HNO_3 and analysed with an inductively coupled plasma atomic emission spectrometer (ICP-OES, SPECTROBLUE). The obtained concentrations of heavy metals (in mg per kg of dry slag) were compared with the limit values specified in the Dutch Soil Quality Decree [105].

5.3 Results analysis

5.3.1 Hydration of BOF slag phases

The early age hydration kinetics of activated BOF slag was investigated with isothermal calorimetry, as presented in Fig. 5.2.

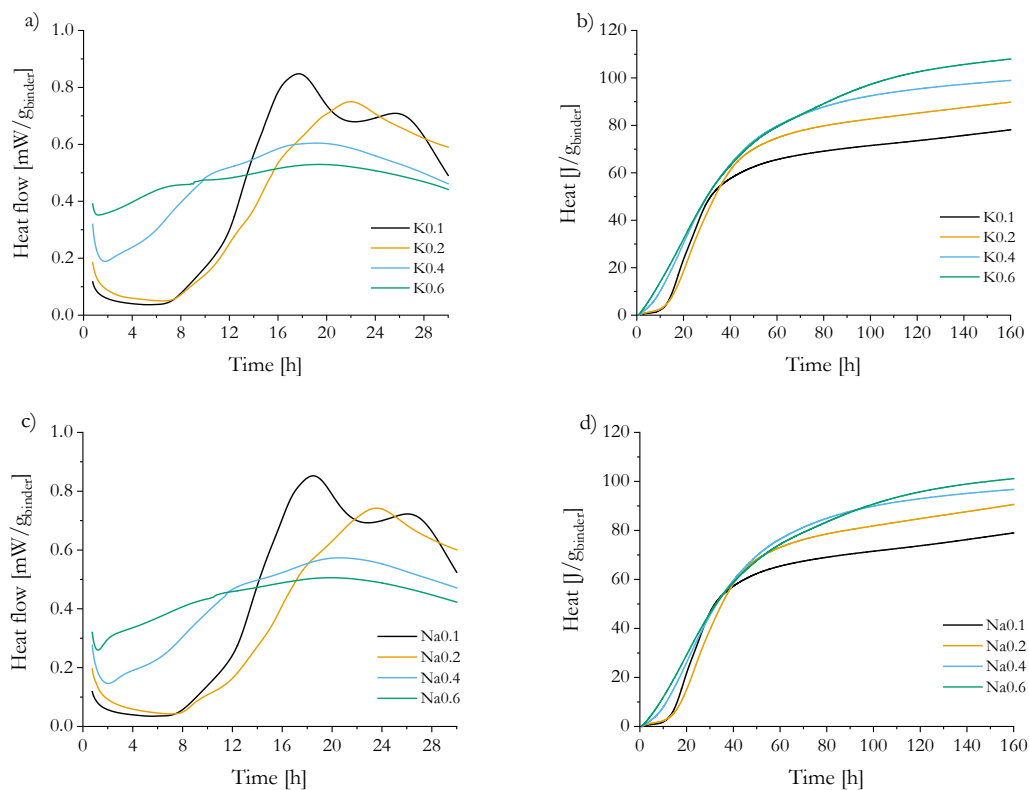


Figure 5.2: Heat flow curves a), c), and cumulative heat release b), d) during the hydration of BOF slag pastes.

No substantial differences are observed between the heat flow curves of potassium and sodium citrate-activated slag, reflecting similarity in the hydration processes when these two activators are applied. After 7 days of hydration, the total heat release is slightly higher for the samples with tri-potassium citrate. In general, higher concentrations of citrate salts result in an increased amount of total heat, indicating enhanced hydration of BOF slag up to 7 days. One must note, however, that the time of heat flow maximum is greatly affected by the activator dosage, being around 18 hours for 0.1 M of citrate salt, shifting towards longer times of around 22 hours for 0.2 M, and being again accelerated with 0.4 and 0.6 M solutions. Moreover, with the high activator dosages (e.g. 0.4 M, 0.6 M), the broadening of the main peak and elimination of the induction period is observed. Based on these findings, it can be concluded that citrate salts act as hydration retarders at low concentrations, whereas reversing their role when highly concentrated accelerating the hydration. This behaviour was previously reported in [106].

To understand the impact of activator concentration on the dissolution of BOF slag phases and their reactivity, as shown with the calorimetric curves, pore solution from pastes containing the highest and lowest activator dosage was extracted and analysed during the first hour after contact with water. The results are presented in Fig. 5.3 and Table 5.4.

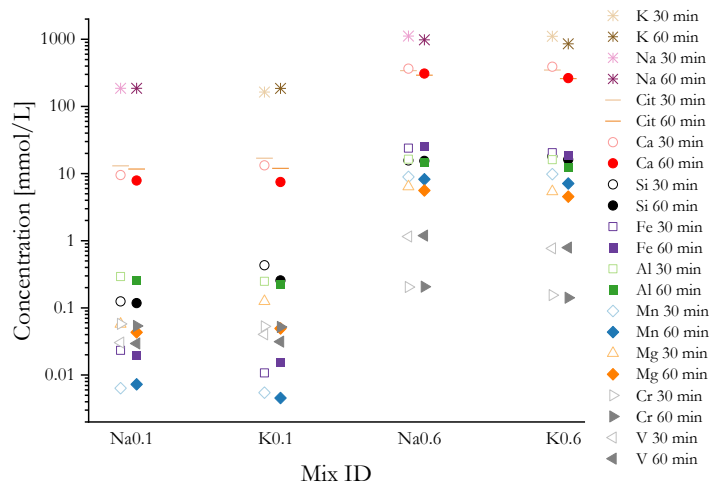


Figure 5.3: The concentrations of ions in the pore solution of pastes with 0.1 M and 0.6 M citrate salts (potassium citrate and sodium citrate).

Fig. 5.3 shows that the concentration of all ions in the pore solution of BOF slag pastes drastically rises when 0.6 M solutions of citrate salts are applied in comparison to 0.1 M solutions. It is evident that with the addition of citrate salts, extraordinarily high numbers of

Ca ions are released to the solution. This behaviour is in agreement with the results reported by Schwarz [96], who investigated the impact of tri-potassium citrate on cement hydration. High concentrations of iron, aluminum as well as heavy metals (chromium and vanadium) confirm the dissolution of brownmillerite at an early age (see Table 5.3). Chromium may also originate from wuestite, as magnesium and manganese are also present in the pore solution with significant quantities. The dissolution of wuestite seems to be enhanced with more concentrated solutions of citrate salts. The escalated contents of multivalent cations (including aluminum, iron and magnesium) in the pore solution were previously observed in the presence of organic admixture (polycarboxylate ether) in cement pastes [179]. It must be noted that pH is also significantly altered with the variable content of citrate salts compared to the intrinsic pH of a BOF slag-water mixture of about 12.5 [76], as shown in Table 4. The higher pH values are generated in pastes with more concentrated solutions of citrate salts after 30 and 60 minutes of hydration.

Table 5.4: The pH of the pore solutions.

Mix	pH		
	Before mixing	30 min	60 min
K0.1	9.03	12.78	12.95
K0.6	8.99	13.41	13.29
Na0.1	8.81	12.98	12.95
Na0.6	8.56	13.79	13.62

The phase development of BOF slag pastes after selected hydration periods is presented in Fig. 5.4. As already indicated with the calorimetry measurements, the hydration kinetics and phase assemblage are affected by the concentration of the citrate, whereas the cation of the salt (Na vs. K) has a minor effect. Among the crystalline phases, during the first 7 days of hydration, mostly brownmillerite reacts, and the extent of the hydration of this phase is enhanced with highly concentrated citrate salts solutions. The degree of brownmillerite hydration is relatively stable at later ages. Magnetite remains inert within the investigated hydration period, while wuestite reveals partial reactivity. The extent of hydration of crystalline C₂S is similar in all pastes after 7 days of hydration, disclosing a slight tendency towards higher reaction degrees with more concentrated citrate solutions. After 28 and 90 days, however, it becomes evident that hydration of C₂S in these latter samples is suppressed. In contrast, in pastes with 0.1 M and 0.2 M citrate salts, hydration of C₂S proceeds up to 90

days, reaching a hydration degree of around 50%. The main crystalline hydration product in the investigated systems is siliceous hydrogarnet, and its amount closely corresponds to the extent of brownmillerite hydration.

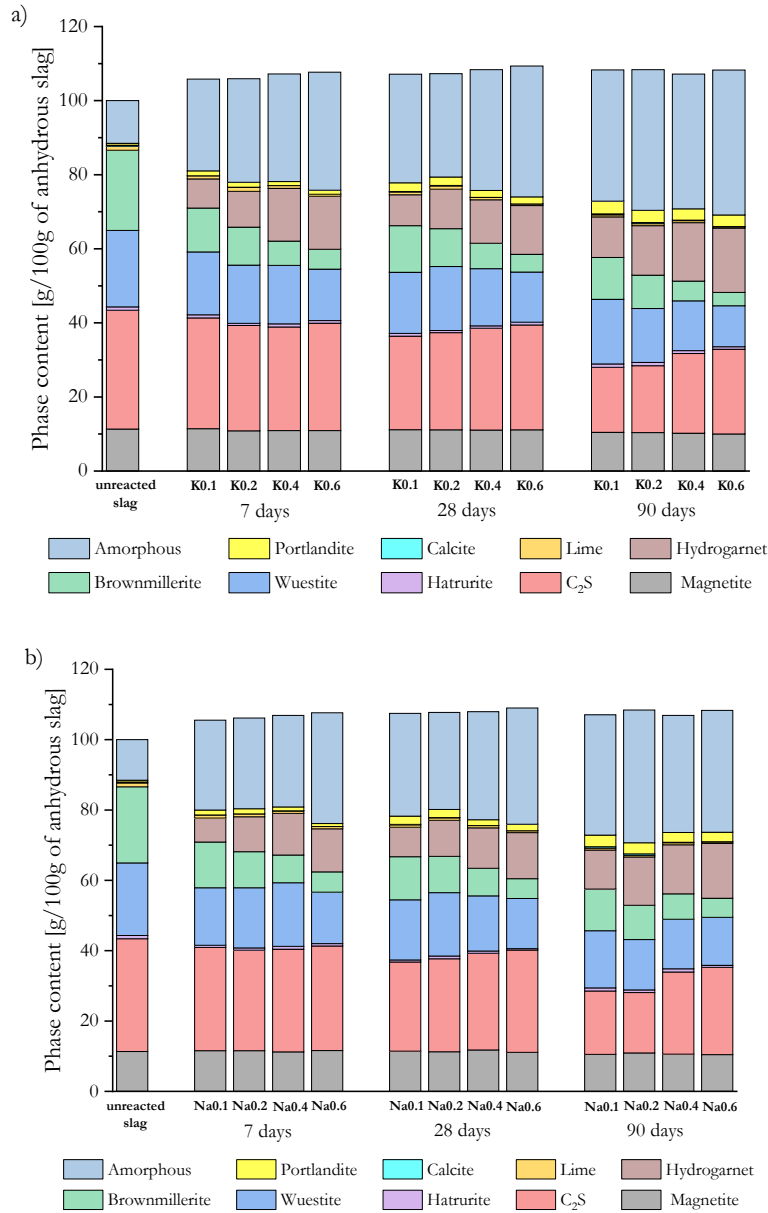


Figure 5.4: Phase compositions of the BOF slag pastes after selected hydration periods (Pyroaurite is also detected, but due to its poor crystallinity and low contents, it is included in the amorphous phase).

The differences in the reactivity of the main BOF slag phases with varying dosages of citrate activators are further reflected in the development of mechanical properties. After 7 days of hydration, the compressive strength of BOF slag pastes increases with the activator dosage. However, already the 28 days-strength values reveal the opposite tendency. After 90 days of hydration, the maximum strength of pastes with both types of the activator is reported when

0.2 M solutions are used, reaching the value of around 90 MPa. The mechanical properties closely reflect the changes in the phase composition shown in Fig. 5.5, emphasizing the impact of belite reactivity.

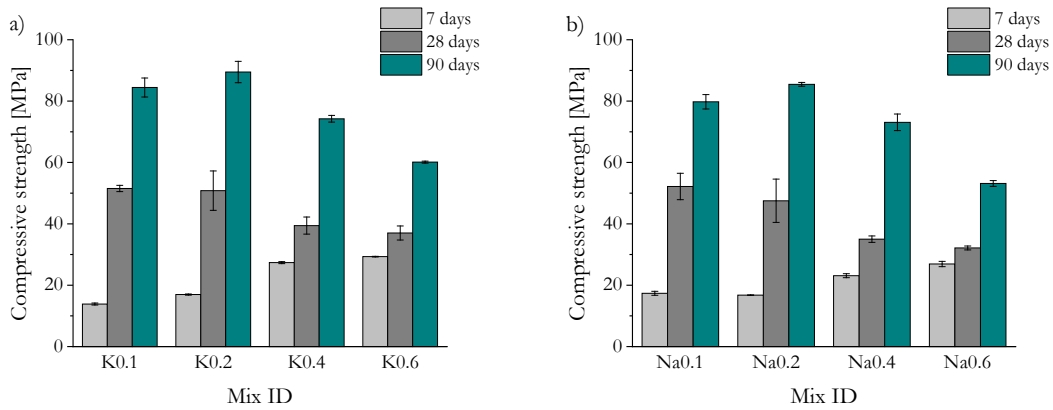


Figure 5.5: Compressive strength of BOF slag pastes with a) potassium citrate and b) sodium citrate.

5.3.2 Environmental impact

In order to take cognisance of physical and chemical factors affecting the leaching of heavy metals from BOF slag/slag-based materials, in this study, two methods: tank test and one batch leaching test, are employed. Additionally, in the one batch leaching test, two fractions of slag and crushed slag pastes, between 0-0.2 mm (P) and 2-4 mm (G), are investigated. The one batch leaching test on the crushed carbonated samples is performed to emphasize the leaching response of the investigated slag mixtures upon accelerated ageing so that the results can be used to estimate the leaching of mortars and concrete, where greater carbonation depth is expected in comparison to pastes. The results are discussed in the following sections.

5.3.2.1 Leaching of heavy metals before carbonation

The fundamental aspects affecting the leaching behaviour from unhydrated and hydrated BOF slag concern the concentration of heavy metals and their distribution within slag phases. Regarding the slag's chemical composition, as shown in Table 5.1, among heavy metals, the highest concentration is reported for vanadium in the investigated slag, followed by traces of chromium, while the scant amounts of molybdenum are below the detection limits of the XRF method. In unreacted slag, vanadium is incorporated in C_2S and brownmillerite, while chromium is detected in wuestite and brownmillerite (see Table 5.2). The incorporation of molybdenum is more difficult to establish due to its low contents in

slag. However, it generally occurs in iron-phases (including brownmillerite, magnetite and wuestite) [180].

Owing to the occurrence of heavy metals in the reactive slag phases, the extent of reaction of these phases becomes crucial. As shown with the early age pore solution analyses, the rate of dissolution of BOF slag phases is strongly affected by the concentration of the activator. With the highly concentrated solutions, considerable amounts of heavy metals are released to the pore solution already within the first hour after being in contact with water. As revealed with quantitative XRD, not only the early kinetics of dissolution of slag phases but also their degree of reaction at later ages show a strong dependency on the activator dosage. Based on the reactivity of the slag phases, the greatest leaching from brownmillerite is expected for the pastes with the highest concentrations of activator and from the C₂S phase with the concentration of 0.1 and 0.2 M potassium/sodium citrate, assuming no incorporation of heavy metals in the hydration products. Nevertheless, the immobilisation of heavy metals in the newly formed hydration products cannot be excluded, as C-S-H gel and hydrogarnets reveal high abilities to incorporate/adsorb these elements.

Vanadium

Among the trace elements in BOF slag, vanadium is often the most abundant and leachable, causing environmental issues [76], [169], [181]. As shown in previous research and confirmed in this study (Fig. 5.6), leaching of vanadium from non-hydrated slag often exceeds the chronic toxicity thresholds [76], [169]. It is generally observed that the release of vanadium is inversely proportional to the concentration of Ca²⁺ in the solution [169]. For non-hydrated BOF slag, the dependency between calcium and vanadium ions may imply that the leaching of vanadium is controlled by the Ca₃(VO₄)₂ solubility limits [169]. However, as shown by De Windt et al. [86], the dissolved concentrations of vanadium are too low to be exclusively governed by this mechanism. From Fig. 5.6, it can be seen that the leaching of vanadium intimately responds to the pH changes, being considerably reduced when pH rises from ~12 to ~13. The difference between the V leaching from the two investigated slag fractions (G and P) can be explained by the higher surface area of the finer fraction (P), which imposes greater reactivity and consequent precipitation of portlandite (pH-buffering phase). Thus, lower values of vanadium leaching are reported for the fine fraction. Similar tendencies are observed for pastes, where coarser fractions show higher leaching of

vanadium, as the pH generated in eluates is lower. The leaching of vanadium from BOF slag pastes falls below the limits specified in Dutch Soil Quality Decree. At high pH, vanadium tends to form oxyanions, which can be adsorbed on C-S-H gel and/or incorporated in hydrogarnet structure [76], [86], [123], [169].

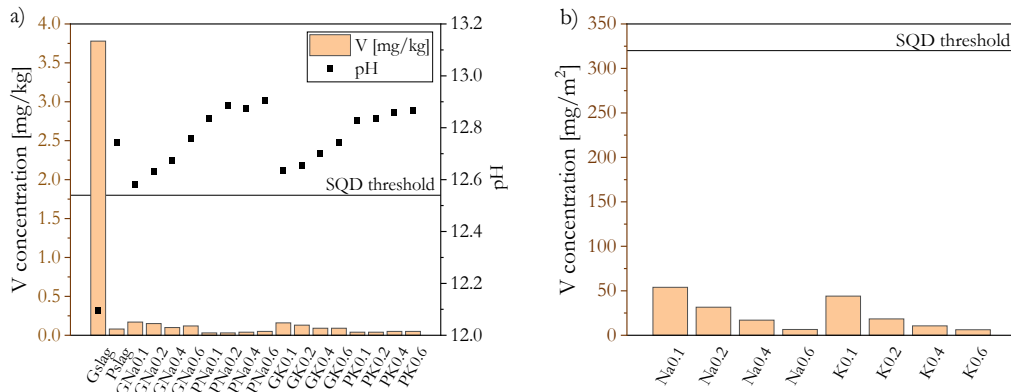


Figure 5.6 Leaching of vanadium before carbonation, derived from a) one batch test, b) tank test (G refers to 2-4 mm size fraction, P to < 0.2 mm).

Chromium

Chromium is the second most abundant and potentially harmful heavy metal in the investigated BOF slag. The leaching of chromium from slag and slag-based pastes is presented in Fig. 5.7. In general, the relatively low release of chromium, not exceeding the threshold values, is observed. Among the analysed samples, the highest leaching of chromium is reported for the unhydrated slag, demonstrating a certain ability of the hydration products to immobilize chromium.

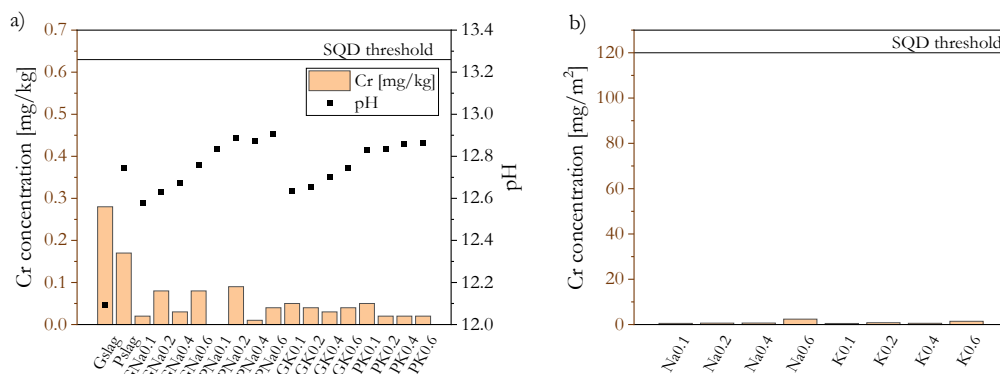


Figure 5.7: Leaching of chromium before carbonation, derived from a) one batch test, b) tank test.

Molybdenum

Even though the total amount of molybdenum in BOF slag is insignificant, the leaching of molybdenum is analysed in this study since brownmillerite (most likely the hosting phase of molybdenum) reveals high reactivity in the presented systems [180]. Fig. 5.8 shows the leaching of molybdenum from unhydrated and hydrated BOF slag. For all samples, the leaching falls far below the SQD limits. Nevertheless, the tendency towards a higher release from the pastes with an increasing concentration of activator can be observed.

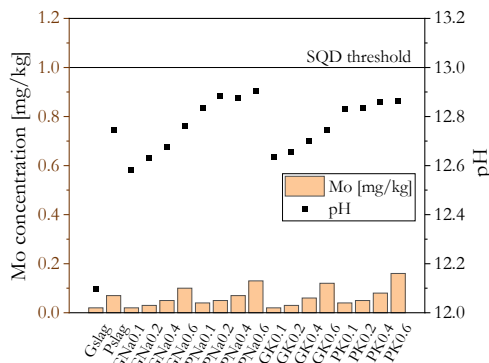


Figure 5.8: Leaching of molybdenum before carbonation, derived from one batch test (the results from the tank test are not shown due to very limited concentrations).

5.3.2.2 Leaching of heavy metals after carbonation

Upon carbonation, the original BOF slag phases, as well as the hydration products, are destabilised, and therefore, the adsorbed/incorporated heavy metals can be released. To reveal the impact of carbonation on the compositional changes in original and hydrated slag, a comparison between the carbonated powders (< 0.2 mm) and non-carbonated samples (unreacted slag and pastes after 90 days of hydration) is made in Fig. 5.9.

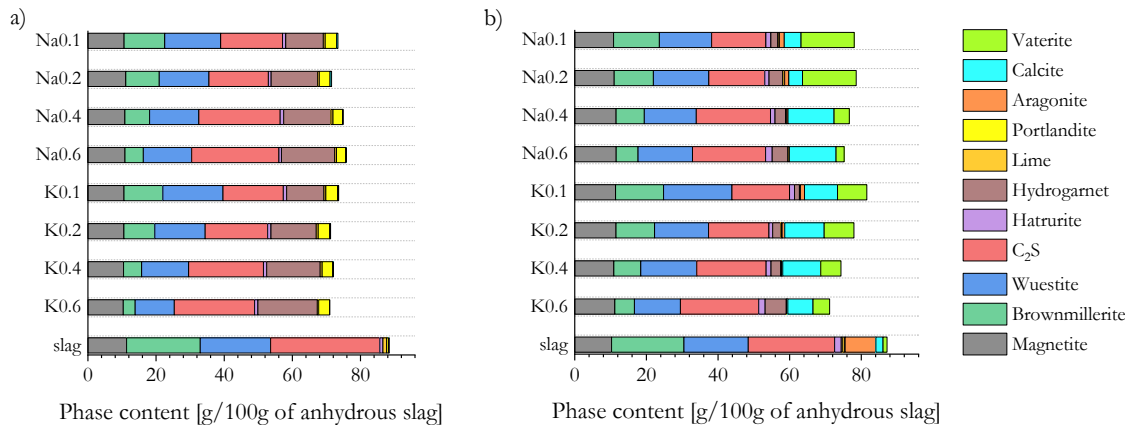


Figure 5.9: Crystalline phase composition of slag/slag pastes a) after 90 days of hydration, b) after 90 days of hydration and subsequent 90 days of carbonation (powder samples < 0.2 mm).

The results demonstrate that in unhydrated BOF slag, C_2S is prone to carbonation (with the reaction degree of about 25%), while other phases are relatively inert. These findings agree well with the reports on post-carbonation leaching from BOF slags presented in the literature [76], [169]. In carbonated BOF slag, aragonite is identified as the main carbonation product.

Similar tendencies are observed for the hydrated slag samples, where C_2S partially undergoes carbonation (up to 15%), while wuestite and brownmillerite remain inert. Among the hydration products, upon carbonation, portlandite is almost entirely consumed and about 75% of hydrogarnet is converted. The exact reaction of hydrogarnet decomposition, however, requires further investigation, as no crystalline Fe-strätlingite or iron hydroxide could be identified with the XRD method. In contrast to the non-hydrated BOF slag, the carbonation of pastes results in the formation of vaterite and calcite. According to Auroy et al. [178], the presence of vaterite is a characteristic for the carbonation of C-S-H gel at accelerated carbonation conditions (3% of CO_2). Since the largest vaterite quantities are observed for the samples activated with 0.1 and 0.2 M citrate solutions, where the highest degree of C_2S reaction is observed, the presence of vaterite likely corresponds to the carbonation of C-S-H gel in the present study. The carbonation of C-S-H gel is confirmed with experiments and thermodynamic modeling in many previous studies [182], [183], [184].

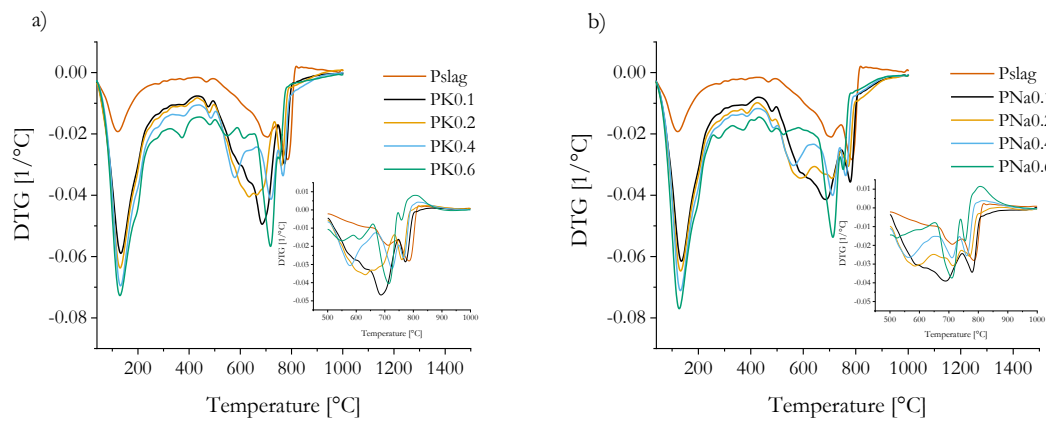


Figure 5.10: DTG curves of carbonated slag/slag pastes analysed on the < 0.2 mm fraction. The inserted graphs show the decomposition of carbonates in the temperature range between 500 and 1000 °C, after correcting for citrate mass loss.

The differences between the carbonates formed in the samples with varying activator dosage are further reflected with thermogravimetric analyses (Fig. 5.10). In order to take into account the mass contribution of citrate, the graphs are corrected by subtracting the mass

loss from the non-carbonated corresponding pastes (Fig. 5.10, insert). In general, in all samples, carbonates decompose in the broad temperature range (between 500 and 800 °C). However, the mass loss is shifted towards lower temperatures for the samples with less concentrated citrate solutions, indicating differences in the physical properties of carbonates formed [185].

The post-carbonation leaching, especially of shaped slag-based materials, is not exclusively a result of the destabilisation of phases but a compilation of several simultaneous effects. For example, the resistance of the material to carbonation must be considered. As shown in Table 5.5, with the phenolphthalein test, no substantial extent of carbonation is detected for all samples. One of the reasons for the limited carbonation depth is the very dense microstructure, i.e. low porosity (see Chapter 3). Only the tendency towards a higher carbonation depth with an increasing activator dosage (up to 1.5 mm for slag activated with 0.6 M solutions) is observed. While for the powder fraction, the amount of carbonates derived from the thermogravimetric method noticeably decreases with the increasing activator dosage (Table 5.5), for the 2-4 mm fraction, the differences in the carbonates content are significantly diminished. This might be associated with the varying carbonation depths in 2-4 mm grains, which tend to increase for samples with more concentrated citrate solutions. Several factors affecting the quantity of carbonates, their physical nature, and carbonation depth can be distinguished.

Table 5.5: The mass losses due to carbonate decomposition determined with thermogravimetry and carbonation depths measured with phenolphthalein test.

Parameter	Slag	K0.1	K0.2	K0.4	K0.6	Na0.1	Na0.2	Na0.4	Na0.6	
Mass loss	< 0.2 mm	3.7	7.8	6.9	5.7	4.2	8.3	7.3	5.5	4.0
500-800 °C [%]	2-4 mm	0.2	5.5	6.0	4.9	3.9	5.9	4.0	5.1	4.0
Carbonation depth [mm]	2-4 mm	0	0.5	0.5	1	1.5	0.5	0.5	1	1.5

On the one hand, taking into account the activator dosage, higher resistance to carbonation could be expected with more concentrated activators, assuming the increased content of Na^+/K^+ in the pore solution, and hence a larger alkalinity buffer [186]. On the other hand, in samples with a lower activator dosage, the degree of C_2S hydration is higher, implying a denser microstructure (further supported by better mechanical performance), which impedes the CO_2 ingress. Furthermore, larger quantities of portlandite in these samples result in the volume increase and formation of a dense protective layer of carbonates on the

surface of the sample upon carbonation [183], [185], [187]. In contrast, during the carbonation of the C-S-H gel, coarsening of the microstructure might occur, especially with a low Ca/Si ratio, facilitating the CO₂ ingress [187], [188]. Phase analyses also demonstrate that hydration products are more prone to carbonation than the original slag phases. This might explain the larger quantities of carbonates in the powdered samples with less concentrated citrate solutions resulting from the reaction of C-S-H gel with CO₂.

Vanadium

After carbonation, the leaching of vanadium increases significantly, exceeding the legal thresholds in the one batch leaching test up to 100 times (Fig. 5.11). In the tank test, however, where the impact of carbonation depth plays a crucial role, the BOF slag pastes meet the leaching standards defined in SQD. The strong correlation between the vanadium leaching and the extent of carbonation is especially visible when comparing the two fractions of slag/pastes. Powder samples show several times higher leaching than the samples with 2-4 mm grain size, implying that the ratio between carbonated and non-carbonated sections defines the magnitude of vanadium leaching. Even though the pH of eluates from the samples with highly concentrated citrate salts is more alkaline, the release of vanadium is boosted in these samples, likely due to the greater carbonation depth and decomposition of hydrogarnets (Fig. 5.9).

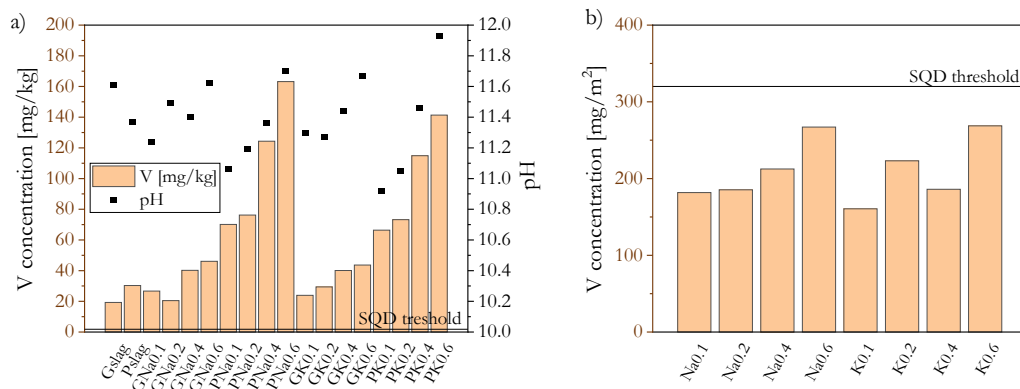


Figure 5.11: Leaching of vanadium after carbonation derived from a) one batch test, b) tank test.

Chromium

The leaching of chromium from plain BOF slag after carbonation is not considerably affected, remaining below the restrictive levels, which agrees with the study by Huijgen and Comans [189]. In contrast, the chromium release from the crushed, carbonated, citrate

activated pastes is significantly increased, especially in pastes with 0.6 M potassium/sodium citrate solutions. This behaviour can be the consequence of the highest reactivity of brownmillerite and partial reactivity of wuestite (which contain Cr) in these samples and destabilization of their hydration products upon carbonation, as revealed with the phase analysis (Fig. 5.9). The presence of citrate complexes with chromium and their decomposition with the pH drop also cannot be excluded. The tank test (Fig. 5.12), however, clearly demonstrates that from the shaped products, where carbonation depth is insubstantial, the leachability of chromium is very limited. The presented data indicate that too high concentrations of citrate activator can result in the boost of chromium leaching, and this phenomenon must be considered when designing BOF slag-based materials in engineering practice.

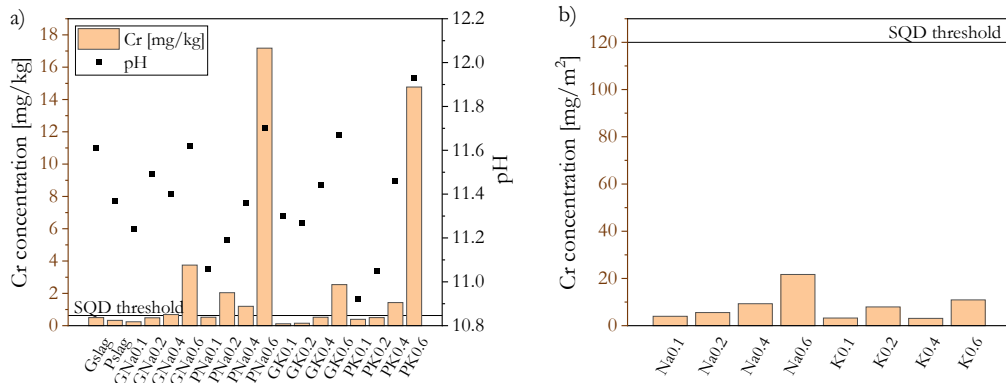


Figure 5.12: Leaching of chromium after carbonation, derived from a) one batch test, b) tank test.

Molybdenum

The leaching of molybdenum from plain BOF slag shows only a slight increase after carbonation (Fig. 5.13). This behaviour contradicts the results of Baciocchi [190], who reported a decreased release of Mo after carbonation. In the study of Costa [167], where two slags with varying composition were analysed, after carbonation, for one slag, Mo leaching was reduced and for another slag, it increased. In one batch leaching test, the release of molybdenum from the carbonated samples escalates, exceeding the threshold values for samples with the highest activator dosages. As shown with the phase analyses of carbonated and non-carbonated materials (Fig. 5.9), brownmillerite (Mo hosting phase) is much more stable upon carbonation than its hydration products. In consequence, the highest leaching of molybdenum is observed for the samples with the greatest extent of brownmillerite hydration. Nevertheless, even though after carbonation, molybdenum becomes very mobile

in the carbonated areas, considering its content in slag and carbonation resistance of pastes, the leaching of molybdenum is not a restraining factor for the application of slag products, as confirmed with the tank test.

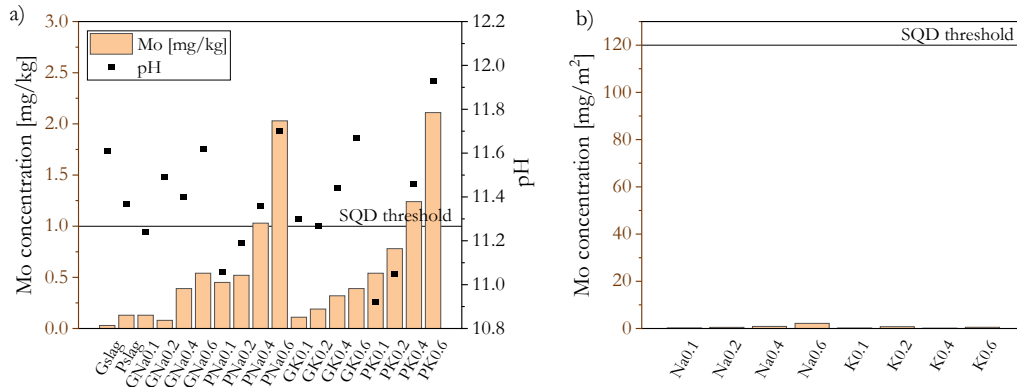


Figure 5.13: Leaching of molybdenum after carbonation, derived from a) one batch test, b) tank test.

5.4 Conclusions

Chemically activated BOF slag pastes are the newly-designed potential building products. To assess the risk of environmental harmfulness of these materials during their service life, in this chapter, the leaching of heavy metals upon carbonation is investigated. Potassium and sodium citrate salts are used with variable dosages to activate slag with the aim to provide a comprehensive overview of the impact of the hydration degree of BOF slag phases on the leaching behaviour of pastes. The carbonation resistance of BOF slag/ slag pastes and the compositional changes induced by carbonation are assessed. To examine the effects of physical and chemical changes, which occur simultaneously upon carbonation, the leaching of heavy metals is determined with the tank test and one batch leaching test on shaped and unshaped materials (fractions < 0.2 mm and 2-4 mm), respectively. The following conclusions are reached within this study:

- The hydration kinetics of BOF slag phases can be controlled and optimized with the addition of potassium/sodium citrate. Whereas the type of activator has a minor impact on the hydration kinetics and phase development, the dosage of the activator is pivotal. At the early hydration ages, the reactivity of BOF slag phases, especially of brownmillerite, is accelerated by the highly concentrated solutions. Siliceous hydrogarnets and C-S-H gel are formed. However, the high concentrations of

activators adversely affect the long-term strength development of BOF slag pastes due to the suppressed reaction of C_2S .

- Even though reactions of most contaminated phases take place, the leaching of heavy metals (including vanadium, chromium and molybdenum) from hydrated BOF slag is insubstantial. The release of vanadium (the most abundant heavy metal) from non-carbonated pastes closely corresponds to the pH changes, being significantly diminished at pH close to 13.
- After 90 days of sealed curing, BOF slag pastes reveal high resistance to carbonation. In consequence, the release of heavy metals in the tank leaching test, where the leachability is mostly determined by the carbonation depth, does not exceed the legal thresholds specified in Soil Quality Decree. In one batch leaching test, the general tendency towards intensified heavy metal leaching from the pastes with highly concentrated citrate solutions is observed. This can be associated with the greatest degree of brownmillerite hydration in these samples and the decomposition of its reaction product- hydrogarnet, which potentially hosts heavy metals in the hydrated slag. As the immobilisation capability of BOF slag hydrates drastically drops upon carbonation, the carbonation resistance (depth of carbonation) becomes crucial in preventing the release of heavy metals from BOF slag-based products. This study demonstrates that the resistance to carbonation can be improved by facilitating the hydration of C_2S in the BOF slag with the use of low concentrations of citrate salts (e.g., 0.1 M and 0.2 M in this study).

NO_x degradation by photocatalytic mortars: The underlying role of the CH and C-S-H carbonation

This chapter aims to understand the impact of the carbonation mechanism of C-S-H and CH in photocatalytic mortars on NO_x removal efficiency. Changes in surface chemistry and microstructure induced by the carbonation of portlandite and C-S-H (AFm/AFt) were correlated with the photocatalytic efficiency of the mortars doped with three types of titania-based photocatalysts. Furthermore, the influence of cementitious matrix on the photocatalytic selectivity was evaluated by studying the capacity of hydration/carbonation products to adsorb NO₂. The study revealed that in terms of both photocatalytic efficiency and selectivity, mortars with microsilica addition exhibit superior properties over the pure cement-based mortars upon carbonation. Carbonation of C-S-H (AFm/AFt) gel results in the formation of capillary pores in 10-50 nm, which outbalances the shielding effects of carbonates formed, leading to the enhanced photocatalytic properties. Moreover, C-S-H gel maintains its high NO₂ adsorption capacity even after carbonation, resulting in the high selectivity of photocatalysis.

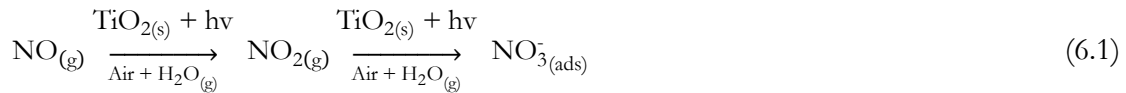
6.1 Introduction

Concrete is the most produced man-made material worldwide, and the consequent large concrete surfaces exposed to solar irradiation provide an excellent opportunity for applying photocatalytic oxidation (PCO) technology for air purification purposes, especially in highly polluted urban areas. Incorporation of photocatalytic semiconductors into a concrete surface layer or as a surface coating induces photocatalytic oxidation of air pollutants and in the meantime, provides self-cleaning effects to the concrete [20], [191]. Among available

Reproduced from:

Kaja, A. M., Brouwers, H. J. H., & Yu, Q. L. (2019). NO_x degradation by photocatalytic mortars: The underlying role of the CH and C-S-H carbonation. Cement and Concrete Research, 125, 105805.

semiconductors, TiO₂-based photocatalysts are most commonly used and investigated due to their high photocatalytic efficiency, high stability and low price [192]. Since nitrogen oxides (NO_x) (the generic term for a group of highly reactive gases, including nitric oxide (NO) and nitrogen dioxide (NO₂)), cause great concern for health and the environment, in recent years, photocatalytically active materials for NO_x removal have been extensively investigated [21], [193], [194]. The photocatalytic conversion of NO with the use of TiO₂ photocatalyst can be described in a simplified way with the following reaction [195]:



The pollutants degradation efficiency of photocatalytic concrete depends on the mix design and the production approach. The main parameters affecting the photocatalytic performance of concrete are the type of binder used (pH, phase composition), porosity, microstructure, surface roughness, the colour of concrete, and type and dosage of photocatalyst [194], [196], [197], [198].

The photocatalytic oxidation of pollutants is a superficial reaction taking place on the concrete surface that is exposed to atmospheric conditions. Therefore, durability issues are of high significance. Among various durability aspects, carbonation is one of the most important ageing-related factors. Upon carbonation, the phase composition of concrete is altered and so the pH, specific surface area and porosity are also affected. Moreover, the overall titania content in the total volume of solids is reduced since the absorbed CO₂ reacts with the hydration products to form calcium carbonates. However, up till now, the understanding of the carbonation effects on photocatalysis is very limited. A few previous studies implied that carbonation of photocatalytic concrete causes the reduction of photocatalytic efficiency, possibly due to the shielding effects of carbonation products on titania particles and the reduction of porosity [199], [200]. However, these assumptions can only be valid when Portland cement carbonation is considered. As widely described in the literature, the impact of carbonation on the concrete microstructure does not necessarily result in a porosity decrease e.g., when pozzolanic materials are added [184], [183], [201]. Moreover, it is not clear whether the changes in porosity or shielding effects are the governing factors causing the reduction of the photocatalytic performance. Even more importantly, with the addition of pozzolanic materials, it is unknown whether the decrease

of photocatalytic performance upon carbonation is actually observed. Up to now, no systematic study has been performed on this topic.

The microstructural changes in concrete upon carbonation depend on the CO₂ binding capacity and phase composition of concrete, with a particular impact of the quantity of portlandite. The reaction of CO₂ with portlandite leads to the formation of CaCO₃ and consequent structural densification. With the addition of pozzolanic material, the CO₂ binding capacity of concrete is reduced due to the lower overall CaO/SiO₂ ratio, and portlandite is consumed to form additional C-S-H gel. Thermodynamic modeling predicts that carbonation of C-S-H gel takes place after the carbonation of CH [184], [202], whereas the experimental data shows that carbonation of C-S-H and CH occurs simultaneously [172], [183], [203]. The carbonation mechanism of the C-S-H gel differs from the carbonation of CH, being governed by the decalcification of the C-S-H layers and formation of amorphous silica [173]. In consequence, the reduction of the volume of the solid (known as carbonation /decalcification shrinkage) and coarsening of the pores is often accompanied by an increase of the total concrete porosity upon carbonation of C-S-H gel. Morandea et al. [182] showed that when a part of cement is substituted with class F fly ash, the formation of big capillary pores (>50 nm) occurs during carbonation. Similarly, Shi et al. [184] reported an increased volume of pores in the range between 10-100 nm for metakaolin and metakaolin/ limestone mortars. It is worth mentioning that also for Portland cement mortars, even if the total amount of pores is reduced, coarsening of the pores is observed upon carbonation [183].

Considering the impact of carbonation-induced microstructural changes on the photocatalytic performance of concrete, it needs to be kept in mind that whereas porosity has a significant influence on the efficiency of the pollutants oxidation process, a higher porosity of concrete does not necessarily result in better photocatalytic properties [204], [205]. Moreover, the strong presence of nanopores (< 50 nm) is found to negatively affect the photocatalytic properties [196], [204]. Jimenez-Relinque et al. [196] suggested an optimum pore size range between 50 and 500 nm for the NO_x and between 100 and 500 nm for the degradation of the organic dye by investigating 28 days hydrated mortars. However, it needs to be noticed that the inner porosity of mortars does not reflect the real surface porosity, where carbonation is unavoidable. Therefore, the re-evaluation of the impact of surface properties of mortars, affected by the mortars' capacity to bind CO₂ and the carbonation mechanism, on the photocatalytic properties is required. Owing to the

porosity increase when C-S-H gel carbonates and porosity decrease when portlandite carbonates, it is hypothesized that from the microstructural point of view, photocatalytic properties can be optimized by controlling the changes in the pore structure of a concrete surface upon carbonation, which are directly related to the initial mix design.

Another important aspect is the carbonation impact on the selectivity of the photocatalytic process. Even if optimal properties of concrete for photocatalytic oxidation are provided, the total outcome of air purification can still be very limited or even take a negative value [206]. This can be attributed to the insufficient conversion of air pollutants to final products, e.g., nitric oxide (NO) to nitrates or volatile organic pollutants to CO₂ and H₂O. During the photocatalytic oxidation of NO, firstly, NO₂ is formed, which is then oxidized to nitrates (NO₃⁻). Instead of being further photocatalytically oxidized, part of the produced NO₂ can be potentially released into the atmosphere. Since the toxicity of NO₂ is significantly higher than NO [207], the ability of photocatalytic mortars for selective oxidation is an important feature. However, only limited research can be found on this topic. Previous studies were mainly focused on the improvement of the photocatalytic reaction selectivity through the modification of the photocatalyst itself, which in turn often results in the reduction of the NO conversion [206], [208]. At the same time, higher values of selectivity are observed when the photocatalyst is loaded into the cementitious matrix in comparison to pure photocatalysts [209]. Nevertheless, the understanding of this behavior remains limited and the effects of carbonation on the selectivity have never been thoroughly investigated.

The photocatalytic oxidation of NO₂ is only one of the possible routes for NO₂ elimination. For example, Araña et al. [195] recently revealed that NO₂ abatement by a photocatalyst is not necessarily an effect of photocatalytic oxidation but rather of the adsorption of NO₂ on the photocatalyst surface, which later undergoes a disproportionation reaction as a prevalent mechanism for NO₂ elimination. Moreover, a few studies already indicated that the chemical composition of the hosting matrix, where the photocatalyst is incorporated, affects the NO₂ abatement [210], [211]. Thus, providing a surface with a high NO₂ adsorption capacity could be a potential solution for selectivity improvement. Taking into account the high NO₂ adsorption capacity of portlandite and C-S-H gel [212], [213], the cementitious matrix seems to be an excellent substrate for photocatalytic processes. Nonetheless, the carbonation impact needs to be further evaluated since the ability of calcium carbonates to adsorb NO₂ is substantially lower than that of portlandite and C-S-H gel [214]. Furthermore, it is

especially important to combine the effects of the formation of carbonates with lower NO₂ adsorption capacity with the accompanying structural changes in order to reveal the real impact of carbonation on the selectivity.

This study aims to explore the underlying role of the carbonation mechanisms on the photocatalytic degradation of NO_x by cement mortars. The carbonation-induced physicochemical changes are analyzed and compared for two mortars series, the first one rich- and the second one free of portlandite. Portland white cement is employed as the primary binder in both mortar series and pozzolanic microsilica is applied in the second mix to adjust the portlandite content. This strategy is used in order to differentiate between the impact of carbonation of CH and C-S-H phase on the photocatalytic performance, and in consequence, to propose a mix design optimization method in order to retain the photocatalytic efficiency during the service life of photocatalytic mortars. For a deeper understanding of the impact of the surface chemistry and microstructure on the selectivity of the photocatalytic processes, the capacity of un-carbonated and carbonated mortars to adsorb toxic NO₂ in darkness is analyzed in this study.

6.2 Experimental

6.2.1 Materials

CEM I 42.5 LA white cement (Aalborgportland), microsilica (Elkem 920ED) and standard sand were used in this study as raw materials. In order to provide representative results, which are valid for different types of photocatalysts, three photocatalysts were selected and investigated, including commercially available Aeroxide TiO₂ P25 (Evonik Industries) consisting of 80% of anatase and 20% of rutile (specific surface area (SSA) ~ 50 m²/g), KRONOcLean 7000 carbon-doped titania (SSA ~ 251 m²/g) (Kronos International), and one home-synthesized composite photocatalyst consisting of 85% of SiO₂ and 15% of TiO₂ (SSA ~ 200 m²/g) prepared with a sol-gel method (more detailed synthesis information is presented elsewhere [215]). The P25 and KRONOcLean 7000 (Kronos) TiO₂ were used as reference photocatalysts, the first one being photocatalytically active only under UV irradiation and the second one with the photo-response extended to the visible regions. To the homemade composite, the coating of titania over silica nanoparticles was applied with the aim to increase the specific surface area of the photocatalyst and, in the meantime, to improve its mechanical properties and thermal stability [216]. Furthermore, the

photocatalytic activity of silica-titania composite over pure titania could be enhanced due to: i) the ability of silica for long-term adsorption of the pollutant molecules, ii) high redox potential of the electrons and holes, iii) additional scattering of the light to the titania surface [217]. The efficiency of the applied coating method was examined by the FTIR measurement (Fig. 6.1). The band located at 946 [cm⁻¹] corresponds to the vibration of Si-O-Ti, confirming the formation of the inorganic network between SiO₂ and TiO₂ [218], [219], [220].

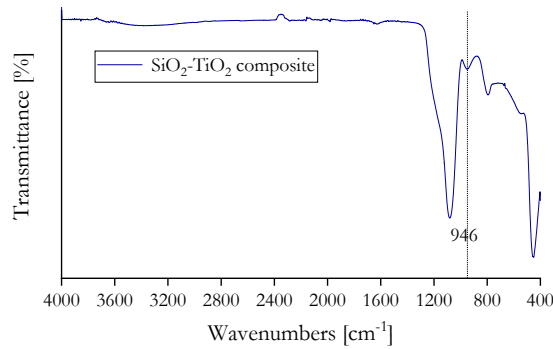


Figure 6.1: FTIR spectrum of titania-silica composite.

6.2.2 Mix design and sample preparation

Mix design

Table 6.1: Mix design of the photocatalytic mortars.

		Cement [g]	Microsilica [g]	Sand [g]	TiO ₂ P25 [g]	KRONO- clean [g]	TiO ₂ - SiO ₂ [g]	SP w/b dosage [wt%]
White cement	P25	450	-	1350	22.5		0.5	0.4
	Kronos	450	-	1350		22.5	0.5	0.4
	SiO ₂ -TiO ₂	450	-	1350			22.5	0.5
White cement + microsilica	P25	270	180	1350	22.5		0.5	1.2
	Kronos	270	180	1350		22.5	0.5	1.2
	SiO ₂ -TiO ₂	270	180	1350			22.5	0.5

Two series of standard mortars with the water to binder ratio (w/b) of 0.5 were prepared and tested in this study. The first series consisted of white cement-based mortars, while in the second series, 40 wt% of cement was replaced with microsilica. For each composition, three photocatalysts were investigated, keeping the amount of photocatalyst at a constant level of 5 wt% of the binder. Superplasticizer MasterGlenium® 51 was used to adjust the

consistency of the mixtures (the dosage is shown in Table 6.1 and is expressed in wt% by mass of the binder). The mix design of the mortars is described in Table 6.1.

Mortars manufacture

Cement and microsilica were firstly intermilled in a planetary ball mill (Pulverisette 5, Fritsch). Milling was employed in this study in order to ensure a proper homogeneity of the binder, which nevertheless would unavoidably cause slight alteration of the specific surface area of cement and microsilica. Subsequently, the photocatalysts were dispersed in 200 ml of water with an ultrasonic device (Hielscher UP400S) for 10 min (amplitude of 75%). An ice-water bath was used to prevent heating of the solutions. Before mixing with cement (cement and microsilica) and sand, the temperature of the solutions was controlled and kept constant at 21 ± 1 °C. Mixing of the mortars was performed in accordance with the EN 196-1:2005 standard. The amounts of superplasticizer were adjusted to provide similar workability of the mortars, falling in S4 class according to the EN 206-1 standard. The mortars were cast into $100 \times 200 \times 20$ mm³ molds, vibrated for 1 min and covered with plastic sheets to prevent moisture loss and carbonation. After 24 hours, all mortars were demolded, sealed with self-adhesive aluminum foil, placed in a humidity chamber (RH > 95%, 20 °C) and cured for 5 months to ensure sufficient hydration. At the end of the curing period, the samples were cut in half with a saw to create plates with a thickness of about 1 cm. This procedure was applied in order to provide surfaces with the same roughness, to eliminate wall effects and to avoid the eventual early age carbonation during casting and demolding of the samples. As water treatment during the cutting could not be avoided, and the photocatalytic efficiency is strongly influenced by the moisture level, after cutting, the samples were immediately inserted and dried in a nitrogen chamber to limit carbonation.

6.2.3 Methods

SEM analyses were performed according to the procedure described in Section 2.2.2. For the mercury intrusion porosimetry (MIP) and thermogravimetric measurements, 3 mm thick surface plates were cut from un-carbonated and carbonated mortars. The plates were split with tongs into cubic pieces for SEM measurements and powdered in a planetary ball mill (Pulverisette 5, Fritsch) for thermogravimetric analyses. A detailed description of both methods is provided in Section 3.2.2.

Accelerated carbonation and Phenolphthalein test

The 5 months old mortars were exposed to CO₂ atmosphere for 28 days in a carbonation chamber. The conditions of 3% CO₂ and RH = 65% were selected in order to facilitate the formation of carbonates, preserve the nanostructure of C-S-H and at the same time mimic the natural carbonation process [172], [178]. Phenolphthalein testing was used to determine the carbonation depth in the samples at the end of the carbonation period. The mortar plates were split with a saw and the carbonation profiles were obtained by spraying the cross-sections with a 1 wt% phenolphthalein aqueous solution.

Photocatalytic efficiency assessment

The photocatalytic oxidation experiments were carried out in accordance with the ISO 22197-1:2016 standard, using a plug-flow setup (Fig. 6.2). Nitric oxide (NO) was employed as a model pollutant. The mortars were tested before and after accelerated carbonation.

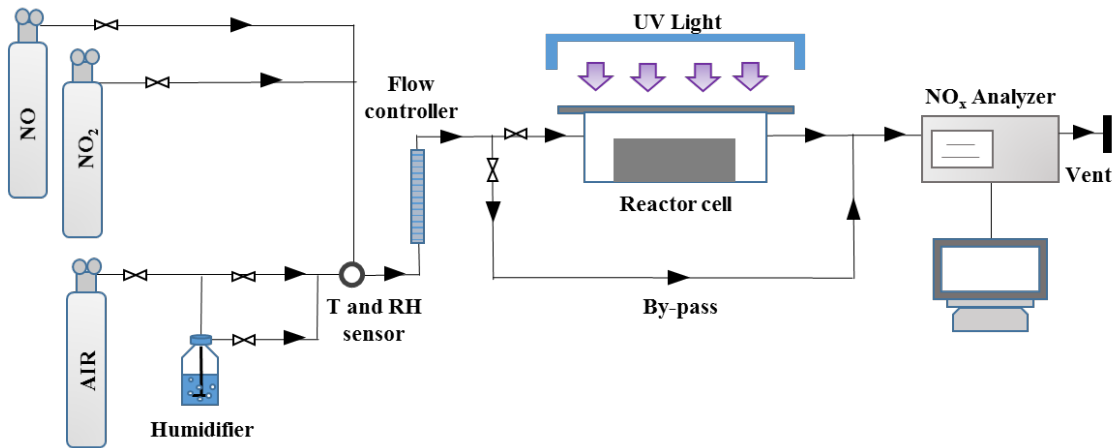


Figure 6.2: The scheme of the PCO experimental set-up.

The mortars were firstly assembled in the reactor and the position of the samples was adjusted to create a 3 mm gap between the sample surface and the top of the reactor. The reactor was covered in order to prevent the uncontrolled degradation of pollutants while adjusting the measurement parameters. All the measurements were performed under stable conditions, described in Table 6.2.

The desired concentration of NO pollutant was achieved by mixing the NO with the synthetic air. Firstly, the gas was allowed to flow through a by-pass until the stabilized values of the light radiation, NO concentration and humidity were reached. Afterward, the gas flow

was switched from the by-pass to the reactor and the data acquisition was started. During the first 15 minutes of the measurements, the reactor was kept covered in order to ensure stable conditions. When a steady-state condition was reached, the samples were illuminated through the glass plate for 1 hour. An APNA-370 (Horiba) analyzer was used to monitor the concentration of pollutants.

Table 6.2: PCO experimental conditions (at ambient pressure).

Parameter	Value	Unit
Relative humidity	50	%
Initial NO concentration	1	ppm
Volumetric flow rate	3	L/min
Light intensity (UVA)	10	[W/m ²]
Temperature	20	°C

The conversion of NO (to nitrate and NO₂) was calculated according to the formula 6.2. Taking into account the eventual NO₂ release, the photocatalytic conversion (efficiency) of the designed materials was also characterized by the NO_x (NO + NO₂) conversion to nitrate and calculated according to the formula (6.3).

$$\% \text{ Conversion} = \frac{[c_{\text{NO}}]_{\text{in}} - [c_{\text{NO}}]_{\text{out}}}{[c_{\text{NO}}]_{\text{in}}} \cdot 100\% \quad (6.2)$$

$$\% \text{ Conversion} = \frac{[c_{\text{NO}_x}]_{\text{in}} - [c_{\text{NO}_x}]_{\text{out}}}{[c_{\text{NO}_x}]_{\text{in}}} \cdot 100\% \quad (6.3)$$

Where $[c_{\text{NO}_{(x)}}]_{\text{in}}$ is the average initial concentration [ppm] of the first 5 min before turning on the light; $[c_{\text{NO}_{(x)}}]_{\text{out}}$ is the average outlet concentration [ppm] of the last 5 min of the irradiation period.

The selectivity of photocatalytic reaction towards the formation of nitrates S(%) [206], [211] was calculated with the following formula (6.4).

$$S\% = \frac{[c_{\text{NO}_x}]_{\text{in}} - [c_{\text{NO}_x}]_{\text{out}}}{[c_{\text{NO}}]_{\text{in}} - [c_{\text{NO}}]_{\text{out}}} \cdot 100\% \quad (6.4)$$

In order to evaluate how the selectivity of NO to nitrates is influenced by the cementitious matrix, adsorption of NO₂ on the surface of the mortar was also measured with the PCO setup. Tests were performed in darkness by flowing a mixture of synthetic gas and 0.5 ppm

of NO₂ through the reactor. The measurement time, humidity, and gas flow were kept identical as for the PCO measurement.

6.3 Results analysis

6.3.1 Mortars characterization

EDX mapping analysis

In a highly alkaline cement environment, titania nanoparticles tend to agglomerate [221], while providing a homogenous dispersion of photocatalyst in the cementitious matrix is crucial 1) to ensure a highly effective surface area of the photocatalyst for the air purifying reactions to occur and 2) to eliminate the statistical error of the measurements of photocatalytic oxidation caused by the local agglomeration of titania particles. This was therefore addressed in this study by applying the ultrasonic treatment (see Section 6.2.2). The dispersibility of the photocatalysts in cement mortars was examined with EDX mapping analysis. It can be seen from Fig. 6.3 that a satisfactory dispersion of titania was achieved. The homemade silica-titania photocatalyst was characterized by a larger size variability compared to P25 (Fig. 6.3b vs. Fig. 6.3a), which was caused by agglomerates with a size up to ~10 μm formed during the manufacture of the composite. Nevertheless, the overall distribution of the composite in the mortars was homogenous. The homogenous dispersion of the different types of photocatalysts contributed to the maximization of their potential in terms of air pollutant removal efficiency.

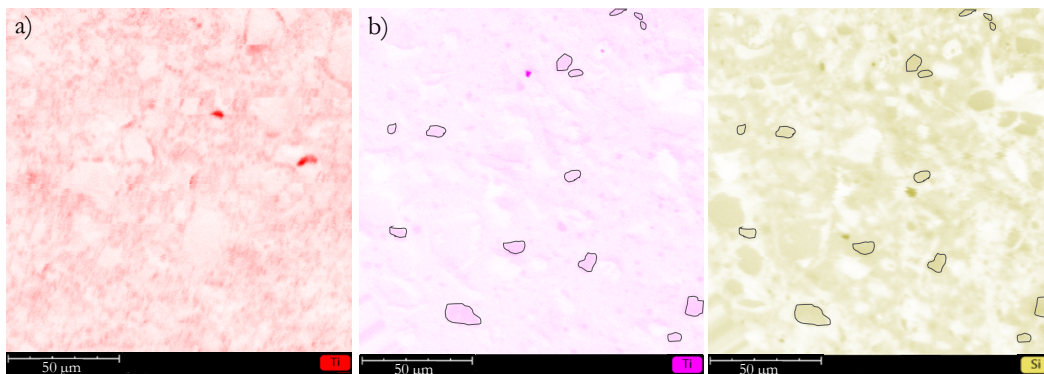


Figure 6.3: EDX mapping showing the distribution of a) titanium in the cement mortar with the P25 addition and b) titanium (in pink) and silicon (in gold) in the cement mortar with the silica-titania composite addition (the outlined grains represent silica-titania agglomerates formed during the manufacture of photocatalyst).

Thermogravimetric analysis & Phenolphthalein test

Fig. 6.4 shows the differential thermogravimetric (DTG) profiles of the mortars before and after the accelerated carbonation treatment. The thermogravimetric (TG) data were collected from the powdered 3 mm upper layers of mortar plates. After 5 months of hydration, two main mass losses were observed in pure cement-based samples due to the release of water from C-S-H (AFt/AFm) phases (30-300 °C) and portlandite (400-450 °C), whereas no portlandite was observed in the mortars with microsilica addition. The successful elimination of portlandite in mortars with microsilica enables differentiation between carbonation of C-S-H (AFt/AFm)/ CH (white cement mortars) and C-S-H (AFt/AFm) (white cement + microsilica mortars) in this study.

After 28 days' treatment in the carbonation chamber (3% CO₂), samples revealed an additional mass loss in the temperature range between 600-800 °C for the pure cement-based mortars and a broad peak between 300-700 °C for the mortars with microsilica addition. These two new peaks are assigned to the decomposition of calcium carbonates. It is evident that the carbonation products of C-S-H gel and AFt/AFm decompose at significantly lower temperatures than the carbonates in CH abundant mortars. Decomposition of carbonates at lower temperature ranges in mortars with the addition of pozzolanic material has been reported in previous studies [184], [183], and this is attributed to the formation of amorphous/poorly crystalline carbonates [222], [223]. It should be mentioned that whereas portlandite carbonates mostly to calcite [178], carbonation of C-S-H gel also leads to the formation of vaterite [178], [224], which decomposes at lower temperatures than calcite even in the crystalline form [225]. Sevelsted et al. [173] showed with ¹³C{¹H} CP/MAS NMR that in a hydrous environment, the formation of calcium carbonate hydrates can also take place. Thermal decomposition of these compounds occurs between 400 and 500 °C [226].

Different mechanisms of carbonation in mortars rich and lean of portlandite led to substantial differences in the extent of carbonation. A comparison between the phenolphthalein profiles of carbonated samples and the amounts of carbonates formed in both systems clearly indicates that pure cement mortars are more resistant to carbonation than mortars with microsilica addition. The pure cement mortars still possess high basicity throughout, while the mortars with microsilica lost all basicity up to a depth of 3 mm (Fig. 6.4). In the cement mortars, crystalline carbonates are formed, whereas in mortars with the

pozzolanic material, a predominance of amorphous/poorly crystalline carbonates is observed.

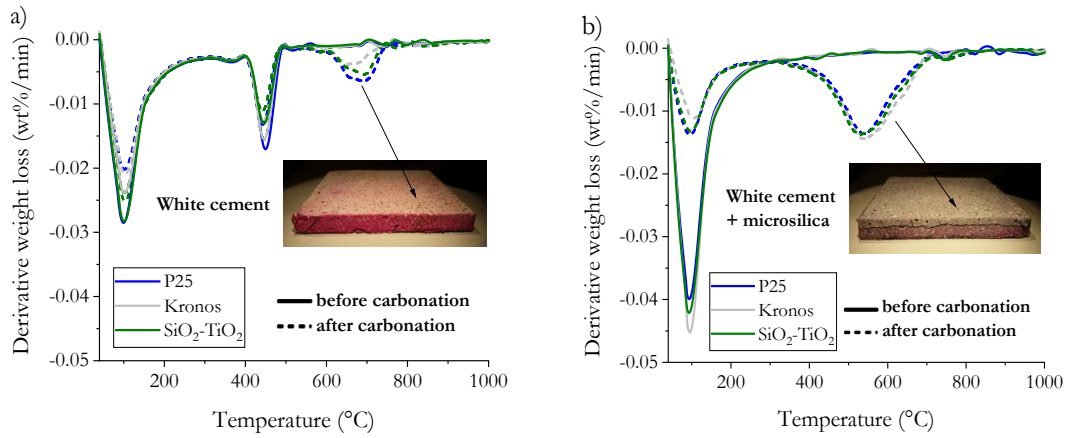


Figure 6.4: DTG curves of carbonated (dash line) and non-carbonated (solid line) a) white cement, b) white cement + microsilica mortars. The carbonation depths measured with phenolphthalein test are representatively visualized regardless of the type of titania used.

Porosity and pore size distribution

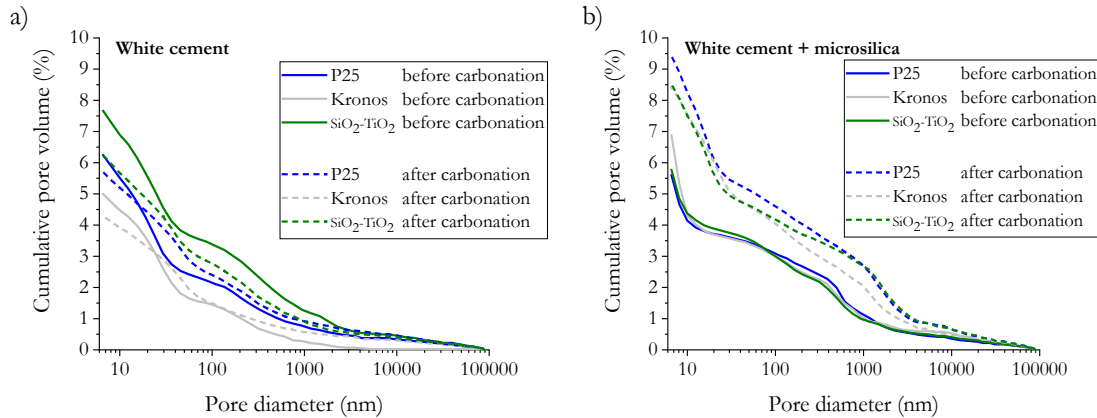


Figure 6.5: Cumulative pore volume derived from Mercury Intrusion Porosimetry of a) white cement mortars and b) white cement + microsilica mortars, before and after accelerated carbonation.

The microstructure of the mortar's surface layer (3 mm), which was altered by the carbonation, was investigated via Mercury Intrusion Porosimetry. The cumulative porosity results (Fig. 6.5) revealed that the carbonation of portlandite and C-S-H led to a decrease in the total porosity of the pure cement mortar's surface, whereas an increase in the total porosity was observed in the mortars with microsilica addition. These findings are in agreement with the observations made in the previous studies on the carbonation of mortars with SCMs [184], [227], and it is worth noting that the addition of photocatalysts did not alter the pore structure evolution beyond carbonation. In the pure cement-based mortars,

changes in the total porosity were substantially lower than that in microsilica mortars, which correlates well with the lower carbonation extent in cement mortars as described with DTG and phenolphthalein test data. Changes in the total porosity between the samples with different photocatalysts can be explained by slight differences in mortars' consistency.

The changes in the pore size distribution for both mortar series during the carbonation are presented in Fig. 6.6. For pure cement-based mortars, a clear decrease of the number of capillary pores between the 10 and 50 nm, accompanied by slight coarsening of the pores, was observed upon the carbonation process. Mortars with microsilica addition initially contained higher amounts of pores below 10 nm after carbonation. However, the number of capillary pores between 10 and 50 nm drastically increased. Coarsening of the pores during the carbonation of mortars with SCMs was also reported elsewhere [181], [185], [183], and can be explained by the so-called “decalcification shrinkage.” Decalcification shrinkage is particularly visible for C-S-H gels with Ca/Si ratios below 1.2, as reported in the study of Chen et al. [228] where, similar to our system, a paste containing 70% of white cement and 30% of microsilica was investigated. The appearance of bigger pores of $\sim 1 \mu\text{m}$ in microsilica mortars can be attributed to the formation of cracks during the carbonation of the C-S-H gel. Formation of cracks upon C-S-H gel carbonation is found to occur in both accelerated and natural conditions [178].

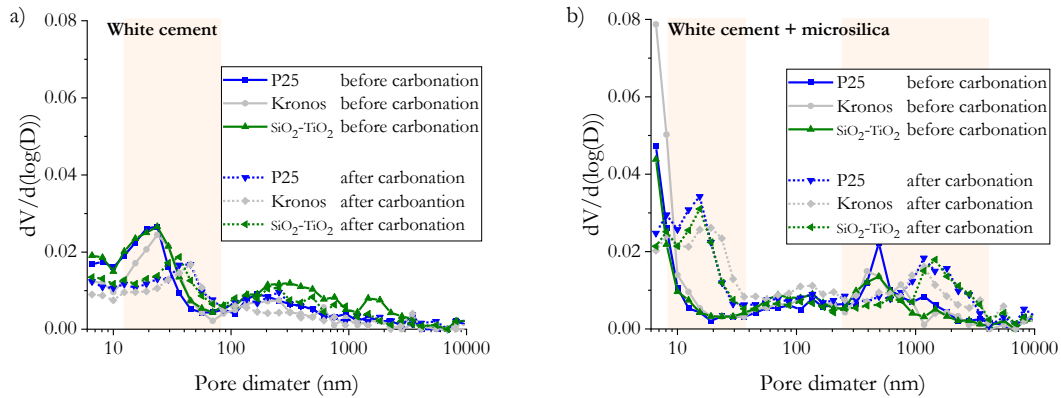


Figure 6.6: Differential pore size distribution in a) white cement mortars and b) white cement + microsilica mortars before and after carbonation.

SEM analysis

The microscopic observations of the surface of the mortar after accelerated carbonation treatment (Fig. 6.7) showed that the carbonation of white cement hydration products led to

the formation of a dense layer of carbonate crystals, strongly affecting the effective exposure of photocatalyst (Fig. 6.7a). In contrast, in mortars with microsilica addition (Fig. 6.7b), only a limited formation of crystalline carbonates was observed and the gel-like structure of the C-S-H phase was preserved. Additionally, in agreement with the porosity results, the formation of cracks was observed in microsilica mortars.

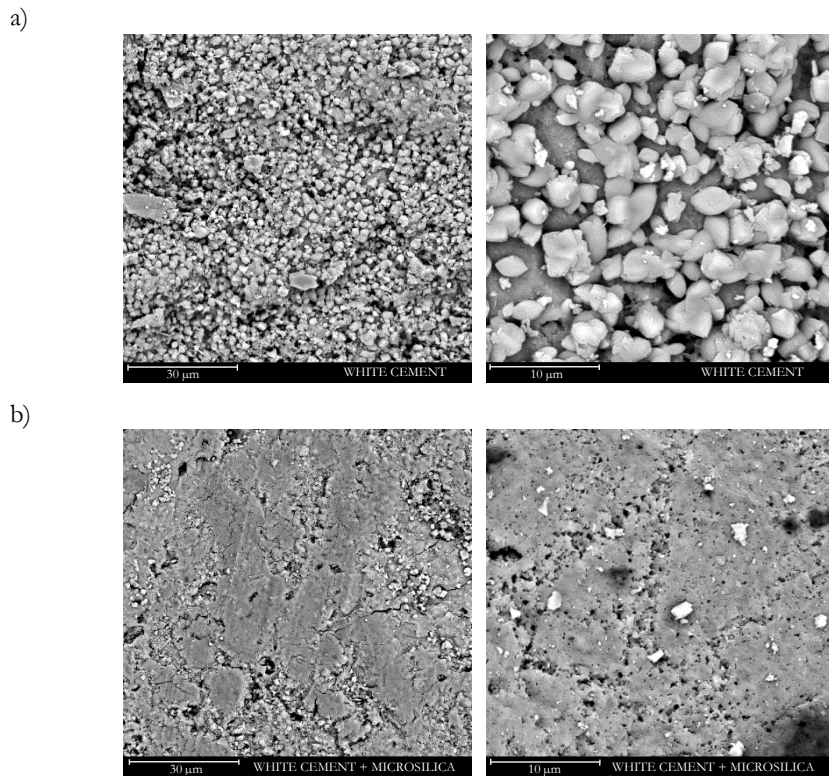


Figure 6.7: SEM images of a) pure cement mortar's surface and b) microsilica mortar's surface after carbonation.

6.3.2 Photocatalytic efficiency

NO_x oxidation rate

The efficiency (conversion %) of photocatalytic oxidation of NO and NO_x before and after carbonation is presented in Fig. 6.8. Comparison of the results obtained for pure cement-based mortar and microsilica mortars clearly reveals that both photocatalyst type and matrix composition/microstructure strongly influence the photocatalytic performance. In regard to the photocatalytic oxidation rate, in un-carbonated white cement mortars, the best performance was observed for P25, followed by the SiO₂-TiO₂ composite and Kronos. Furthermore, the photocatalytic efficiency of the mortars with SiO₂-TiO₂ composite was the most sensitive to the surface changes upon carbonation. As SiO₂-TiO₂ composite formed

agglomerates (as shown with EDX mapping, see Section 6.3.1), it is apparent that due to the microstructural changes, there was a limited exposure of SiO₂-TiO₂ composite for the photocatalytic reaction.

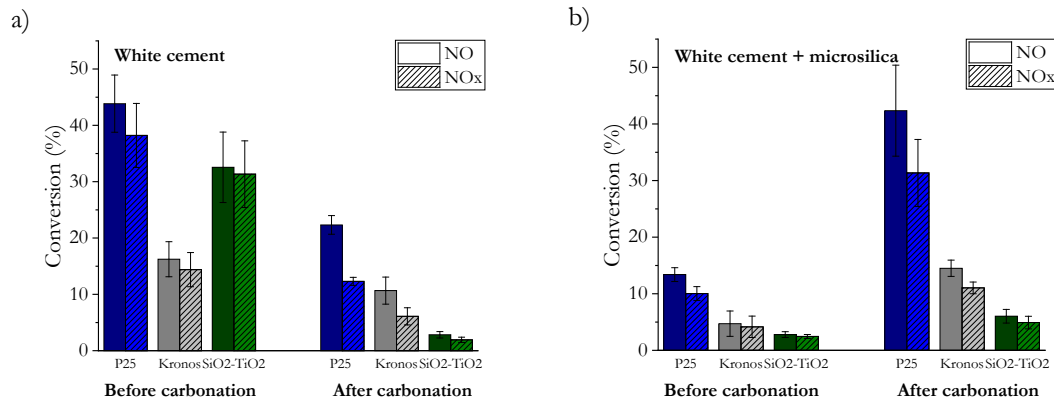


Figure 6.8: The NO and NO_x conversion by photocatalytic a) white cement mortars and b) white cement + microsilica mortars before and after carbonation.

It is worth mentioning that the photocatalytic oxidation rates of cement mortars before the carbonation were similar to those observed in other studies [196], [197]. Upon carbonation, a decrease of photocatalytic performance was observed in all pure cement mortars and an increase in all microsilica containing mortars, following the observed microstructural changes. This behavior will be discussed later in this chapter.

Selectivity

The selectivity of the photocatalytic oxidation of NO, which accounts for the formation and release of NO₂, is presented in Fig. 6.9. The selectivity of photocatalytic conversion observed in this study for the mortars before the carbonation (up to 97%) is higher than that observed, e.g., by Yang et al. [209], where a similar formulation of the mortar was used. This can be an effect of differences in porosity [198], dispersion of titania in the mortar matrix and strong carbonation impact, which is unavoidable during standard curing of the samples. These effects are later discussed in this chapter.

Among the investigated photocatalysts, silica-titania composite revealed the highest selectivity, followed by carbon-doped Kronos titania and titania P25 as the least selective photocatalyst, regardless of the carbonation stage. The superior performance of silica-titania composite and Kronos titania over P25 can be a result of around 4 times higher specific surface area of these photocatalysts. A higher specific surface area results in a higher NO₂

adsorption capacity of the photocatalyst, which is a crucial factor if one considers that NO₂ can be not only further photocatalytically converted but also be adsorbed on the surface and, e.g., undergo disproportionation, as shown by Arana et al. [195]. Additionally, silica-titania composite offers extra hydroxyl groups on the surface and enhanced hydrophilic properties [217]. Even though in the study of Hakki et al. [229] it was shown that Ti-O-Si binding negatively affects the nitrate selectivity, the abovementioned features seem to outbalance this effect. After carbonation, the selectivity of the samples dropped significantly for pure cement-based mortars, whereas only a slight drop was observed for microsilica mortars.

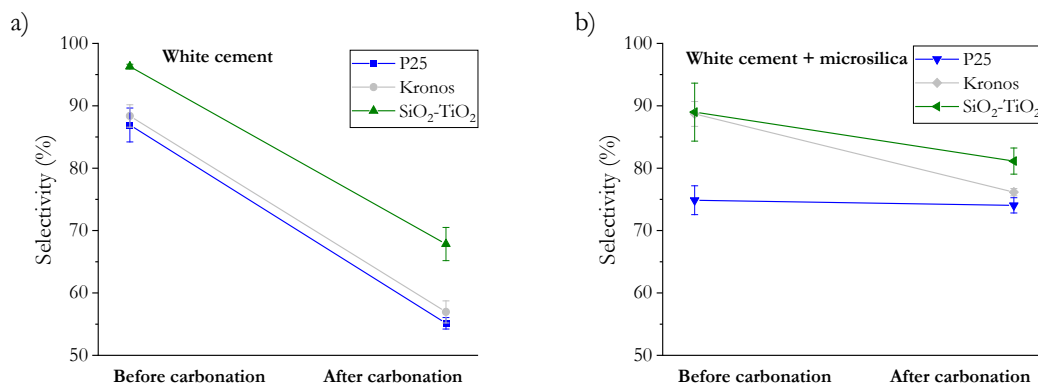


Figure 6.9: Photocatalytic selectivity of NO to nitrate for a) white cement mortar and b) white cement + microsilica mortars before and after accelerated carbonation.

NO₂ adsorption

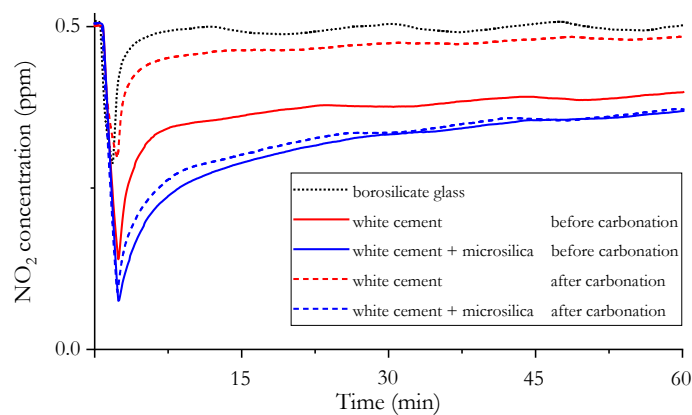


Figure 6.10: Adsorption of NO₂ on the mortars performed in the darkness before and after accelerated carbonation.

The adsorption of NO₂ gas on the surface of the mortar was investigated in darkness following the experimental scheme of the PCO test, before and after carbonation. The

results shown in Fig. 6.10 express that the highest adsorption capacity was observed for mortars with microsilica addition. Furthermore, microsilica mortars maintained their high adsorption capacity even after carbonation. In contrast, a drastic drop of NO₂ adsorption capacity was observed for pure cement-based mortars after carbonation - the measured values were only slightly higher than for borosilicate glass which was used as a reference.

6.4 Discussion

6.4.1 Influence of carbonation on the photocatalytic performance

The comparison between the photocatalytic response of mortars with and without microsilica addition, and three types of photocatalysts used, enabled the determination of the main parameters affecting the photocatalytic performance of mortars upon carbonation. The highest photocatalytic activity was observed for pure cement-based mortars before carbonation. This could be assigned to the presence of capillary pores in the range between 10 and 50 nm since for microsilica mortars, with the prevalence of pores below 10 nm, the NO oxidation rates were about 3 times lower. The predominant role of porosity was further confirmed by the analysis of the microsilica mortars, where as a result of C-S-H (AFt/AFm) phase carbonation, an increase of photocatalytic activity was observed. The improved photocatalytic activity coincided with the occurrence of capillary porosity between 10-50 nm. Therefore, it can be concluded that the microstructural changes caused by C-S-H (AFt/AFm) carbonation boost the photocatalytic activity due to the formation of capillary pores in the range between 10-50 nm, which can outbalance any shielding effects of the carbonates formed (as revealed with thermogravimetric analysis and the phenolphthalein test). In contrast, in the cement mortar series, with high portlandite content, the drop of photocatalytic activity observed upon carbonation was a result of both structural densification and formation of a dense layer of crystalline carbonates, as revealed with SEM analysis. Moreover, shielding effects on the hydration and carbonation products, limiting the TiO₂ exposure on the surface, were substantially stronger when photocatalyst was loaded in the form of agglomerates. Whereas the photocatalytic efficiency of cement mortars with P25 and Kronos titania addition dropped about 1.5-2 times upon carbonation, in mortars with SiO₂-TiO₂ composite agglomerates, photocatalytic performance was reduced more than 10 times.

The impact of capillary pores between 10-50 nm on the photocatalytic properties of mortars observed in this study argues with the previous findings on the influence of porosity on photocatalytic performance. Contradictory to the optimum porosity ranges for pollutants' oxidation presented, e.g., by Rimenez-Relinque et al. [196] between 50 and 500 nm, it is found in this study that the presence of pores in size range between 10-50 nm in the mortars' surface can significantly boost the photocatalytic efficiency. It is shown that capillary porosity in the range between 10-50 nm provides satisfying photocatalytic properties to cementitious mortars and that the elimination of portlandite enables to avoid the drop of the photocatalytic properties upon carbonation.

6.4.2 Influence of carbonation on selectivity

The release of NO₂ to air is not desired since NO₂ is more harmful than NO [230]. Therefore, the selectivity of the photocatalytic reaction towards the elimination of intermediate NO₂ is one of the main issues in the practical application of photocatalytic technology to deal with NO removal. During the photocatalytic process, NO₂ can be further photocatalytically oxidized [231], decomposed via photolysis [232] or be just adsorbed on the surface and, e.g., eliminated via disproportionation [195]. The later route is pH-dependent and therefore, the impact of carbonation becomes crucial. The observed drop of selectivity after the reduction of pH of mortar's surface upon carbonation could be partially explained with this route. However, further investigation is needed. This study shows that the amount of the NO₂ released during the photocatalytic experiments depends not only on the photocatalyst itself but also on the changes of the cementitious matrix upon carbonation. Before carbonation, the selectivity of the photocatalytic reaction was very high for pure cement-based mortars (Fig. 6.9). Similarly, microsilica mortars revealed high selectivity before carbonation, except for the sample with P25 photocatalyst. The lower selectivity of this mortar can be related to the significantly lower specific surface area of the P25 photocatalyst, which in combination with the low porosity of mortars is insufficient to capture the NO₂ when relatively higher amounts of NO are photocatalytically oxidized. For carbonated pure cement samples, a drastic drop was observed when portlandite reacted with CO₂ forming a 'protective' layer of carbonates on the surface and the selectivity was maintained or only slightly reduced for microsilica samples, even though their photocatalytic efficiency increased significantly after carbonation (Fig. 6.8).

On the other hand, the study on the NO₂ adsorption capacity of the mortars in darkness revealed superior properties of microsilica samples over cement samples. In the darkness, only two routes for NO₂ abatement are possible - physical or chemical adsorption. The higher NO₂ adsorption capacity of microsilica mortars over cement mortars could be related to the higher specific surface area of the C-S-H gel compared to the surface area of large portlandite crystals. After carbonation, even though a drop of pH was observed (as shown with the phenolphthalein test) on the surface of both sets of mortars, microsilica mortars maintained their high adsorption capacity. In the study of Thomas et al. [233], it was revealed that the specific surface area of C-S-H gel can be even doubled upon carbonation, as measured by nitrogen gas sorption and small-angle neutron scattering. Therefore, it is suggested that the drop in pH was compensated in this case with the higher specific surface area and porosity of the gel. In contrast, the significant decrease in NO₂ adsorption capacity of cement mortars after carbonation was a result of the formation of a dense layer of carbonate crystals on the surface, which are found to have a lower capacity to adsorb the pollutants [214]. Following the above discussion, a conceptual description of the adsorption of NO₂ on the surface of the mortar is proposed, as shown in Fig. 6.11, underlining the high NO₂ adsorption capacity of microsilica mortars after carbonation, where shielding effects are very limited and the effective surface area is maintained or even increased upon carbonation due to the changes in gel porosity and crack formation.

It is therefore proposed that the cementitious matrix supports NO₂ elimination due to its high NO₂ adsorption capacity related to the high pH and specific surface area of the hydration products. The C-S-H gel is more favorable over portlandite, being able to maintain its high NO₂ adsorption capacity even after carbonation. Furthermore, with low oxidation rates, the ability of the cementitious products/photocatalysts to adsorb NO₂ is the main selectivity controlling factor, whereas, with high pollutant oxidation rates, porosity starts to play a dominant role. The capillary porosity in the range between 10 and 50 nm is shown to increase the selectivity of the photocatalytic reaction. The positive role of open porosity on the NO₂ capture is in agreement with the observations made by Gauvin et al. [198]. This study shows that capillary porosity supports the NO₂ adsorption, presumably due to the prolonged presence of NO₂ close to the sample surface rather than being immediately departed. It is postulated that with lower flows than applied in this study (3 L/min) the overall selectivity towards the elimination of NO₂ would be even higher. The negative

influence of high flow rate and high concentration of the pollutants have been reported in several studies [209], [234]. Despite the sub-optimal experimental conditions applied in this study, the selectivity values were much higher than those observed for pure photocatalysts [206], [211].

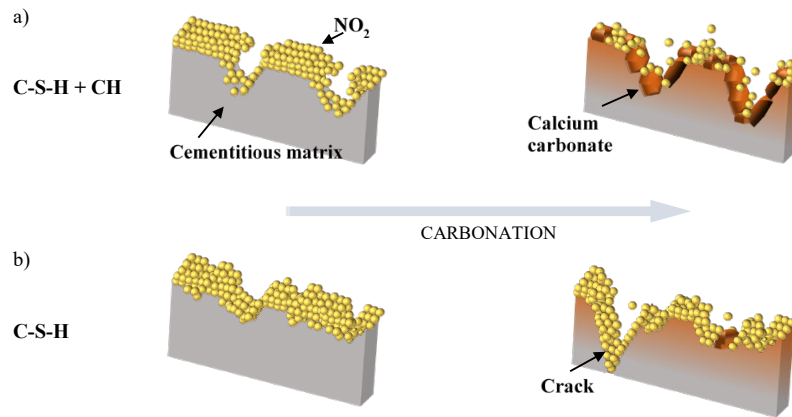


Figure 6.11: Conceptual model of the adsorption of NO_2 on the surface of mortars a) based on pure cement and b) with microsilica addition, before and after carbonation process.

6.5 Conclusions

The impact of carbonation mechanism on the NO_x removal efficiency by cement mortars applying heterogeneous photocatalysis was investigated and the underlying roles of carbonation of portlandite and C-S-H gel were evaluated in this chapter. Pore structure, morphology, and phase composition of the designed mortars were studied. Photocatalytic oxidation efficiency of NO and the related selectivity were determined.

Table 6.3: Carbonation impact on the NO_x oxidation rate by photocatalytic mortars.

	Porosity 10-50 nm	Specific surface area*	TiO ₂ exposure	NO ₂ adsorption capacity	NO _x oxidation rate after carbonation
CH + C-S-H cement mortars	high	high	high	high	low
Carbonation impact	↘	↘	↘	↘	
C-S-H cement + microsilica mortars	low	high	high	high	high
Carbonation impact	↗	↗	→	→	

*Predicted based on the available literature [233], [235].

Table 6.3 presents the summarized influence of carbonation on the properties of mortars and their effect on photocatalytic performance. The present study shows that the photocatalytic properties can be controlled and optimized with the initial mix design of the mortars concerning the influence of carbonation on the mortars' microstructure. Pure cement is not recommended to be used as a matrix for photocatalysts, and instead, the addition of pozzolanic material is suggested. Here, microsilica was chosen as a pozzolanic material. The following detailed conclusions are reached by the acquired results:

- Carbonation of portlandite leads to the structural densification of the mortar in the porosity range between 10-50 nm, and to the formation of the layer of crystal carbonates on the surface, limiting the exposure of TiO₂. In consequence, a drastic decrease of photocatalytic oxidation was observed for white cement mortars. Additionally, agglomeration of photocatalyst escalated the negative impact of the shielding effects and microstructural changes on the photocatalytic activity of mortars upon carbonation.
- Decalcification of C-S-H (AFm/AFt) gel in mortars with the addition of pozzolanic material results in the formation of capillary pores in size range of 10 to 50 nm and an increase of photocatalytic efficiency, indicating dominant effects of porosity restructuring on the photocatalytic performance over the shielding effects caused by the carbonation products when C-S-H gel carbonates.
- The selectivity of photocatalytic processes depends on the type of TiO₂ photocatalyst and the matrix properties. The highest selectivity was observed for the silica-supported composite and was found to be affected by the specific surface area of the photocatalyst. The cementitious matrix can support the elimination of NO₂ due to its high ability to adsorb NO₂, associated with the high pH and specific surface area.
- The reduction of the mortar's selectivity upon carbonation is minimized for mortars with microsilica addition, where mainly C-S-H (AFm/AFt) gel carbonates. The superior impact of the C-S-H gel on the overall reaction selectivity is mainly related to the high specific surface area before and after carbonation and, therefore, the high capacity to adsorb NO₂.
- High pH together with the high specific surface area of the hydration products, favor NO₂ elimination and control the selectivity level and are observed to be

accompanied by low oxidation rates of NO. With higher oxidation rates, the cementitious matrix supports the NO₂ elimination. However, the presence of porosity becomes a limiting factor - a high capillary porosity improves the overall selectivity of the photocatalytic process, possibly due to the prolonged residence time.

Conclusions and recommendations

This thesis focuses on the development of alternative cementitious binders and functionalized materials, aiming at economically and environmentally profitable solutions. Within this path, several topics are explored, including the improvement of currently utilized alkali activated materials technology, the implementation of new cementitious binders, and the assessment of the air purifying potential of concrete. The outcome of this work and corresponding recommendations for future research are summarized below.

7.1 Conclusions

7.1.1 Ambient cured silica-rich alkali activated materials

With the aim to eliminate the need for elevated temperature curing of fly ash-based geopolymers, the addition of small quantities of cement was proposed. The experimental investigation revealed that the partial replacement of fly ash with cement (between 5 and 10 wt%) enables the manufacture of silica-rich alkali-activated products at ambient conditions. While in pure fly ash system setting takes place after a few days of curing, the setting times of the samples containing small cement quantities are comparable to those reported for cement pastes (according to the Vicat test). The accelerated hardening process is a consequence of the fast dissolution of cement phases and precipitation of calcium-enriched gel. However, already up to 7 days of hydration, it is notable that the accelerated hydration of cement within the first hours after contact with the alkaline solution has an adverse effect on its overall reaction degree (in comparison to cement hydrated just with water). The optimal dosage of cement in the fly ash ash-based geopolymeric system depends on the total initial content of silica in the pore solution. The highest 28-days compressive strength was observed with 5 wt% and 7.5 wt% cement addition for silicate-based activator with a silica

modulus of 1.2 and 1.5, respectively. Based on this study, it is postulated that the fast consumption of activator species in the presence of reactive cement and formation of Ca-enriched gel products may impede the dissolution and solidification processes of fly ash between 7 and 28 days of curing.

7.1.2 BOF slag as a cementitious binder

In this thesis, it is demonstrated that despite many technological challenges, BOF slag can be successfully applied as a binding material. This is obtained with the use of potassium and sodium citrate salts, which exhibit the dual role of superplasticizer and activator. The superplasticizing effect of citrates helps to reduce the water demand of the BOF slag, which is a critical factor determining the performance of slag-based products if one considers the inertness and limited or slow reactivity of BOF slag phases. Owing to the superplasticizing properties of potassium and sodium citrates, throughout this research, the BOF slag pastes were produced with a w/b ratio of 0.16 and 0.18. The second “activating” effect of citrate salts is associated with their chelating properties, which enable fast dissolution of phases (especially brownmillerite). In addition, the applied activators are found to significantly increase the pH of the pore solution (as determined after 30 min and 1 hour of hydration), accelerating the reaction of C₂S at early ages. The experimental investigation further revealed that the overall reaction degree of C₂S (after 90 days of hydration) is facilitated in the samples containing relatively low concentrations of citrate salts (0.2 M). In contrast, the extent of brownmillerite reaction is escalated in the samples with highly concentrated citrate solutions (0.6 M).

The hydration of BOF slag (mainly brownmillerite and C₂S) leads to the formation of siliceous hydrogarnets, C-S-H gel, portlandite and hydrotalcite. The formation of these products results in a dense microstructure, and consequently, outstanding mechanical performance of BOF slag pastes (with 28-days compressive strength up to 75 MPa). The strength properties are influenced by the activator dosage, w/b ratio and slag fineness. Further optimization of the reaction kinetics and strength development of the slag mixtures can be achieved via nanosilica addition. However, it must be noted that while nanosilica enhances the precipitation of C-S-H gel, it has a delaying effect on the reaction of brownmillerite.

Finally, the environmental impact of designed BOF slag products needs to be considered. Both brownmillerite and C_2S are the hosting phases for heavy metals, mainly vanadium and chromium, in BOF slag. Even though the leaching of these elements from hydrated slag pastes is insubstantial (as determined with one batch leaching test and tank test), it must be noted that the immobilization capability of slag pastes drastically drops upon carbonation when hydrogarnets and C-S-H gel (hydration products which potentially incorporate heavy metals) react with CO_2 . Therefore, it is recommended to manufacture slag products with low porosity and high contents of portlandite (e.g., by facilitating hydration of C_2S), which helps to increase the carbonation resistance via the formation of a dense layer of carbonates on the surface, impeding the diffusion of CO_2 .

7.1.3 The durability of photocatalytically active mortars

The durability of photocatalytic materials defines its profitability. In this thesis, the effects of carbonation, unavoidably occurring at the concrete surface, on the photocatalytic performance of mortars were investigated. Two series of mortars containing nanotitania particles were prepared. In the first series, white cement was employed as a binder, while in the second series, 40 wt% of white cement was substituted with a pozzolanic material (microsilica) in order to differentiate between the impact of carbonation of C-S-H gel and portlandite on the photocatalytic performance of mortars. The experimental results revealed that white cement should not be used as a sole binder for the manufacture of photocatalytic materials since a dramatic efficiency decrease will be observed during their service life. Carbonation of mortars abundant in portlandite results in structural densification (mainly in the porosity range between 10 and 50 nm) and deposition of a dense layer of carbonate crystals on the surface, considerably limiting the exposure of TiO_2 . In contrast, the carbonation of C-S-H gel is accompanied by the formation of capillary pores, which in the present study, led to the improved photocatalytic properties of mortars containing microsilica after accelerated aging. Accordingly, the dominant role of carbonation-induced microstructural changes over shielding effects caused by carbonates is concluded. The superior photocatalytic properties of mortars with microsilica were further disclosed with the evaluation of the selectivity of photocatalytic oxidation. It was found that in contrast to portlandite, C-S-H gel maintains its high ability to adsorb NO_2 upon carbonation, which can be related to its high specific surface area.

7.2 Recommendations

Cement and concrete technology constitutes an industrial sector with tremendous potential for solutions protecting the environment. As shown in this thesis, materials from industrial waste streams, which are often landfilled, e.g., due to contamination with heavy metals, can be utilized for the manufacture of building products, receiving high market value. Concrete also serves as a safety material, protecting the environment from exposure to fire or chemical attack (e.g. with the use of geopolymers). Finally, with the application of photocatalytic technology, concrete constitutes a suitable candidate for the abatement of air pollutants. All these outstanding concrete features require the development of technological solutions that are economically competitive, easily applicable, and, most importantly, safe. In this context, some general recommendations for future research, which were recognized throughout performing this work, are given, followed by specific suggestions for each analysed topic.

- The chemistry and mineralogy of currently utilized supplementary cementitious materials (SCMs) are well defined, which guarantees their predictable performance and safety. The assessment of the new potential cementitious binders should be performed on the level of individual phases in order to foresee the long-term properties of the designed building product and to assess the changes in their performance when the composition varies within the same by-product/waste. In this way, the applicability of the whole range of materials with similar chemistry can be easier addressed.
- Before the real-scale applications, the durability of the newly designed products containing by-products/wastes should be thoroughly investigated. Attention should be paid to the fact that the methodology employed for durability assessment of traditional cementitious products may be insufficient or inaccurate for the materials manufactured from industrial wastes, which often contain heavy metals, expansive phases, or large quantities of organic components.
- The research on the durability of concretes designed for air-purifying purposes should be extended to prevent large-scale applications with little or no environmental profit in the long term perspective. The recognition of the main causes for the commonly observed loss of photocatalytic efficiency of building products during their service life should be a point of departure for the implementation of the new solutions. For the concrete mixtures with nanotitania

particles, not only the mechanical damage (including washing or wearing processes) but also microstructural and compositional changes upon progressive hydration and carbonation during their service life, need to be considered. At the moment, the ratio between the research on the durability of photocatalytic products and the research on the performance of different photocatalytic products is disconcertingly low.

- To enable the widespread application of new cementitious binders, the commonly applied methods to assess their reactivity and durability should be revisited and revised. Extensive research on the mineralogy of SCMs and the development of the test methods for their characterization are needed to constitute new measures for quality control and to standardize the testing methodology for their use in concrete.

More specific recommendations related to this work are as follows.

7.2.1 Ambient cured silica-rich alkali activated materials

- Since hydration of cement between 7 and 28 days of curing is suppressed at highly alkaline conditions, the mechanical profits as well as the economic aspects of analysed hybrid fly ash-cement systems are not optimized. It is therefore recommended either to lower the alkalinity of activating solution and increase the content of cement in the mixture or to consider other calcium sources (revealing high reaction degree under alkaline conditions). The content of the selected additive should be regulated not only based on the reactivity of applied precursors but also the activator characteristics, e.g., silica modulus, as shown in this thesis.
- The impact of cement (or other calcium-rich material) addition on the desired geopolymeric properties, e.g., fire resistance or chemical attack resistance, should be evaluated in order to ensure that with the new formulations, the products maintain their outstanding properties.

7.2.2 BOF slag as a cementitious binder

- Even though in the present work BOF slag-based products show very promising properties, further investigation of the durability aspects is essential for their widespread application. In this work, samples were sealed-cured for 90 days before being tested for carbonation resistance and for a minimum of 28 days before the evaluation of heavy metals leaching. However, in real applications, the exposure of these materials to atmospheric conditions is expected to take place much earlier,

which might affect the mobility of heavy metals and raise the risk of efflorescence formation. Moreover, since slags often contain large quantities of expansive components, the volume expansion also needs to be evaluated.

- In this thesis, BOF-slag products were investigated mostly on the paste level. Exemplary mortar formulations revealed substantially lower mechanical performance than pastes. Followingly, attention should be paid to the design of mortar and concrete mixtures with optimised particle packing and improved interfacial transition zone (ITZ) between paste and aggregate.
- Potassium and sodium citrates have shown to be effective activators and superplasticizers enabling the production of high-quality products from BOF slag. In this context, other chelators (e.g., lactate, malate, tartrate, or EDTA) should also be researched to provide solutions offering superior properties and the best economic value.

7.2.3 The durability of photocatalytically active mortars

- In this thesis, three types of titania nanoparticles (P25, KRONOclean 7000, and SiO₂-TiO₂ composite), intermixed with the cementitious matrix, were used at a constant dosage of 5 wt%. It was revealed that the photocatalytic performance of mortars upon carbonation drops more significantly for samples with silica-titania composite, where the total TiO₂ content is more than 6 times lower than in samples with titania P25 and KRONOclean 7000. This behavior indicates that next to the phase composition, the dosage of nanotitania (and likely, associated pore structure modification) has a strong impact on the photocatalytic performance of mortars upon carbonation, which should be further investigated.

Bibliography

- [1] “Cement technology roadmap.” <https://www.wbcds.org/Sector-Projects/Cement-Sustainability-Initiative/News/Cement-technology-roadmap-shows-how-the-path-to-achieve-CO2-reductions-up-to-24-by-2050> (accessed Oct. 07, 2020).
- [2] M. Schneider, “The cement industry on the way to a low-carbon future,” *Cem. Concr. Res.*, vol. 124, p. 105792, 2019.
- [3] “The Paris Agreement | UNFCCC.” <https://unfccc.int/process-and-meetings/the-paris-agreement/the-paris-agreement> (accessed Oct. 07, 2020).
- [4] M. C. G. Juenger, R. Snellings, and S. A. Bernal, “Supplementary cementitious materials: New sources, characterization, and performance insights,” *Cem. Concr. Res.*, vol. 122, pp. 257–273, 2019.
- [5] C. Shi, B. Qu, and J. L. Provis, “Recent progress in low-carbon binders,” *Cem. Concr. Res.*, vol. 122, pp. 227–250, 2019.
- [6] J. L. Provis and J. S. J. van Deventer, *Alkali Activated Materials: State-of-the-Art Report*, RILEM TC 224-AAM. Dordrecht: Springer, 2014.
- [7] J. L. Provis, “Activating solution chemistry for geopolymers,” in *Geopolymers: Structures, Processing, Properties and Industrial Applications*, Cambridge: CRC Press, pp. 50–71, 2009.
- [8] H. Kühl, “Slag cement and process of making the same,” 900,939, Jul. 03, 1908.
- [9] A. O. Purdon, “The action of alkalis on blast-furnace slag,” *J. Soc. Chem. Ind.*, vol. 59, pp. 191–202, 1940.
- [10] V. D. Glukhovskiy, *Gruntosilikaty (Soil silicates)*. Kiev: Gosstroyizdat Publishing (in Russian), 1959.
- [11] A. Derdacka-Grzymek and A. Stok, “Bezcementowe spoiwo z popiołu lotnego,” *Cem. Wapno Bet.*, no. 8–9, pp. 220–220, 1980.
- [12] B. Talling and J. Brandstetr, “Present state and future of alkali-activated slag concretes,” *Fly ash, Silica fume, Slag Nat. Pozzolans Concr. Proc. Third Int. Conf.*, vol. 114, pp. 1519–1545, 1989.
- [13] J. Malolepszy and J. Deja, “The influence of curing conditions on the mechanical properties of alkali slag binders,” *Silic. Ind.*, vol. 53, no. 11–12, 1988.
- [14] J. Deja, “Carbonation aspects of alkali activated slag mortars and concretes,” *Silic. Ind.*, no. 3–4, 2002.
- [15] S. Wang, “Review of recent research on alkali-activated concrete in China,” *Mag. Concr. Res.*, vol. 43, no. 154, pp. 29–35, 1991.

- [16] J. Davidovits, "Geopolymers - Inorganic polymeric new materials," *J. Therm. Anal.*, vol. 37, pp. 1633–1656, 1991.
- [17] R. Snellings, "CoverPicture." 2016.
- [18] R. Snellings, "Assessing, Understanding and Unlocking Supplementary Cementitious Materials," *RILEM Tech. Lett.*, vol. 1, pp. 50–55, 2016.
- [19] M. Schneider, "The cement industry on the way to a low-carbon future," *Cem. Concr. Res.*, vol. 124, p. 105792, 2019.
- [20] A. Fujishima and K. Honda, "Electrochemical photolysis of water at a semiconductor electrode," *Nature*, vol. 238, pp. 37–38, 1972.
- [21] M. M. Ballari, Q. L. Yu, and H. J. H. Brouwers, "Experimental study of the NO and NO₂ degradation by photocatalytically active concrete," *Catal. Today*, vol. 161, pp. 175–180, 2011.
- [22] W. J. Steyn, J. Harvey, and K. Gopalakrishnan, *Climate Change, Energy, Sustainability and Pavements*. New York: Springer, 2014.
- [23] "W Warszawie ze smogiem miał walczyć chodnik. Ale czy da sobie radę? - SmogLab." <https://smoglab.pl/w-warszawie-ze-smogiem-mial-walczyc-chodnik-ale-czy-da-sobie-rade/> (accessed Nov. 01, 2020).
- [24] R. Hingorani, E. Jimenez-Relinque, M. Grande, A. Castillo, R. Nevshupa, and M. Castellote, "From analysis to decision: Revision of a multifactorial model for the in situ assessment of NO_x abatement effectiveness of photocatalytic pavements," *Chem. Eng. J.*, vol. 402, p. 126250, 2020.
- [25] J. M. Cordero, R. Hingorani, E. Jimenez-Relinque, M. Grande, R. Borge, A. Narros, and M. Castellote, "NO_x removal efficiency of urban photocatalytic pavements at pilot scale," *Sci. Total Environ.*, vol. 719, p. 137459, 2020.
- [26] E. Jimenez-Relinque, M. Grande, T. Duran, Á. Castillo, and M. Castellote, "Environmental impact of nano-functionalized construction materials: leaching of titanium and nitrates from photocatalytic pavements under outdoor conditions," *Sci. Total Environ.*, vol. 744, p. 140817, 2020.
- [27] P. Duxson, J. L. Provis, G. C. Lukey, S. W. Mallicoat, W. M. Kriven, and J. S. J. Van Deventer, "Understanding the relationship between geopolymer composition, microstructure and mechanical properties," *Colloids Surfaces A Physicochem. Eng. Asp.*, vol. 269, no. 1–3, pp. 47–58, 2005.
- [28] M. Criado, A. Fernandez-Jimenez, A. G. de la Torre, M. A. G. Aranda, and A. Palomo, "An XRD study of the effect of the SiO₂/Na₂O ratio on the alkali activation of fly ash," *Cem. Concr. Res.*, vol. 37, pp. 671–679, 2007.
- [29] T. Bakharev, "Geopolymeric materials prepared using Class F fly ash and elevated temperature curing," *Cem. Concr. Res.*, vol. 35, no. 6, pp. 1224–1232, 2005.
- [30] G. Habert, J. B. D’Espinose De Lacaillerie, and N. Roussel, "An environmental evaluation of geopolymer based concrete production: Reviewing current research trends," *J. Clean. Prod.*, vol. 19, no. 11, pp. 1229–1238, 2011.

- [31] B. Tempest, C. Snell, T. Gentry, M. Trejo, and K. Isherwood, "Manufacture of full-scale geopolymer cement concrete components: A case study to highlight opportunities and challenges," *PCI J.*, pp. 39–50, 2015.
- [32] R. R. Lloyd, "Accelerated ageing of geopolymers," in *Geopolymers: Structures, Processing, Properties and Industrial Applications*, Cambridge: CRC Press, 2009, pp. 139–166.
- [33] P. De Silva and K. Sagoe-Crenstil, "Medium-term phase stability of Na₂O-Al₂O₃-SiO₂-H₂O geopolymer systems," *Cem. Concr. Res.*, vol. 38, pp. 870–876, 2008.
- [34] P. Krivenko, G. Kovalchuk, and O. Kovalchuk, "Hybrid fly ash based alkali activated cements," *Conf. Pap. Brno*, pp. 66–72, 2013.
- [35] A. Fernández-Jiménez and F. Puertas, "Setting of alkali-activated slag cement. Influence of activator nature," *Adv. Cem. Res.*, vol. 13, no. 3, pp. 115–121, 2001.
- [36] J. Temuujin, A. Van Riessen, and R. Williams, "Influence of calcium compounds on the mechanical properties of fly ash geopolymer pastes," *J. Hazard. Mater.*, vol. 167, pp. 82–88, 2009.
- [37] J. Davidovits, "Geopolymers - Inorganic polymeric new materials," *J. Therm. Anal.*, vol. 37, pp. 1633–1656, 1991.
- [38] I. García-Lodeiro, A. Fernández-Jiménez, and A. Palomo, "Variation in hybrid cements over time. Alkaline activation of fly ash-portland cement blends," *Cem. Concr. Res.*, vol. 52, pp. 112–122, 2013.
- [39] I. Garcia-Lodeiro, S. Donatello, A. Fernández-Jiménez, and Á. Palomo, "Hydration of Hybrid Alkaline Cement Containing a Very Large Proportion of Fly Ash: A Descriptive Model," *Materials (Basel)*, vol. 9, no. 8, p. 605, 2016.
- [40] C. K. Yip, G. C. Lukey, J. L. Provis, and J. S. J. van Deventer, "Effect of calcium silicate sources on geopolymerisation," *Cem. Concr. Res.*, vol. 38, pp. 554–564, 2008.
- [41] P. Nath and P. K. Sarker, "Use of OPC to improve setting and early strength properties of low calcium fly ash geopolymer concrete cured at room temperature," *Cem. Concr. Compos.*, vol. 55, pp. 205–214, 2015.
- [42] T. Suwan, M. Fan, and N. Braimah, "Internal heat liberation and strength development of self-cured geopolymers in ambient curing conditions," *Constr. Build. Mater.*, vol. 114, pp. 297–306, 2016.
- [43] I. Garcia-lodeiro, A. Palomo, A. Fernández-jiménez, and D. E. Macphee, "Compatibility studies between N-A-S-H and C-A-S-H gels. Study in the ternary diagram Na₂O-CaO-Al₂O₃-SiO₂-H₂O," *Cem. Concr. Res.*, vol. 41, pp. 923–931, 2011.
- [44] Y. Ma, *Microstructure and Engineering Properties of Alkali Activated Fly Ash -as an environment friendly alternative to Portland cement*. PhD thesis, 2013.
- [45] F. Škvára, T. Jílek, and L. Kopecký, "Geopolymer materials based on fly ash," *Ceram. - Silikaty*, vol. 49, no. 3, pp. 195–204, 2005.
- [46] F. Winnefeld, A. Leemann, M. Lucuk, P. Svoboda, and M. Neuroth, "Assessment of phase formation in alkali activated low and high calcium fly ashes in building

- materials,” *Constr. Build. Mater.*, vol. 24, pp. 1086–1093, 2010.
- [47] C. A. Rees, J. L. Provis, G. C. Lukey, and J. S. J. Van Deventer, “In situ ATR-FTIR study of the early stages of fly ash geopolymer gel formation,” *Langmuir*, vol. 23, no. 17, pp. 9076–9082, 2007.
- [48] P. Duxson, S. W. Mallicoat, G. C. Lukey, W. M. Kriven, and J. S. J. van Deventer, “The effect of alkali and Si/Al ratio on the development of mechanical properties of metakaolin-based geopolymers,” *Colloids Surfaces A Physicochem. Eng. Asp.*, vol. 292, no. 1, pp. 8–20, 2007.
- [49] C. A. Rees, J. L. Provis, G. C. Lukey, and J. S. J. Van Deventer, “Attenuated total reflectance fourier transform infrared analysis of fly ash geopolymer gel aging,” *Langmuir*, vol. 23, pp. 8170–8179, 2007.
- [50] X. Gao, Q. L. Yu, and H. J. H. Brouwers, “Reaction kinetics, gel character and strength of ambient temperature cured alkali activated slag–fly ash blends,” *Constr. Build. Mater.*, vol. 80, pp. 105–115, 2015.
- [51] “BS-EN-196-1. Methods of testing cement – Part 1: determination of strength,” *Br. Stand. Institution-BSI CEN Eur. Comm. Stand.*, 2005.
- [52] “BS-EN-196-3. Methods of testing cement – Part 3: determination of setting times and soundness,” *Br. Stand. Institution-BSI CEN Eur. Comm. Stand.*, 2005.
- [53] I. Soroka, “The determination of setting time of portland cement by the vicat test,” *Cem. Concr. Res.*, vol. 14, no. 6, pp. 884–886, 1984.
- [54] T. Suwan and M. Fan, “Influence of OPC replacement and manufacturing procedures on the properties of self-cured geopolymer,” *Constr. Build. Mater.*, vol. 73, pp. 551–561, 2014.
- [55] J. H. M. Visser, “Fundamentals of alkali-silica gel formation and swelling: Condensation under influence of dissolved salts,” *Cem. Concr. Res.*, vol. 105, pp. 18–30, 2018.
- [56] R. K. Iler, *The chemistry of silica: solubility, polymerization, colloid and surface properties, and biochemistry*. New York: John Wiley & Sons, 1979.
- [57] F. Gaboriaud, A. Nonat, D. Chaumont, and A. Craievich, “Structural model of gelation processes of a sodium silicate sol destabilized by calcium ions: Combination of SAXS and rheological measurements,” *J. Non. Cryst. Solids*, vol. 351, no. 4, pp. 351–354, 2005.
- [58] M. Criado, A. Fernández-Jiménez, and A. Palomo, “Alkali activation of fly ash: Effect of the SiO₂/Na₂O ratio. Part I: FTIR study,” *Microporous Mesoporous Mater.*, vol. 106, pp. 180–191, 2007.
- [59] W. K. W. Lee and J. S. J. Van Deventer, “Use of Infrared Spectroscopy to Study Geopolymerization of Heterogeneous Amorphous Aluminosilicates,” *Langmuir*, no. 7, pp. 8726–8734, 2003.
- [60] A. Palomo, A. Fernández-Jiménez, G. Kovalchuk, L. M. Ordonez, and M. C. Naranjo, “Opc-fly ash cementitious systems : study of gel binders produced during alkaline hydration,” *Adv. Geopolymer Sci.*, pp. 2958–2966, 2007.

- [61] I. Halasz, M. Agarwal, R. Li, and N. Miller, "What can vibrational spectroscopy tell about the structure of dissolved sodium silicates?," *Microporous Mesoporous Mater.*, vol. 135, pp. 74–81, 2010.
- [62] I. Halasz, A. Mukesh, N. Miller, and R. Li, "Vibrational spectra and dissociation of aqueous Na_2SiO_3 solutions," *Catal. Letters*, vol. 117, 2014.
- [63] H. Jansson, D. Bernin, and K. Ramser, "Silicate species of water glass and insights for alkali-activated green cement," *AIP Adv.*, vol. 5, p. 067167, 2015.
- [64] X. Yang, P. Roonasi, and A. Holmgren, "A study of sodium silicate in aqueous solution and sorbed by synthetic magnetite using in situ ATR-FTIR spectroscopy," *J. Colloid Interface Sci.*, vol. 328, pp. 41–47, 2008.
- [65] J. L. Bass and G. Turner, "Anion distributions in sodium silicate solutions. Characterization by ^{29}Si NMR and infrared spectroscopies, and vapor phase osmometry," *J. Phys. Chem. B*, vol. 101, pp. 10638–10644, 1997.
- [66] J. L. Provis, A. Hajimohammadi, C. A. Rees, and J. S. J. Van Deventer, "Analysing and Manipulating the Nanostructure of Geopolymers," *Nanotechnol. Constr.*, pp. 113-118 437, 2009.
- [67] W. R. Taylor, "Application of infrared spectroscopy to studies of silicate glass structure: Examples from the melilite glasses and the systems $\text{Na}_2\text{O}-\text{SiO}_2$ and $\text{Na}_2\text{O}-\text{Al}_2\text{O}_3-\text{SiO}_2$," *Proc. Indian Acad. Sci. - Earth Planet. Sci.*, vol. 99, pp. 99–117, 1990.
- [68] Z. Zhang, H. Wang, and J. L. Provis, "Quantitative study of the reactivity of fly ash in geopolymerization by FTIR," *J. Sustain. Cem. Mater.*, vol. 1, pp. 154–166, 2012.
- [69] S. Zhang, A. Keulen, K. Arbi, and G. Ye, "Waste glass as partial mineral precursor in alkali-activated slag/fly ash system," *Cem. Concr. Res.*, vol. 102, pp. 29–40, 2017.
- [70] F. Skavara, L. Kopecky, J. Nemecek, and Z. Bittnar, "Microstructure of Geopolymer Materials Based on Fly Ash," *Ceramics*, vol. 50, pp. 208–215, 2006.
- [71] S. Alahrache, F. Winnefeld, J. B. Champenois, F. Hesselbarth, and B. Lothenbach, "Chemical activation of hybrid binders based on siliceous fly ash and Portland cement," *Cem. Concr. Compos.*, vol. 66, pp. 10–23, 2016.
- [72] I. G. Richardson, A. V. Girão, R. Taylor, and S. Jia, "Hydration of water- and alkali-activated white Portland cement pastes and blends with low-calcium pulverized fuel ash," *Cem. Concr. Res.*, vol. 83, pp. 1–18, 2016.
- [73] R. L. Frost, M. C. Hales, and W. N. Martens, "Thermogravimetric analysis of selected group (II) carbonate minerals - Implication for the geosequestration of greenhouse gases," *J. Therm. Anal. Calorim.*, vol. 95, pp. 999–1005, 2009.
- [74] J. Tailby and K. J. D. Mackenzie, "Structure and mechanical properties of aluminosilicate geopolymer composites with Portland cement and its constituent minerals," *Cem. Concr. Res.*, vol. 40, pp. 787–794, 2010.
- [75] C. Shi, "Characteristics and cementitious properties of ladle slag fines from steel production," *Cem. Concr. Res.*, vol. 32, pp. 459–462, 2002.
- [76] A. van Zomeren, S. R. van der Laan, H. B. A. Kobesen, W. J. J. Huijgen, and R. N.

- J. Comans, “Changes in mineralogical and leaching properties of converter steel slag resulting from accelerated carbonation at low CO₂ pressure,” *Waste Manag.*, vol. 31, pp. 2236–2244, 2011.
- [77] S. Y. Pan, R. Adhikari, Y. H. Chen, P. Li, and P. C. Chiang, “Integrated and innovative steel slag utilization for iron reclamation, green material production and CO₂ fixation via accelerated carbonation,” *J. Clean. Prod.*, vol. 137, pp. 617–631, 2016.
- [78] S. Z. Carvalho, F. Vernilli, B. Almeida, M. Demarco, and S. N. Silva, “The recycling effect of BOF slag in the portland cement properties,” *Resour. Conserv. Recycl.*, vol. 127, no. September, pp. 216–220, 2017.
- [79] “Euroslag,” 2016. <http://www.euroslag.com/products/statistics/2016/> (accessed Jul. 19, 2018).
- [80] D. Wang, J. Chang, and W. S. Ansari, “The effects of carbonation and hydration on the mineralogy and microstructure of basic oxygen furnace slag products,” *J. CO₂ Util.*, vol. 34, pp. 87–98, 2019.
- [81] F. Han and Z. Zhang, “Properties of 5-year-old concrete containing steel slag powder,” *Powder Technol.*, vol. 334, pp. 27–35, 2018.
- [82] J. Li, Q. Yu, J. Wei, and T. Zhang, “Structural characteristics and hydration kinetics of modified steel slag,” *Cem. Concr. Res.*, vol. 41, pp. 324–329, 2011.
- [83] F. Han, Z. Zhang, D. Wang, and P. Yan, “Hydration heat evolution and kinetics of blended cement containing steel slag at different temperatures,” *Thermochim. Acta*, vol. 605, pp. 43–51, 2015.
- [84] Y. Jiang, T. C. Ling, C. Shi, and S. Y. Pan, “Characteristics of steel slags and their use in cement and concrete—A review,” *Resour. Conserv. Recycl.*, vol. 136, pp. 187–197, 2018.
- [85] B. Das, S. Prakash, P. S. R. Reddy, and V. N. Misra, “An overview of utilization of slag and sludge from steel industries,” *Resour. Conserv. Recycl.*, vol. 50, pp. 40–57, 2007.
- [86] L. De Windt, P. Chaurand, and J. Rose, “Kinetics of steel slag leaching: Batch tests and modeling,” *Waste Manag.*, vol. 31, pp. 225–235, 2011.
- [87] E. Belhadj, C. Diliberto, and A. Lecomte, “Characterization and activation of Basic Oxygen Furnace slag,” *Cem. Concr. Compos.*, vol. 34, pp. 34–40, 2012.
- [88] Q. Wang, J. W. Yang, and P. Y. Yan, “Influence of initial alkalinity on the hydration of steel slag,” *Sci. China Technol. Sci.*, vol. 55, pp. 3378–3387, 2012.
- [89] S. Kourounis, S. Tsivilis, P. E. Tsakiridis, G. D. Papadimitriou, and Z. Tsibouki, “Properties and hydration of blended cements with steelmaking slag,” *Cem. Concr. Res.*, vol. 37, pp. 815–822, 2007.
- [90] Y. M. Kim and S. H. Hong, “Influence of minor ions on the stability and hydration rates of β -dicalcium silicate,” *J. Am. Ceram. Soc.*, vol. 87, pp. 900–905, 2004.
- [91] B. Z. Dilnesa, E. Wieland, B. Lothenbach, R. Dähn, and K. L. Scrivener, “Fe-containing phases in hydrated cements,” *Cem. Concr. Res.*, vol. 58, pp. 45–55, 2014.

- [92] B. Z. Dilnesa, B. Lothenbach, G. Renaudin, A. Wichser, and D. Kulik, "Synthesis and characterization of hydrogarnet $\text{Ca}_3(\text{Al}_x\text{Fe}_{1-x})_2(\text{SiO}_4)_y(\text{OH})_{4(3-y)}$," *Cem. Concr. Res.*, vol. 59, pp. 96–111, 2014.
- [93] K. L. Scrivener, T. Füllmann, E. Gallucci, G. Walenta, and E. Bermejo, "Quantitative study of Portland cement hydration by X-ray diffraction/Rietveld analysis and independent methods," *Cem. Concr. Res.*, vol. 34, pp. 1541–1547, 2004.
- [94] F. Bullerjahn, M. Ben Haha, and K. L. Scrivener, "Iron solid solutions of ye' elimite - Effect on reactivity," 19. Int. Baustofftagung Ibausil, 2015.
- [95] W. Kurdowski, *Cement and Concrete Chemistry*. Netherlands: Springer, 2014.
- [96] W. Schwarz, "Novel cement matrices by accelerated hydration of the ferrite phase in portland cement via chemical activation: kinetics and cementitious properties," *Adv. Cem. Based Mater.*, vol. 2, pp. 189–200, 1995.
- [97] W. Stumm, *Chemistry of the Solid-Water Interface*. New York: John Wiley & Sons, 1992.
- [98] G. Möschner, B. Lothenbach, R. Figi, and R. Kretzschmar, "Influence of citric acid on the hydration of Portland cement," *Cem. Concr. Res.*, vol. 39, pp. 275–282, 2009.
- [99] M. E. Ramos and F. J. Huertas, "Adsorption of lactate and citrate on montmorillonite in aqueous solutions," *Appl. Clay Sci.*, vol. 90, pp. 27–34, 2014.
- [100] B. Mota, T. Matschei, and K. Scrivener, "Impact of NaOH and Na_2SO_4 on the kinetics and microstructural development of white cement hydration," *Cem. Concr. Res.*, vol. 108, pp. 172–185, 2018.
- [101] C. van Hoek, J. Small, and S.R. van der Laan, "Large-Area Phase Mapping Using PhAse Recognition and Characterization (PARC) Software," *Micros. Today*, vol. 24, pp. 12–21, 2016.
- [102] D. Jansen, F. Goetz-Neunhoeffler, C. Stabler, and J. Neubauer, "A remastered external standard method applied to the quantification of early OPC hydration," *Cem. Concr. Res.*, vol. 41, pp. 602–608, 2011.
- [103] D. Jansen, C. Stabler, F. Goetz-Neunhoeffler, S. Dittrich, and J. Neubauer, "Does Ordinary Portland Cement contain amorphous phase? A quantitative study using an external standard method," *Powder Diffr.*, vol. 26, pp. 31–38, 2011.
- [104] A. C. A. Muller and K. L. Scrivener, "A reassessment of mercury intrusion porosimetry by comparison with ^1H NMR relaxometry," *Cem. Concr. Res.*, vol. 100, pp. 350–360, 2017.
- [105] "Soil Quality Decree," 2015. <http://wetten.overheid.nl/BWBR0023085/2015-07-01#BijlageA> (accessed Jul. 19, 2018).
- [106] J. T. Pacanovsky, L. Huang, T. Frank, and M. Samy, "Hydration control of cementitious systems," 1996, [Online]. Available: <https://patents.google.com/patent/US5634972A/en>.
- [107] I. Strandkvist, Å. Sandström, and F. Engström, "Effect of FeO/MgO Ratio on Dissolution and Leaching of Magnesio-wüstite," *Steel Res. Int.*, vol. 88, pp. 1–7, 2017.

- [108] G. R. Qian, D. D. Sun, J. H. Tay, and Z. Y. Lai, "Hydrothermal reaction and autoclave stability of Mg bearing RO phase in steel slag," *Br. Ceram. Trans.*, vol. 101, pp. 159–164, 2002.
- [109] R. S. Gollop and H. F. W. Taylor, "Microstructural and microanalytical studies of sulfate attack. II. Sulfate-resisting Portland cement: Ferrite composition and hydration chemistry," *Cem. Concr. Res.*, vol. 24, pp. 1347–1358, 1994.
- [110] B. Lothenbach and E. Wieland, "A thermodynamic approach to the hydration of sulphate-resisting Portland cement," *Waste Manag.*, vol. 26, pp. 706–719, 2006.
- [111] H. F. W. Taylor and D. E. Newbury, "An electron microprobe study of a mature cement paste," *Cem. Concr. Res.*, vol. 14, pp. 565–573, 1984.
- [112] V. Morin, P. Termkhajornkit, B. Huet, and G. Pham, "Impact of quantity of anhydrite, water to binder ratio, fineness on kinetics and phase assemblage of belite-ye'elinite-ferrite cement," *Cem. Concr. Res.*, vol. 99, pp. 8–17, 2017.
- [113] S. Hillier, D. G. Lumsdon, R. Brydson, and E. Paterson, "Hydrogarnet: A host phase for Cr(VI) in chromite ore processing residue (COPR) and other high pH wastes," *Environ. Sci. Technol.*, vol. 41, pp. 1921–1927, 2007.
- [114] S. Fujita, K. Suzuki, Y. Shibasaki, and T. Mori, "Synthesis of hydrogarnet from molten slag and its hydrogen chloride fixation performance at high temperature," *J. Mater. Cycles Waste Manag.*, vol. 4, pp. 70–76, 2002.
- [115] M. Zajac, S. K. Bremseth, M. Whitehead, and M. Ben Haha, "Effect of $\text{CaMg}(\text{CO}_3)_2$ on hydrate assemblages and mechanical properties of hydrated cement pastes at 40 °C and 60 °C," *Cem. Concr. Res.*, vol. 65, pp. 21–29, 2014.
- [116] K. Rozov, U. Berner, C. Taviot-Gueho, F. Leroux, G. Renaudin, D. Kulik, L. W. Diamond, "Synthesis and characterization of the LDH hydrotalcite-pyroaurite solid-solution series," *Cem. Concr. Res.*, vol. 40, pp. 1248–1254, 2010.
- [117] N. K. Labhasetwar, "Mossbauer Study on Iron-Exchanged Calcium Silicate Hydrate," *J. Solid State Chem.*, vol. 87, pp. 82–87, 1991.
- [118] V. Daux, G. Christophe, T. Advocat, J. L. Crovisier, and P. Stille, "Kinetic aspects of basaltic glass dissolution at 90°C: Role of aqueous silicon and aluminium," *Chem. Geol.*, vol. 142, pp. 109–126, 1997.
- [119] J. S. J. van Deventer, J. L. Provis, P. Duxson, and G. C. Lukey, "Reaction mechanisms in the geopolymeric conversion of inorganic waste to useful products," *J. Hazard. Mater.*, vol. 139, pp. 506–513, 2007.
- [120] N. Ye, Y. Chen, J. Yang, S. Liang, Y. Hu, J. Hu, S. Zhu, W. Fan, B. Xiao, "Transformations of Na, Al, Si and Fe species in red mud during synthesis of one-part geopolymers," *Cem. Concr. Res.*, vol. 101, pp. 123–130, 2017.
- [121] Y. Ma and G. Ye, "The shrinkage of alkali activated fly ash," *Cem. Concr. Res.*, vol. 68, pp. 75–82, 2015.
- [122] A. Poletini, R. Pomi, and P. Sirini, "Fractional factorial design to investigate the influence of heavy metals and anions on acid neutralization behavior of cement-based products," *Environ. Sci. Technol.*, vol. 36, pp. 1584–1591, 2002.

- [123] A. Vollpracht and W. Brameshuber, "Binding and leaching of trace elements in Portland cement pastes," *Cem. Concr. Res.*, vol. 79, pp. 76–92, 2016.
- [124] N. D. M. Evans, "Binding mechanisms of radionuclides to cement," *Cem. Concr. Res.*, vol. 38, pp. 543–553, 2008.
- [125] I. Moulin, J. Rose, W. Stone, and J. Bottero, "Lead, zinc and chromium (III) and (VI) speciation in hydrated cement phases," *Waste Mater. Constr.*, pp. 269–280, 2000.
- [126] I. T. Burke, W. M. Mayes, C. L. Peacock, A. P. Brown, A. P. Jarvis, and K. Gruiz, "Speciation of arsenic, chromium, and vanadium in red mud samples from the Ajka spill site, Hungary," *Environ. Sci. Technol.*, vol. 46, pp. 3085–3092, 2012.
- [127] H. J. H. Brouwers, A hydration model of Portland Cement using the work of Powers and Brownyard. Skokie, Illinois, U.S.: Eindhoven University of Technology/Portland Cement Association, 2011. PCA Report No. SN3039. http://www2.cement.org/pdf_files/SN3039.pdf
- [128] T. Zhang, P. Gao, R. Luo, Y. Guo, J. Wei, and Q. Yu, "Measurement of chemical shrinkage of cement paste: Comparison study of ASTM C 1608 and an improved method," *Constr. Build. Mater.*, vol. 48, pp. 662–669, 2013.
- [129] W. Chen, Hydration of Slag Cement. Theory, Modeling and Application, PhD Thesis. Twente University, 2007.
- [130] F. Avet and K. Scrivener, "Effect of temperature on the water content of C-A-S-H in plain Portland and blended cements," *Cem. Concr. Res.*, vol. 136, p. 106124, 2020.
- [131] M. H. Zhang, J. Islam, and S. Peethamparan, "Use of nano-silica to increase early strength and reduce setting time of concretes with high volumes of slag," *Cem. Concr. Compos.*, vol. 34, pp. 650–662, 2012.
- [132] G. Land and D. Stephan, "Controlling cement hydration with nanoparticles," *Cem. Concr. Compos.*, vol. 57, pp. 64–67, 2015.
- [133] K. Sobolev, I. Flores, R. Hermosillo, and L. M. Torres-Martínez, "Nanomaterials and nanotechnology for high-performance cement composites," American Concrete Institute, ACI Special Publication, pp. 93–120, 2008.
- [134] M. Amin and K. Abu El-Hassan, "Effect of using different types of nano materials on mechanical properties of high strength concrete," *Constr. Build. Mater.*, vol. 80, pp. 116–124, 2015.
- [135] J. I. Tobón, J. Payá, and O. J. Restrepo, "Study of durability of Portland cement mortars blended with silica nanoparticles," *Constr. Build. Mater.*, vol. 80, pp. 92–97, 2015.
- [136] D. Kong, D. J. Corr, P. Hou, Y. Yang, and S. P. Shah, "Influence of colloidal silica sol on fresh properties of cement paste as compared to nano-silica powder with agglomerates in micron-scale," *Cem. Concr. Compos.*, vol. 63, pp. 30–41, 2015.
- [137] A. Hanif, P. Parthasarathy, H. Ma, T. Fan, and Z. Li, "Properties improvement of fly ash cenosphere modified cement pastes using nano silica," *Cem. Concr. Compos.*, vol. 81, pp. 35–48, 2017.

- [138] H. S. Lee, B. Balasubramanian, G. V. T. Gopalakrishna, S. J. Kwon, S. P. Karthick, and V. Saraswathy, “Durability performance of CNT and nanosilica admixed cement mortar,” *Constr. Build. Mater.*, vol. 159, pp. 463–472, 2018.
- [139] C. Nunes, Z. Slížková, M. Stefanidou, and J. Němeček, “Microstructure of lime and lime-pozzolana pastes with nanosilica,” *Cem. Concr. Res.*, vol. 83, pp. 152–163, 2016.
- [140] G. Quercia, G. Hüsken, and H. J. H. Brouwers, “Water demand of amorphous nano silica and its impact on the workability of cement paste,” *Cem. Concr. Res.*, vol. 42, pp. 344–357, 2012.
- [141] A. M. Kaja and Q. L. Yu, “Method for the manufacture of high-end performance steel slag-based building products,” U.S. Provisional Pat. Ser. No. 62/821603, filed 3/21/2019.
- [142] A. Lazaro, H. J. H. Brouwers, G. Quercia, and J. W. Geus, “The properties of amorphous nano-silica synthesized by the dissolution of olivine,” *Chem. Eng. J.*, vol. 211–212, pp. 112–121, 2012.
- [143] A. Lázaro García, Nano-silica production at low temperatures from the dissolution of olivine, PhD Thesis. Eindhoven University of Technology, 2014.
- [144] G. Quercia Bianchi, Application of nano-silica in concrete, PhD Thesis. Eindhoven University of Technology, 2014.
- [145] K. Scrivener, R. Snellings, and B. Lothenbach, *A Practical Guide to Microstructural Analysis of Cementitious Materials*. 2018.
- [146] E. Prince, Ed., *International Tables for Crystallography*, Third edition., vol. C. International Union of Crystallography, 2006.
- [147] C. Hesse, F. Goetz-Neunhoeffler, and J. Neubauer, “A new approach in quantitative in-situ XRD of cement pastes: Correlation of heat flow curves with early hydration reactions,” *Cem. Concr. Res.*, vol. 41, pp. 123–128, 2011.
- [148] D. Ectors, J. Neubauer, and F. Goetz-Neunhoeffler, “The hydration of synthetic brownmillerite in presence of low Ca-sulfate content and calcite monitored by quantitative in-situ-XRD and heat flow calorimetry,” *Cem. Concr. Res.*, vol. 54, pp. 61–68, 2013.
- [149] T. Hertel, J. Neubauer, and F. Goetz-Neunhoeffler, “Study of hydration potential and kinetics of the ferrite phase in iron-rich CAC,” *Cem. Concr. Res.*, vol. 83, pp. 79–85, 2016.
- [150] D. E. Rogers and L. P. Aldridge, “Hydrates of calcium ferrites and calcium aluminoferrites,” *Cem. Concr. Res.*, vol. 7, pp. 399–409, 1977.
- [151] J. M. Fortune and J. M. D. Coey, “Hydration products of calcium aluminoferrite,” *Cem. Concr. Res.*, vol. 13, pp. 696–702, 1983.
- [152] H. F. W. Taylor, *Cement Chemistry*, Second edition. London: Thomas Telford, 1997.
- [153] E. Aleshin, Ed., *Proceedings of the Mineral Waste Utilization Symposium*. Chicago, Illinois: IITRI, 1976.
- [154] B. Lothenbach, D. A. Kulik, T. Matschei, M. Balonis, L. Baquerizo, B. Dilnesa, G. D.

- Miron, R. J. Myers, "Cemdata18: A chemical thermodynamic database for hydrated Portland cements and alkali-activated materials," *Cem. Concr. Res.*, vol. 115, pp. 472–506, 2019.
- [155] H. Madani, A. Bagheri, and T. Parhizkar, "The pozzolanic reactivity of monodispersed nanosilica hydrosols and their influence on the hydration characteristics of Portland cement," *Cem. Concr. Res.*, vol. 42, pp. 1563–1570, 2012.
- [156] A. V. Soin, L. J. J. Catalan, and S. D. Kinrade, "A combined QXRD/TG method to quantify the phase composition of hydrated Portland cements," *Cem. Concr. Res.*, vol. 48, pp. 17–24, 2013.
- [157] Y. Wei, W. Yao, X. Xing, and M. Wu, "Quantitative evaluation of hydrated cement modified by silica fume using QXRD, ²⁷Al MAS NMR, TG-DSC and selective dissolution techniques," *Constr. Build. Mater.*, vol. 36, pp. 925–932, 2012.
- [158] A. M. Kaja, A. Lazaro, and Q. L. Yu, "Effects of Portland cement on activation mechanism of class F fly ash geopolymer cured under ambient conditions," *Constr. Build. Mater.*, vol. 189, pp. 1113–1123, 2018.
- [159] A.M. Kaja, A. Delsing, H. J. H. Brouwers, and Q. L. Yu, "Effects of carbonation on the retention of heavy metals in chemically activated BOF slag pastes," Manuscript in preparation.
- [160] A. M. Kaja, K. Schollbach, S. Melzer, S. R. van der Laan, H. J. H. Brouwers, and Q. Yu, "Hydration of potassium citrate-activated BOF slag," *Cem. Concr. Res.*, vol. 140, p. 106291, 2021.
- [161] X. Gao, Q. L. Yu, and H. J. H. Brouwers, "Properties of alkali activated slag-fly ash blends with limestone addition," *Cem. Concr. Compos.*, vol. 59, pp. 119–128, 2015.
- [162] Q. Zhao, C. Liu, L. Cao, X. Zheng, and M. Jiang, "Effect of lime on stability of chromium in stainless steel slag," *Minerals*, vol. 8, pp. 1–10, 2018.
- [163] P. Chaurand, J. Rose, V. Briois, L. Olivi, J. Hazemann, O. Proux, J. Domas, and J. Bottero, "Environmental impacts of steel slag reused in road construction: A crystallographic and molecular (XANES) approach," *J. Hazard. Mater.*, vol. 139, pp. 537–542, 2007.
- [164] J. F. P. Gomes and C. G. Pinto, "Leaching of heavy metals from steelmaking slags," *Rev. Metal.*, vol. 42, 2006.
- [165] U. V. Oty, "Steel slag leachates: environmental risks and metal recovery opportunities," University of Hull, 2015.
- [166] P. Chaurand, J. Rose, J. Domas, and J. Y. Bottero, "Speciation of Cr and V within BOF steel slag reused in road constructions," *J. Geochemical Explor.*, vol. 88, no. SPEC. ISS., pp. 10–14, 2006.
- [167] G. Costa, A. Poletini, R. Pomi, and A. Stramazzo, "Leaching modelling of slurry-phase carbonated steel slag," *J. Hazard. Mater.*, vol. 302, pp. 415–425, 2016.
- [168] H. Preßlinger and K. O. Klepp, "Vanadium in converter slags," *Steel Res.*, vol. 73, pp. 522–525, 2002.

- [169] A. J. Hobson, D. I. Stewart, A. W. Bray, R. J. G. Mortimer, W. M. Mayes, M. Rogerson, and I. T. Burke, "Mechanism of Vanadium Leaching during Surface Weathering of Basic Oxygen Furnace Steel Slag Blocks: A Microfocus X-ray Absorption Spectroscopy and Electron Microscopy Study," *Environ. Sci. Technol.*, vol. 51, pp. 7823–7830, 2017.
- [170] M. L. D. Gougar, B. E. Scheetz, and D. M. Roy, "Ettringite and C-S-H portland cement phases for waste ion immobilization: A review," *Waste Manag.*, vol. 16, pp. 295–303, 1996.
- [171] O. E. Omotoso, D. G. Ivey, and R. Mikula, "Characterization of chromium doped tricalcium silicate using SEM/EDS, XRD and FTIR," *J. Hazard. Mater.*, vol. 42, pp. 87–102, 1995.
- [172] M. Castellote, L. Fernandez, C. Andrade, and C. Alonso, "Chemical changes and phase analysis of OPC pastes carbonated at different CO₂ concentrations," *Mater. Struct. Constr.*, vol. 42, pp. 515–525, 2009.
- [173] T. F. Sevelsted and J. Skibsted, "Carbonation of C-S-H and C-A-S-H samples studied by ¹³C, ²⁷Al and ²⁹Si MAS NMR spectroscopy," *Cem. Concr. Res.*, vol. 71, pp. 56–65, 2015.
- [174] K. De Weerd, G. Plusquellec, A. Belda Revert, M. R. Geiker, and B. Lothenbach, "Effect of carbonation on the pore solution of mortar," *Cem. Concr. Res.*, vol. 118, pp. 38–56, 2019.
- [175] Y. Zuo, M. Nedeljković, and G. Ye, "Pore solution composition of alkali-activated slag/fly ash pastes," *Cem. Concr. Res.*, vol. 115, pp. 230–250, 2019.
- [176] "EA NEN 7375:2004 - Leaching characteristics of moulded or monolithic building and waste materials," 2005.
- [177] D. Laerke Baun, J. Holm, J. B. Hansen, and M. Wahlström, "CEN EN 12457 leaching test," 2003.
- [178] M. Auroy, S. Poyet, P. Le Bescop, J. Torrenti, T. Charpentier, M. Moskura, and X. Bourbon, "Comparison between natural and accelerated carbonation (3% CO₂): Impact on mineralogy, microstructure, water retention and cracking," *Cem. Concr. Res.*, vol. 109, pp. 64–80, 2018.
- [179] F. Caruso, S. Mantellato, M. Palacios, and R. J. Flatt, "ICP-OES method for the characterization of cement pore solutions and their modification by polycarboxylate-based superplasticizers," *Cem. Concr. Res.*, vol. 91, pp. 52–60, 2017.
- [180] M. Spanka, T. Mansfeldt, and R. Bialucha, "Sequential extraction of chromium, molybdenum, and vanadium in basic oxygen furnace slags," *Environ. Sci. Pollut. Res.*, vol. 25, pp. 23082–23090, 2018.
- [181] A. J. Hobson, D. I. Stewart, R. J. G. Mortimer, W. M. Mayes, M. Rogerson, and I. T. Burke, "Leaching behaviour of co-disposed steel making wastes : Effects of aeration on leachate chemistry and vanadium mobilisation," *Waste Manag.*, vol. 81, pp. 1–10, 2018.
- [182] A. Morandau, M. Thiéry, and P. Dangla, "Cement and Concrete Research Impact

- of accelerated carbonation on OPC cement paste blended with fly ash,” *Cem. Concr. Res.*, vol. 67, pp. 226–236, 2015.
- [183] V. Shah, K. Scrivener, B. Bhattacharjee, and S. Bishnoi, “Changes in microstructure characteristics of cement paste on carbonation,” *Cem. Concr. Res.*, vol. 109, pp. 184–197, 2018.
- [184] Z. Shi, B. Lothenbach, M. R. Geiker, J. Kaufmann, A. Leemann, S. Ferreiro, and J. Skibsted, “Experimental studies and thermodynamic modeling of the carbonation of Portland cement, metakaolin and limestone mortars,” *Cem. Concr. Res.*, vol. 88, pp. 60–72, 2016.
- [185] H. Justnes, J. Skocek, T. A. Østnor, C. J. Engelsen, and O. Skjølvold, “Microstructural changes of hydrated cement blended with fly ash upon carbonation,” *Cem. Concr. Res.*, vol. 137, p. 106192, 2020.
- [186] M. Nedeljković, B. Ghiassi, S. van der Laan, Z. Li, and G. Ye, “Effect of curing conditions on the pore solution and carbonation resistance of alkali-activated fly ash and slag pastes,” *Cem. Concr. Res.*, vol. 116, pp. 146–158, 2019.
- [187] A. M. Kaja, H. J. H. Brouwers, and Q. L. Yu, “NO_x degradation by photocatalytic mortars: The underlying role of the CH and C-S-H carbonation,” *Cem. Concr. Res.*, vol. 125, 2019.
- [188] A. Morandea, M. Thiéry, and P. Dangla, “Impact of accelerated carbonation on OPC cement paste blended with fly ash,” *Cem. Concr. Res.*, vol. 67, pp. 226–236, 2015.
- [189] W. J. J. Huijgen, “Carbonation of Steel Slag for CO₂ Sequestration: Leaching of Products and Reaction Mechanisms,” vol. 40, pp. 2790–2796, 2006.
- [190] R. Baciocchi, G. Costa, A. Poletti, and R. Pomi, “Effects of thin-film accelerated carbonation on steel slag leaching,” *J. Hazard. Mater.*, vol. 286, pp. 369–378, 2015.
- [191] A. Fujishima, X. Zhang, and D. A. Tryk, “Heterogeneous photocatalysis: From water photolysis to applications in environmental cleanup,” *Int. J. Hydrogen Energy*, vol. 32, pp. 2664–2672, 2007.
- [192] Q. L. Yu and H. J. H. Brouwers, “Indoor air purification using heterogeneous photocatalytic oxidation. Part I: Experimental study,” *Appl. Catal. B Environ.*, vol. 92, pp. 454–461, 2009.
- [193] M. Hunger, G. Hüsken, and H. J. H. Brouwers, “Photocatalytic degradation of air pollutants — From modeling to large scale application,” *Cem. Concr. Res.*, vol. 40, pp. 313–320, 2010.
- [194] C. S. Poon and E. Cheung, “NO removal efficiency of photocatalytic paving blocks prepared with recycled materials,” *Constr. Build. Mater.*, vol. 21, pp. 1746–1753, 2007.
- [195] J. Araña, D. Garzón Sousa, O. González Díaz, E. Pulido Melián, and J. M. Doña Rodríguez, “Effect of NO₂ and NO₃⁻/HNO₃ adsorption on no photocatalytic conversion,” *Appl. Catal. B Environ.*, vol. 244, pp. 660–670, 2019.
- [196] E. Jimenez-Relinque and J. R. Rodriguez-Garcia, “Characteristics and efficiency of photocatalytic cementitious materials: Type of binder, roughness and microstructure,”

- Cem. Concr. Res., vol. 71, pp. 124–131, 2015.
- [197] M. Pérez-Nicolás, J. Balbuena, M. Cruz-Yusta, L. Sanchez, I. Navarro-Blasco, J. M. Fernandez, J. I. Alvarez, “Photocatalytic NO_x abatement by calcium aluminate cements modified with TiO₂: Improved NO₂ conversion,” *Cem. Concr. Res.*, vol. 70, pp. 67–76, 2015.
- [198] F. Gauvin, V. Caprai, Q. L. Yu, and H. J. H. Brouwers, “Effect of the morphology and pore structure of porous building materials on photocatalytic oxidation of air pollutants,” *Appl. Catal. B Environ.*, vol. 227, pp. 123–131, 2018.
- [199] M. Lackhoff, X. Prieto, N. Nestle, F. Dehn, and R. Niessner, “Photocatalytic activity of semiconductor-modified cement - Influence of semiconductor type and cement ageing,” *Appl. Catal. B Environ.*, vol. 43, pp. 205–216, 2003.
- [200] M. V. Diamanti, F. Lollini, M. P. Pedferri, and L. Bertolini, “Mutual interactions between carbonation and titanium dioxide photoactivity in concrete,” *Build. Environ.*, vol. 62, pp. 174–181, 2013.
- [201] M. Serdar, S. Poyet, V. L. Hostis, and D. Bjegovi, “Carbonation of low-alkalinity mortars : Influence on corrosion of steel and on mortar microstructure,” *Cem. Concr. Res.*, vol. 101, pp. 33–45, 2017.
- [202] F. P. Glasser and T. Matschei, *Interactions Between Portland Cement and Carbon Dioxide*. ICCI, 2007.
- [203] A. Morandea, M. Thiéry, and P. Dangla, “Investigation of the carbonation mechanism of CH and C-S-H in terms of kinetics, microstructure changes and moisture properties,” *Cem. Concr. Res.*, vol. 56, pp. 153–170, 2014.
- [204] S. S. Lucas, V. M. Ferreira, and J. L. B. De Aguiar, “Incorporation of titanium dioxide nanoparticles in mortars - Influence of microstructure in the hardened state properties and photocatalytic activity,” *Cem. Concr. Res.*, vol. 43, pp. 112–120, 2013.
- [205] R. Sugrañez, J. I. Alvarez, M. Cruz-Yusta, I. Marmol, J. Morales, J. Vila, and L. Sanchez, “Enhanced photocatalytic degradation of NO_x gases by regulating the microstructure of mortar cement modified with titanium dioxide,” *Build. Environ.*, vol. 69, pp. 55–63, 2013.
- [206] J. Z. Bloh, A. Folli, and D. E. Macphee, “Photocatalytic NO_x abatement : why the selectivity matters,” *RSC Adv.*, vol. 4, pp. 45726–45734, 2014.
- [207] L. Yang, A. Hakki, F. Wang, and D. E. Macphee, “Different Roles of Water in Photocatalytic DeNO_x Mechanisms on TiO₂: Basis for Engineering Nitrate Selectivity?,” *Appl. Mater. interfaces*, 2017.
- [208] J. Kou, C. Lu, J. Wang, Y. Chen, Z. Xu, and R. S. Varma, “Selectivity Enhancement in Heterogeneous Photocatalytic Transformations,” *Chem. Rev.*, vol. 117, pp. 1445–1514, 2017.
- [209] L. Yang, A. Hakki, L. Zheng, M. R. Jones, F. Wang, and D. E. Macphee, “Photocatalytic concrete for NO_x abatement: Supported TiO₂ efficiencies and impacts,” *Cem. Concr. Res.*, vol. 116, pp. 57–64, 2019.
- [210] M. Horgnies, I. Dubois-Brugger, and E. M. Gartner, “NO_x de-pollution by hardened

- concrete and the influence of activated charcoal additions,” *Cem. Concr. Res.*, vol. 42, pp. 1348–1355, 2012.
- [211] L. Yang, A. Hakki, F. Wang, and D. E. Macphee, “Photocatalyst efficiencies in concrete technology: The effect of photocatalyst placement,” *Appl. Catal. B Environ.*, vol. 222, pp. 200–208, 2018.
- [212] X. Zhang, H. Tong, H. Zhang, and C. Chen, “Nitrogen oxides absorption on calcium hydroxide at low temperature,” *Ind. Eng. Chem. Res.*, vol. 47, pp. 3827–3833, 2008.
- [213] N. J. Krou, I. Batonneau-Gener, T. Belin, S. Mignard, M. Horgnies, and I. Dubois-Brugger, “Mechanisms of NO_x entrapment into hydrated cement paste containing activated carbon - Influences of the temperature and carbonation,” *Cem. Concr. Res.*, vol. 53, pp. 51–58, 2013.
- [214] C. H. Nelli and G. T. Rochelle, “Nitrogen Dioxide Reaction with Alkaline Solids,” *Ind. Eng. Chem. Res.*, vol. 35, pp. 999–1005, 1996.
- [215] Y. Hendrix, A. Lazaro, Q. L. Yu, and H. J. H. Brouwers, “Influence of synthesis conditions on the properties of photocatalytic titania-silica composites,” *J. Photochem. Photobiol. A Chem.*, vol. 371, pp. 25–32, 2019.
- [216] X. Gao, S. R. Bare, J. L. G. Fierro, M. A. Banares, and I. E. Wachs, “Preparation and in-Situ Spectroscopic Characterization of Molecularly Dispersed Titanium Oxide on Silica,” *J. Phys. Chem. B*, vol. 102, pp. 5653–5666, 1998.
- [217] Y. Hendrix, A. Lazaro, Q. Yu, and H.J.H. Brouwers, “Titania-Silica Composites: A Review on the Photocatalytic Activity and Synthesis Methods,” *World J. Nano Sci. Eng.*, vol. 05, pp. 161–177, 2015.
- [218] V. S. Smitha, K. A. Manjumol, K. V. Baiju, S. Ghosh, P. Perumal, and K. G. K. Warriar, “Sol-gel route to synthesize titania-silica nano precursors for photoactive particulates and coatings,” *J. Sol-Gel Sci. Technol.*, vol. 54, pp. 203–211, 2010.
- [219] X. Zhang, F. Zhang, and K.-Y. Chan, “Synthesis of titania–silica mixed oxide mesoporous materials, characterization and photocatalytic properties,” *Appl. Catal. A Gen.*, vol. 284, pp. 193–198, 2005.
- [220] M. Montes, F. P. Getton, M. S. W. Vong, and P. Sermon, “Titania on silica. A comparison of sol-gel routes and traditional methods,” *J. Sol-Gel Sci. Technol.*, vol. 8, pp. 131–137, 1997.
- [221] D. E. Macphee and A. Folli, “Photocatalytic concretes — The interface between photocatalysis and cement chemistry,” *Cem. Concr. Res.*, vol. 85, pp. 48–54, 2016.
- [222] M. Thiery, G. Villain, P. Dangla, and G. Platret, “Investigation of the carbonation front shape on cementitious materials: Effects of the chemical kinetics,” *Cem. Concr. Res.*, vol. 37, pp. 1047–1058, 2007.
- [223] W. F. Cole and B. Kroone, “Carbonate Minerals in Hydrated Portland Cement,” *Nature*, vol. 7, p. 4688, 1959.
- [224] P. H. R. Borges, J. O. Costa, N. B. Milestone, C. J. Lynsdale, and R. E. Streatfield, “Carbonation of CH and C-S-H in composite cement pastes containing high amounts of BFS,” *Cem. Concr. Res.*, vol. 40, pp. 284–292, 2010.

- [225] Z. Šauman, “Carbonization of porous concrete and its main binding components,” *Cem. Concr. Res.*, vol. 1, pp. 645–662, 1971.
- [226] E. T. Stepkowska, J. M. Blanes, F. Franco, C. Real, and J. L. Pérez-Rodríguez, “Phase transformation on heating of an aged cement paste,” *Thermochim. Acta*, vol. 420, no. SPEC. ISS., pp. 79–87, 2004.
- [227] V. Shah, K. Scrivener, B. Bhattacharjee, and S. Bishnoi, “Changes in microstructure characteristics of cement paste on carbonation,” *Cem. Concr. Res.*, vol. 109, pp. 184–197, 2018.
- [228] J. J. Chen, J. J. Thomas, and H. M. Jennings, “Decalcification shrinkage of cement paste,” *Cem. Concr. Res.*, vol. 36, pp. 801–809, 2006.
- [229] A. Hakki, L. Yang, F. Wang, and D. E. Macphee, “The Effect of Interfacial Chemical Bonding in $\text{TiO}_2\text{-SiO}_2$ Composites on Their Photocatalytic NO_x Abatement Performance,” *J. Vis. Exp.*, no. 125, pp. 1–11, 2017.
- [230] B. Weinberger, D. L. Laskin, D. E. Heck, and J. D. Laskin, “The toxicology of inhaled nitric oxide,” *Toxicol. Sci.*, vol. 59, pp. 5–16, 2001.
- [231] R. Dillert, A. Engel, J. Große, P. Lindner, and D. W. Bahnemann, “Light intensity dependence of the kinetics of the photocatalytic oxidation of nitrogen(II) oxide at the surface of TiO_2 ,” *Phys. Chem. Chem. Phys.*, vol. 15, pp. 20876–20886, 2013.
- [232] M. M. Ballari, Q. L. Yu, and H. J. H. Brouwers, “Experimental study of the NO and NO_2 degradation by photocatalytically active concrete,” *Catal. Today*, vol. 161, pp. 175–180, 2011.
- [233] J. J. Thomas, J. J. Chen, A. J. Allen, and H. M. Jennings, “Effects of decalcification on the microstructure and surface area of cement and tricalcium silicate pastes,” *Cem. Concr. Res.*, vol. 34, pp. 2297–2307, 2004.
- [234] G. Hüsken, M. Hunger, and H. J. H. Brouwers, “Experimental study of photocatalytic concrete products for air purification,” *Build. Environ.*, vol. 44, pp. 2463–2474, 2009.
- [235] S. T. Pham and W. Prince, “Effects of Carbonation on the Microstructure of Cement Materials: Influence of Measuring Methods and of Types of Cement,” *Int. J. Concr. Struct. Mater.*, vol. 8, pp. 327–333, 2014.

List of publications

Peer-Reviewed Journal Publications

1. Kaja, A. M., Lazaro, A., & Yu, Q. L. (2018). Effects of Portland cement on activation mechanism of class F fly ash geopolymer cured under ambient conditions. *Construction and Building Materials*, 189, 1113–1123.
2. Kaja, A. M., Brouwers, H. J. H., & Yu, Q. L. (2019). NO_x degradation by photocatalytic mortars: The underlying role of the CH and C-S-H carbonation. *Cement and Concrete Research*, 125, 105805.
3. Kaja, A. M., Schollbach, K., Melzer, S., van der Laan, S. R., Brouwers, H. J. H., & Yu, Q. L. (2021). Hydration of potassium citrate-activated BOF slag. *Cement and Concrete Research*, 140, 106291.
4. Kaja, A. M., Melzer, S., Brouwers, H. J. H., & Yu, Q. L. On the optimization of BOF slag hydration kinetics. *Submitted to Cement and Concrete Composites, revised.*
5. Kaja, A. M., Delsing, A., van der Laan, S. R., Brouwers, H. J. H., & Yu, Q. L. Effects of carbonation on the retention of heavy metals in chemically activated BOF slag pastes. *Submitted.*

Patent Applications

1. Kaja, A. M., & Yu, Q. L. Method for the manufacture of high-end performance steel slag-based building products. WO 2020/188070 A1. Published 24/09/2020.

Conference Proceedings

1. Kaja, A. M., Brouwers, H. J. H., & Yu, Q. L. Ambient cured fly ash geopolymers, The 6th International Conference of Non-Traditional Cement and Concrete, 19-22 July 2017, Brno, Czech Republic.
2. Kaja, A. M., Brouwers, H. J. H., & Yu, Q. L. Effect of cement addition on the geopolymerisation process, The 9th International Symposium of Cement and Concrete, 31 October- 3 November 2017, Wuhan, China.

3. Kaja, A. M., Brouwers, H. J. H., & Yu, Q. L. Durability of photocatalytic mortars, The 2nd International Conference on Sustainable Building Materials, 12-15 August 2019, Eindhoven, The Netherlands.

Curriculum Vitae

Anna Kaja was born on the 30th of September 1992 in Limanowa, Poland. She obtained her Bachelor's degree in Chemical Technology at the AGH University of Science and Technology, Cracow, in 2015. During her Bachelor's study, she worked on the low-friction coatings on the moving parts of the hip joint. Directly after receiving her Bachelor's degree, she enrolled in the Chemical Technology Master program at AGH. In 2016 she graduated cum laude with the Master thesis: “A study on the pozzolanic reaction in a ternary system of synthetic aluminosilicate glass, limestone and alkali,” supervised by Prof. Jan Deja. After her Master's study, Anna moved to the Netherlands to pursue her PhD at the Eindhoven University of Technology in the Building Materials group. She worked on the NWO project titled “Tailoring new nano-silica, and its application in smart concrete” under the supervision of Prof. H.J.H. Brouwers and Prof. Q.L. Yu. The results of the project are presented in this thesis.

Bouwstenen is een publicatiereeks van de Faculteit Bouwkunde, Technische Universiteit Eindhoven. Zij presenteert resultaten van onderzoek en andere activiteiten op het vakgebied der Bouwkunde, uitgevoerd in het kader van deze Faculteit.

Bouwstenen en andere proefschriften van de TU/e zijn online beschikbaar via:
<https://research.tue.nl/>

Reeds verschenen in de serie
Bouwstenen

nr 1

Elan: A Computer Model for Building Energy Design: Theory and Validation

Martin H. de Wit

H.H. Driessen

R.M.M. van der Velden

nr 2

Kwaliteit, Keuzevrijheid en Kosten: Evaluatie van Experiment Klarendal, Arnhem

J. Smeets

C. le Nobel

M. Broos

J. Frenken

A. v.d. Sanden

nr 3

Crooswijk: Van 'Bijzonder' naar 'Gewoon'

Vincent Smit

Kees Noort

nr 4

Staal in de Woningbouw

Edwin J.F. Delsing

nr 5

Mathematical Theory of Stressed Skin Action in Profiled Sheeting with Various Edge Conditions

Andre W.A.M.J. van den Bogaard

nr 6

Hoe Berekenbaar en Betrouwbaar is de Coëfficiënt k in x -ksigma en x -ks?

K.B. Lub

A.J. Bosch

nr 7

Het Typologisch Gereedschap: Een Verkennende Studie Omtrent Typologie en Omtrent de Aanpak van Typologisch Onderzoek

J.H. Luiten

nr 8

Informatievoorziening en Beheerprocessen

A. Nauta

Jos Smeets (red.)

Helga Fassbinder (projectleider)

Adrie Proveniers

J. v.d. Moosdijk

nr 9

Strukturering en Verwerking van Tijdgegevens voor de Uitvoering van Bouwwerken

ir. W.F. Schaefer

P.A. Erkelens

nr 10

Stedebouw en de Vorming van een Speciale Wetenschap

K. Doevendans

nr 11

Informatica en Ondersteuning van Ruimtelijke Besluitvorming

G.G. van der Meulen

nr 12

Staal in de Woningbouw, Korrosie-Bescherming van de Begane Grondvloer

Edwin J.F. Delsing

nr 13

Een Thermisch Model voor de Berekening van Staalplaatbetonvloeren onder Brandomstandigheden

A.F. Hamerlinck

nr 14

De Wijkgedachte in Nederland: Gemeenschapsstreven in een Stedebouwkundige Context

K. Doevendans

R. Stolzenburg

nr 15

Diaphragm Effect of Trapezoidally Profiled Steel Sheets:

Experimental Research into the Influence of Force Application

Andre W.A.M.J. van den Bogaard

nr 16

Versterken met Spuit-Ferrocement: Het Mechanische Gedrag van met Spuit-Ferrocement Versterkte Gewapend Betonbalken

K.B. Lubir

M.C.G. van Wanroy

- nr 17
**De Tractaten van
Jean Nicolas Louis Durand**
G. van Zeyl
- nr 18
**Wonen onder een Plat Dak:
Drie Opstellen over Enkele
Vooronderstellingen van de
Stedebouw**
K. Doevendans
- nr 19
**Supporting Decision Making Processes:
A Graphical and Interactive Analysis of
Multivariate Data**
W. Adams
- nr 20
**Self-Help Building Productivity:
A Method for Improving House Building
by Low-Income Groups Applied to Kenya
1990-2000**
P. A. Erkelens
- nr 21
**De Verdeling van Woningen:
Een Kwestie van Onderhandelen**
Vincent Smit
- nr 22
**Flexibiliteit en Kosten in het
Ontwerpproces:
Een Besluitvormingondersteunend Model**
M. Prins
- nr 23
**Spontane Nederzettingen Begeleid:
Voorwaarden en Criteria in Sri Lanka**
Po Hin Thung
- nr 24
**Fundamentals of the Design of
Bamboo Structures**
Oscar Arce-Villalobos
- nr 25
Concepten van de Bouwkunde
M.F.Th. Bax (red.)
H.M.G.J. Trum (red.)
- nr 26
Meaning of the Site
Xiaodong Li
- nr 27
**Het Woonmilieu op Begrip Gebracht:
Een Speurtocht naar de Betekenis van het
Begrip 'Woonmilieu'**
Jaap Ketelaar
- nr 28
Urban Environment in Developing Countries
editors: Peter A. Erkelens
George G. van der Meulen (red.)
- nr 29
**Stategische Plannen voor de Stad:
Onderzoek en Planning in Drie Steden**
prof.dr. H. Fassbinder (red.)
H. Rikhof (red.)
- nr 30
Stedebouwkunde en Stadsbestuur
Piet Beekman
- nr 31
**De Architectuur van Djenné:
Een Onderzoek naar de Historische Stad**
P.C.M. Maas
- nr 32
Conjoint Experiments and Retail Planning
Harmen Oppewal
- nr 33
**Strukturformen Indonesischer Bautechnik:
Entwicklung Methodischer Grundlagen
für eine 'Konstruktive Pattern Language'
in Indonesien**
Heinz Frick arch. SIA
- nr 34
**Styles of Architectural Designing:
Empirical Research on Working Styles
and Personality Dispositions**
Anton P.M. van Bakel
- nr 35
**Conjoint Choice Models for Urban
Tourism Planning and Marketing**
Benedict Dellaert
- nr 36
Stedelijke Planvorming als Co-Productie
Helga Fassbinder (red.)

- nr 37
Design Research in the Netherlands
editors: R.M. Oxman
M.F.Th. Bax
H.H. Achten
- nr 38
Communication in the Building Industry
Bauke de Vries
- nr 39
**Optimaal Dimensioneren van
Gelaste Plaatliggers**
J.B.W. Stark
F. van Pelt
L.F.M. van Gorp
B.W.E.M. van Hove
- nr 40
Huisvesting en Overwinning van Armoede
P.H. Thung
P. Beekman (red.)
- nr 41
**Urban Habitat:
The Environment of Tomorrow**
George G. van der Meulen
Peter A. Erkelens
- nr 42
A Typology of Joints
John C.M. Olie
- nr 43
**Modeling Constraints-Based Choices
for Leisure Mobility Planning**
Marcus P. Stemerding
- nr 44
Activity-Based Travel Demand Modeling
Dick Ettema
- nr 45
**Wind-Induced Pressure Fluctuations
on Building Facades**
Chris Geurts
- nr 46
Generic Representations
Henri Achten
- nr 47
**Johann Santini Aichel:
Architectuur en Ambiguiteit**
Dirk De Meyer
- nr 48
**Concrete Behaviour in Multiaxial
Compression**
Erik van Geel
- nr 49
Modelling Site Selection
Frank Witlox
- nr 50
Ecolemma Model
Ferdinand Beetstra
- nr 51
**Conjoint Approaches to Developing
Activity-Based Models**
Donggen Wang
- nr 52
On the Effectiveness of Ventilation
Ad Roos
- nr 53
**Conjoint Modeling Approaches for
Residential Group preferences**
Eric Molin
- nr 54
**Modelling Architectural Design
Information by Features**
Jos van Leeuwen
- nr 55
**A Spatial Decision Support System for
the Planning of Retail and Service Facilities**
Theo Arentze
- nr 56
Integrated Lighting System Assistant
Ellie de Groot
- nr 57
Ontwerpend Leren, Leren Ontwerpen
J.T. Boekholt
- nr 58
**Temporal Aspects of Theme Park Choice
Behavior**
Astrid Kemperman
- nr 59
**Ontwerp van een Geïndustrialiseerde
Funderingswijze**
Faas Moonen

nr 60

**Merlin: A Decision Support System
for Outdoor Leisure Planning**

Manon van Middelkoop

nr 61

The Aura of Modernity

Jos Bosman

nr 62

Urban Form and Activity-Travel Patterns

Daniëlle Snellen

nr 63

Design Research in the Netherlands 2000

Henri Achten

nr 64

**Computer Aided Dimensional Control in
Building Construction**

Rui Wu

nr 65

Beyond Sustainable Building

editors: Peter A. Erkelens

Sander de Jonge

August A.M. van Vliet

co-editor: Ruth J.G. Verhagen

nr 66

Das Globalrecyclingfähige Haus

Hans Löfflad

nr 67

Cool Schools for Hot Suburbs

René J. Dierkx

nr 68

**A Bamboo Building Design Decision
Support Tool**

Fitri Mardjono

nr 69

Driving Rain on Building Envelopes

Fabien van Mook

nr 70

Heating Monumental Churches

Henk Schellen

nr 71

**Van Woningverhuurder naar
Aanbieder van Woongenot**

Patrick Dogge

nr 72

**Moisture Transfer Properties of
Coated Gypsum**

Emile Goossens

nr 73

Plybamboo Wall-Panels for Housing

Guillermo E. González-Beltrán

nr 74

The Future Site-Proceedings

Ger Maas

Frans van Gassel

nr 75

**Radon transport in
Autoclaved Aerated Concrete**

Michel van der Pal

nr 76

**The Reliability and Validity of Interactive
Virtual Reality Computer Experiments**

Amy Tan

nr 77

**Measuring Housing Preferences Using
Virtual Reality and Belief Networks**

Maciej A. Orzechowski

nr 78

**Computational Representations of Words
and Associations in Architectural Design**

Nicole Segers

nr 79

**Measuring and Predicting Adaptation in
Multidimensional Activity-Travel Patterns**

Chang-Hyeon Joh

nr 80

Strategic Briefing

Fayez Al Hassan

nr 81

Well Being in Hospitals

Simona Di Cicco

nr 82

**Solares Bauen:
Implementierungs- und Umsetzungs-
Aspekte in der Hochschulausbildung
in Österreich**

Gerhard Schuster

- nr 83
Supporting Strategic Design of Workplace Environments with Case-Based Reasoning
Shauna Mallory-Hill
- nr 84
ACCEL: A Tool for Supporting Concept Generation in the Early Design Phase
Maxim Ivashkov
- nr 85
Brick-Mortar Interaction in Masonry under Compression
Ad Vermeltfoort
- nr 86
Zelfredzaam Wonen
Guus van Vliet
- nr 87
Een Ensemble met Grootstedelijke Allure
Jos Bosman
Hans Schippers
- nr 88
On the Computation of Well-Structured Graphic Representations in Architectural Design
Henri Achten
- nr 89
De Evolutie van een West-Afrikaanse Vernaculaire Architectuur
Wolf Schijns
- nr 90
ROMBO Tactiek
Christoph Maria Ravesloot
- nr 91
External Coupling between Building Energy Simulation and Computational Fluid Dynamics
Ery Djunaedy
- nr 92
Design Research in the Netherlands 2005
editors: Henri Achten
Kees Dorst
Pieter Jan Stappers
Bauke de Vries
- nr 93
Ein Modell zur Baulichen Transformation
Jalil H. Saber Zaimian
- nr 94
Human Lighting Demands: Healthy Lighting in an Office Environment
Myriam Aries
- nr 95
A Spatial Decision Support System for the Provision and Monitoring of Urban Greenspace
Claudia Pelizaro
- nr 96
Leren Creëren
Adri Proveniers
- nr 97
Simlandscape
Rob de Waard
- nr 98
Design Team Communication
Ad den Otter
- nr 99
Humaan-Ecologisch Georiënteerde Woningbouw
Juri Czabanowski
- nr 100
Hambase
Martin de Wit
- nr 101
Sound Transmission through Pipe Systems and into Building Structures
Susanne Bron-van der Jagt
- nr 102
Het Bouwkundig Contrapunt
Jan Francis Boelen
- nr 103
A Framework for a Multi-Agent Planning Support System
Dick Saarloos
- nr 104
Bracing Steel Frames with Calcium Silicate Element Walls
Bright Mweene Ng'andu
- nr 105
Naar een Nieuwe Houtskeletbouw
F.N.G. De Medts

nr 106 and 107
Niet gepubliceerd

nr 108
Geborgenheid
T.E.L. van Pinxteren

nr 109
Modelling Strategic Behaviour in Anticipation of Congestion
Qi Han

nr 110
Reflecties op het Woondomein
Fred Sanders

nr 111
On Assessment of Wind Comfort by Sand Erosion
Gábor Dezsö

nr 112
Bench Heating in Monumental Churches
Dionne Limpens-Neilen

nr 113
RE. Architecture
Ana Pereira Roders

nr 114
Toward Applicable Green Architecture
Usama El Fiky

nr 115
Knowledge Representation under Inherent Uncertainty in a Multi-Agent System for Land Use Planning
Liyang Ma

nr 116
Integrated Heat Air and Moisture Modeling and Simulation
Jos van Schijndel

nr 117
Concrete Behaviour in Multiaxial Compression
J.P.W. Bongers

nr 118
The Image of the Urban Landscape
Ana Moya Pellitero

nr 119
The Self-Organizing City in Vietnam
Stephanie Geertman

nr 120
A Multi-Agent Planning Support System for Assessing Externalities of Urban Form Scenarios
Rachel Katoshevski-Cavari

nr 121
Den Schulbau Neu Denken, Fühlen und Wollen
Urs Christian Maurer-Dietrich

nr 122
Peter Eisenman Theories and Practices
Bernhard Kormoss

nr 123
User Simulation of Space Utilisation
Vincent Tabak

nr 125
In Search of a Complex System Model
Oswald Devisch

nr 126
Lighting at Work: Environmental Study of Direct Effects of Lighting Level and Spectrum on Psycho-Physiological Variables
Grazyna Górnicka

nr 127
Flanking Sound Transmission through Lightweight Framed Double Leaf Walls
Stefan Schoenwald

nr 128
Bounded Rationality and Spatio-Temporal Pedestrian Shopping Behavior
Wei Zhu

nr 129
Travel Information: Impact on Activity Travel Pattern
Zhongwei Sun

nr 130
Co-Simulation for Performance Prediction of Innovative Integrated Mechanical Energy Systems in Buildings
Marija Trcka

nr 131
Niet gepubliceerd

- nr 132
Architectural Cue Model in Evacuation Simulation for Underground Space Design
Chengyu Sun
- nr 133
Uncertainty and Sensitivity Analysis in Building Performance Simulation for Decision Support and Design Optimization
Christina Hopfe
- nr 134
Facilitating Distributed Collaboration in the AEC/FM Sector Using Semantic Web Technologies
Jacob Beetz
- nr 135
Circumferentially Adhesive Bonded Glass Panes for Bracing Steel Frame in Façades
Edwin Huveners
- nr 136
Influence of Temperature on Concrete Beams Strengthened in Flexure with CFRP
Ernst-Lucas Klamer
- nr 137
Sturen op Klantwaarde
Jos Smeets
- nr 139
Lateral Behavior of Steel Frames with Discretely Connected Precast Concrete Infill Panels
Paul Teewen
- nr 140
Integral Design Method in the Context of Sustainable Building Design
Perica Savanovic
- nr 141
Household Activity-Travel Behavior: Implementation of Within-Household Interactions
Renni Anggraini
- nr 142
Design Research in the Netherlands 2010
Henri Achten
- nr 143
Modelling Life Trajectories and Transport Mode Choice Using Bayesian Belief Networks
Marloes Verhoeven
- nr 144
Assessing Construction Project Performance in Ghana
William Gyadu-Asiedu
- nr 145
Empowering Seniors through Domotic Homes
Masi Mohammadi
- nr 146
An Integral Design Concept for Ecological Self-Compacting Concrete
Martin Hunger
- nr 147
Governing Multi-Actor Decision Processes in Dutch Industrial Area Redevelopment
Erik Blokhuis
- nr 148
A Multifunctional Design Approach for Sustainable Concrete
Götz Hüsken
- nr 149
Quality Monitoring in Infrastructural Design-Build Projects
Ruben Favié
- nr 150
Assessment Matrix for Conservation of Valuable Timber Structures
Michael Abels
- nr 151
Co-simulation of Building Energy Simulation and Computational Fluid Dynamics for Whole-Building Heat, Air and Moisture Engineering
Mohammad Mirsadeghi
- nr 152
External Coupling of Building Energy Simulation and Building Element Heat, Air and Moisture Simulation
Daniel Cóstola

- nr 153
**Adaptive Decision Making In
Multi-Stakeholder Retail Planning**
Ingrid Janssen
- nr 154
Landscape Generator
Kymo Slager
- nr 155
Constraint Specification in Architecture
Remco Niemeijer
- nr 156
**A Need-Based Approach to
Dynamic Activity Generation**
Linda Nijland
- nr 157
**Modeling Office Firm Dynamics in an
Agent-Based Micro Simulation Framework**
Gustavo Garcia Manzato
- nr 158
**Lightweight Floor System for
Vibration Comfort**
Sander Zegers
- nr 159
Aanpasbaarheid van de Draagstructuur
Roel Gijsbers
- nr 160
'Village in the City' in Guangzhou, China
Yanliu Lin
- nr 161
Climate Risk Assessment in Museums
Marco Martens
- nr 162
Social Activity-Travel Patterns
Pauline van den Berg
- nr 163
**Sound Concentration Caused by
Curved Surfaces**
Martijn Vercammen
- nr 164
**Design of Environmentally Friendly
Calcium Sulfate-Based Building Materials:
Towards an Improved Indoor Air Quality**
Qingliang Yu
- nr 165
**Beyond Uniform Thermal Comfort
on the Effects of Non-Uniformity and
Individual Physiology**
Lisje Schellen
- nr 166
Sustainable Residential Districts
Gaby Abdalla
- nr 167
**Towards a Performance Assessment
Methodology using Computational
Simulation for Air Distribution System
Designs in Operating Rooms**
Mônica do Amaral Melhado
- nr 168
**Strategic Decision Modeling in
Brownfield Redevelopment**
Brano Glumac
- nr 169
**Pamela: A Parking Analysis Model
for Predicting Effects in Local Areas**
Peter van der Waerden
- nr 170
**A Vision Driven Wayfinding Simulation-
System Based on the Architectural Features
Perceived in the Office Environment**
Qunli Chen
- nr 171
**Measuring Mental Representations
Underlying Activity-Travel Choices**
Oliver Horeni
- nr 172
**Modelling the Effects of Social Networks
on Activity and Travel Behaviour**
Nicole Ronald
- nr 173
**Uncertainty Propagation and Sensitivity
Analysis Techniques in Building
Performance Simulation to Support
Conceptual Building and System Design**
Christian Struck
- nr 174
**Numerical Modeling of Micro-Scale
Wind-Induced Pollutant Dispersion
in the Built Environment**
Pierre Gousseau

nr 175

**Modeling Recreation Choices
over the Family Lifecycle**

Anna Beatriz Grigolon

nr 176

**Experimental and Numerical Analysis of
Mixing Ventilation at Laminar, Transitional
and Turbulent Slot Reynolds Numbers**

Twan van Hooff

nr 177

**Collaborative Design Support:
Workshops to Stimulate Interaction and
Knowledge Exchange Between Practitioners**

Emile M.C.J. Quanjel

nr 178

Future-Proof Platforms for Aging-in-Place

Michiel Brink

nr 179

**Motivate:
A Context-Aware Mobile Application for
Physical Activity Promotion**

Yuzhong Lin

nr 180

**Experience the City:
Analysis of Space-Time Behaviour and
Spatial Learning**

Anastasia Moiseeva

nr 181

**Unbonded Post-Tensioned Shear Walls of
Calcium Silicate Element Masonry**

Lex van der Meer

nr 182

**Construction and Demolition Waste
Recycling into Innovative Building Materials
for Sustainable Construction in Tanzania**

Mwita M. Sabai

nr 183

**Durability of Concrete
with Emphasis on Chloride Migration**

Przemysław Spiesz

nr 184

**Computational Modeling of Urban
Wind Flow and Natural Ventilation
Potential of Buildings**

Rubina Ramponi

nr 185

**A Distributed Dynamic Simulation
Mechanism for Buildings Automation
and Control Systems**

Azzedine Yahiaoui

nr 186

**Modeling Cognitive Learning of Urban
Networks in Daily Activity-Travel Behavior**

Sehnaz Cenani Durmazoglu

nr 187

**Functionality and Adaptability of Design
Solutions for Public Apartment Buildings
in Ghana**

Stephen Agyefi-Mensah

nr 188

**A Construction Waste Generation Model
for Developing Countries**

Lilliana Abarca-Guerrero

nr 189

**Synchronizing Networks:
The Modeling of Supernetworks for
Activity-Travel Behavior**

Feixiong Liao

nr 190

**Time and Money Allocation Decisions
in Out-of-Home Leisure Activity Choices**

Gamze Zeynep Dane

nr 191

**How to Measure Added Value of CRE and
Building Design**

Rianne Appel-Meulenbroek

nr 192

**Secondary Materials in Cement-Based
Products:
Treatment, Modeling and Environmental
Interaction**

Miruna Florea

nr 193

**Concepts for the Robustness Improvement
of Self-Compacting Concrete:
Effects of Admixtures and Mixture
Components on the Rheology and Early
Hydration at Varying Temperatures**

Wolfram Schmidt

nr 194

Modelling and Simulation of Virtual Natural Lighting Solutions in Buildings

Rizki A. Mangkuto

nr 195

Nano-Silica Production at Low Temperatures from the Dissolution of Olivine - Synthesis, Tailoring and Modelling

Alberto Lazaro Garcia

nr 196

Building Energy Simulation Based Assessment of Industrial Halls for Design Support

Bruno Lee

nr 197

Computational Performance Prediction of the Potential of Hybrid Adaptable Thermal Storage Concepts for Lightweight Low-Energy Houses

Pieter-Jan Hoes

nr 198

Application of Nano-Silica in Concrete

George Quercia Bianchi

nr 199

Dynamics of Social Networks and Activity Travel Behaviour

Fariya Sharmeen

nr 200

Building Structural Design Generation and Optimisation including Spatial Modification

Juan Manuel Davila Delgado

nr 201

Hydration and Thermal Decomposition of Cement/Calcium-Sulphate Based Materials

Ariën de Korte

nr 202

Republiek van Beelden: De Politieke Werkingen van het Ontwerp in Regionale Planvorming

Bart de Zwart

nr 203

Effects of Energy Price Increases on Individual Activity-Travel Repertoires and Energy Consumption

Dujuan Yang

nr 204

Geometry and Ventilation: Evaluation of the Leeward Sawtooth Roof Potential in the Natural Ventilation of Buildings

Jorge Isaac Perén Montero

nr 205

Computational Modelling of Evaporative Cooling as a Climate Change Adaptation Measure at the Spatial Scale of Buildings and Streets

Hamid Montazeri

nr 206

Local Buckling of Aluminium Beams in Fire Conditions

Ronald van der Meulen

nr 207

Historic Urban Landscapes: Framing the Integration of Urban and Heritage Planning in Multilevel Governance

Loes Veldpaus

nr 208

Sustainable Transformation of the Cities: Urban Design Pragmatics to Achieve a Sustainable City

Ernesto Antonio Zumelzu Scheel

nr 209

Development of Sustainable Protective Ultra-High Performance Fibre Reinforced Concrete (UHPRFC): Design, Assessment and Modeling

Rui Yu

nr 210

Uncertainty in Modeling Activity-Travel Demand in Complex Urban Systems

Soora Rasouli

nr 211

Simulation-based Performance Assessment of Climate Adaptive Greenhouse Shells

Chul-sung Lee

nr 212

Green Cities: Modelling the Spatial Transformation of the Urban Environment using Renewable Energy Technologies

Saleh Mohammadi

- nr 213
A Bounded Rationality Model of Short and Long-Term Dynamics of Activity-Travel Behavior
Ifigeneia Psarra
- nr 214
Effects of Pricing Strategies on Dynamic Repertoires of Activity-Travel Behaviour
Elaheh Khademi
- nr 215
Handstorm Principles for Creative and Collaborative Working
Frans van Gassel
- nr 216
Light Conditions in Nursing Homes: Visual Comfort and Visual Functioning of Residents
Marianne M. Sinoo
- nr 217
**Woonsporen:
De Sociale en Ruimtelijke Biografie van een Stedelijk Bouwblok in de Amsterdamse Transvaalbuurt**
Hüseyin Hüsnü Yegenoglu
- nr 218
Studies on User Control in Ambient Intelligent Systems
Berent Willem Meerbeek
- nr 219
Daily Livings in a Smart Home: Users' Living Preference Modeling of Smart Homes
Erfaneh Allameh
- nr 220
Smart Home Design: Spatial Preference Modeling of Smart Homes
Mohammadali Heidari Jozam
- nr 221
**Wonen:
Discoursen, Praktijken, Perspectieven**
Jos Smeets
- nr 222
**Personal Control over Indoor Climate in Offices:
Impact on Comfort, Health and Productivity**
Atze Christiaan Boerstra
- nr 223
Personalized Route Finding in Multimodal Transportation Networks
Jianwe Zhang
- nr 224
The Design of an Adaptive Healing Room for Stroke Patients
Elke Daemen
- nr 225
Experimental and Numerical Analysis of Climate Change Induced Risks to Historic Buildings and Collections
Zara Huijbregts
- nr 226
Wind Flow Modeling in Urban Areas Through Experimental and Numerical Techniques
Alessio Ricci
- nr 227
Clever Climate Control for Culture: Energy Efficient Indoor Climate Control Strategies for Museums Respecting Collection Preservation and Thermal Comfort of Visitors
Rick Kramer
- nr 228
Fatigue Life Estimation of Metal Structures Based on Damage Modeling
Sarmediran Silitonga
- nr 229
A multi-agents and occupancy based strategy for energy management and process control on the room-level
Timilehin Moses Labeodan
- nr 230
Environmental assessment of Building Integrated Photovoltaics: Numerical and Experimental Carrying Capacity Based Approach
Michiel Ritzen
- nr 231
Performance of Admixture and Secondary Minerals in Alkali Activated Concrete: Sustaining a Concrete Future
Arno Keulen

nr 232

World Heritage Cities and Sustainable Urban Development: Bridging Global and Local Levels in Monitoring the Sustainable Urban Development of World Heritage Cities
Paloma C. Guzman Molina

nr 233

Stage Acoustics and Sound Exposure in Performance and Rehearsal Spaces for Orchestras: Methods for Physical Measurements
Remy Wenmaekers

nr 234

Municipal Solid Waste Incineration (MSWI) Bottom Ash: From Waste to Value Characterization, Treatments and Application
Pei Tang

nr 235

Large Eddy Simulations Applied to Wind Loading and Pollutant Dispersion
Mattia Ricci

nr 236

Alkali Activated Slag-Fly Ash Binders: Design, Modeling and Application
Xu Gao

nr 237

Sodium Carbonate Activated Slag: Reaction Analysis, Microstructural Modification & Engineering Application
Bo Yuan

nr 238

Shopping Behavior in Malls
Widiyani

nr 239

Smart Grid-Building Energy Interactions: Demand Side Power Flexibility in Office Buildings
Kennedy Otieno Aduda

nr 240

Modeling Taxis Dynamic Behavior in Uncertain Urban Environments
Zheng Zhong

nr 241

Gap-Theoretical Analyses of Residential Satisfaction and Intention to Move
Wen Jian

nr 242

Travel Satisfaction and Subjective Well-Being: A Behavioral Modeling Perspective
Yanan Gao

nr 243

Building Energy Modelling to Support the Commissioning of Holistic Data Centre Operation
Vojtech Zavrel

nr 244

Regret-Based Travel Behavior Modeling: An Extended Framework
Sunghoon Jang

nr 245

Towards Robust Low-Energy Houses: A Computational Approach for Performance Robustness Assessment using Scenario Analysis
Rajesh Reddy Kotireddy

nr 246

Development of sustainable and functionalized inorganic binder-biofiber composites
Guillaume Doudart de la Grée

nr 247

A Multiscale Analysis of the Urban Heat Island Effect: From City Averaged Temperatures to the Energy Demand of Individual Buildings
Yasin Toparlar

nr 248

Design Method for Adaptive Daylight Systems for buildings covered by large (span) roofs
Florian Heinzelmänn

nr 249

Hardening, high-temperature resistance and acid resistance of one-part geopolymers
Patrick Sturm

- nr 250
Effects of the built environment on dynamic repertoires of activity-travel behaviour
Aida Pontes de Aquino
- nr 251
Modeling for auralization of urban environments: Incorporation of directivity in sound propagation and analysis of a framework for auralizing a car pass-by
Fotis Georgiou
- nr 252
Wind Loads on Heliostats and Photovoltaic Trackers
Andreas Pfahl
- nr 253
Approaches for computational performance optimization of innovative adaptive façade concepts
Roel Loonen
- nr 254
Multi-scale FEM-DEM Model for Granular Materials: Micro-scale boundary conditions, Statics, and Dynamics
Jiadun Liu
- nr 255
Bending Moment - Shear Force Interaction of Rolled I-Shaped Steel Sections
Rianne Willie Adriana Dekker
- nr 256
Paralympic tandem cycling and handcycling: Computational and wind tunnel analysis of aerodynamic performance
Paul Fionn Mannion
- nr 257
Experimental characterization and numerical modelling of 3D printed concrete: Controlling structural behaviour in the fresh and hardened state
Robert Johannes Maria Wolfs
- nr 258
Requirement checking in the building industry: Enabling modularized and extensible requirement checking systems based on semantic web technologies
Chi Zhang
- nr 259
A Sustainable Industrial Site Redevelopment Planning Support System
Tong Wang
- nr 260
Efficient storage and retrieval of detailed building models: Multi-disciplinary and long-term use of geometric and semantic construction information
Thomas Ferdinand Krijnen
- nr 261
The users' value of business center concepts for knowledge sharing and networking behavior within and between organizations
Minou Weijs-Perrée
- nr 262
Characterization and improvement of aerodynamic performance of vertical axis wind turbines using computational fluid dynamics (CFD)
Abdolrahim Rezaeiha
- nr 263
In-situ characterization of the acoustic impedance of vegetated roofs
Chang Liu
- nr 264
Occupancy-based lighting control: Developing an energy saving strategy that ensures office workers' comfort
Christel de Bakker
- nr 265
Stakeholders-Oriented Spatial Decision Support System
Cahyono Susetyo
- nr 266
Climate-induced damage in oak museum objects
Rianne Aleida Luimes
- nr 267
Towards individual thermal comfort: Model predictive personalized control of heating systems
Katarina Katic

nr 268

Modelling and Measuring Quality of Urban Life: Housing, Neighborhood, Transport and Job

Lida Aminian

nr 269

Optimization of an aquifer thermal energy storage system through integrated modelling of aquifer, HVAC systems and building

Basar Bozkaya

nr 270

Numerical modeling for urban sound propagation: developments in wave-based and energy-based methods

Raúl Pagán Muñoz

nr 271

Lighting in multi-user office environments: improving employee wellbeing through personal control

Sanae van der Vleuten-Chraibi

nr 272

A strategy for fit-for-purpose occupant behavior modelling in building energy and comfort performance simulation

Isabella I. Gaetani dell'Aquila d'Aragona

nr 273

Een architectuurhistorische waardestelling van naoorlogse woonwijken in Nederland: Het voorbeeld van de Westelijke Tuinsteden in Amsterdam

Eleonore Henriette Marie Mens

nr 274

Job-Housing Co-Dependent Mobility Decisions in Life Trajectories

Jia Guo

nr 275

A user-oriented focus to create healthcare facilities: decision making on strategic values

Emilia Rosalia Catharina Maria Huisman

nr 276

Dynamics of plane impinging jets at moderate Reynolds numbers – with applications to air curtains

Adelya Khayrullina

nr 277

Valorization of Municipal Solid Waste Incineration Bottom Ash - Chemical Nature, Leachability and Treatments of Hazardous Elements

Qadeer Alam

nr 278

Treatments and valorization of MSWI bottom ash - application in cement-based materials

Veronica Caprai

nr 279

Personal lighting conditions of office workers - input for intelligent systems to optimize subjective alertness

Juliëtte van Duijnhoven

nr 280

Social influence effects in tourism travel: air trip itinerary and destination choices

Xiaofeng Pan

nr 281

Advancing Post-War Housing: Integrating Heritage Impact, Environmental Impact, Hygrothermal Risk and Costs in Renovation Design Decisions

Lisanne Claartje Havinga

nr 282

Impact resistant ultra-high performance fibre reinforced concrete: materials, components and properties

Peipeng Li

nr 283

Demand-driven Science Parks: The Perceived Benefits and Trade-offs of Tenant Firms with regard to Science Park Attributes

Wei Keat Benny Ng

nr 284

Raise the lantern; how light can help to maintain a healthy and safe hospital environment focusing on nurses

Maria Petronella Johanna Aarts

nr 285

Modelling Learning and Dynamic Route and Parking Choice Behaviour under Uncertainty

Elaine Cristina Schneider de Carvalho

nr 286

Identifying indoor local microclimates for safekeeping of cultural heritage

Karin Kompatscher

nr 287

Probabilistic modeling of fatigue resistance for welded and riveted bridge details. Resistance models and estimation of uncertainty.

Davide Leonetti

nr 288

Performance of Layered UHPFRC under Static and Dynamic Loads: Effects of steel fibers, coarse aggregates and layered structures

Yangyueye Cao

nr 289

Photocatalytic abatement of the nitrogen oxide pollution: synthesis, application and long-term evaluation of titania-silica composites

Yuri Hendrix

nr 290

Assessing knowledge adoption in postdisaster reconstruction: Understanding the impact of hazard-resistant construction knowledge on reconstruction processes of self-recovering communities in Nepal and the Philippines

Eefje Hendriks

nr 291

Locating electric vehicle charging stations: A multi-agent based dynamic simulation

Seheon Kim

nr 292

De invloed van Lean Management op de beheersing van het bouwproces

Wim van den Bouwhuisen

nr 293

Neighborhood Environment and Physical Activity of Older Adults

Zhengying Liu

nr 294

Practical and continuous luminance distribution measurements for lighting quality

Thijs Willem Kruisselbrink

nr 295

Auditory Distraction in Open-Plan Study Environments in Higher Education

Pieterella Elizabeth Braat-Eggen

nr 296

Exploring the effect of the sound environment on nurses' task performance: an applied approach focusing on prospective memory

Jikke Reinten

nr 297

Design and performance of water resistant cementitious materials– Mechanisms, evaluation and applications

Zhengyao Qu

nr 298

Design Optimization of Seasonal Thermal Energy Storage Integrated District Heating and Cooling System: A Modeling and Simulation Approach

Luyi Xu

nr 299

Land use and transport: Integrated approaches for planning and management

Zhongqi Wang

nr 300

Multi-disciplinary optimization of building spatial designs: co-evolutionary design process simulations, evolutionary algorithms, hybrid approaches

Sjonnie Boonstra

nr 301

Modeling the spatial and temporal relation between urban land use, temperature, and energy demand

Hung-Chu Chen

nr 302

Seismic retrofitting of masonry walls with flexible deep mounted CFRP strips

Ömer Serhat Türkmen

nr 303

Coupled Aerostructural Shape and Topology Optimization of Horizontal-Axis Wind Turbine Rotor Blades

Zhijun Wang

nr 304

Valorization of Recycled Waste Glass and Converter Steel Slag as Ingredients for Building Materials: Hydration and Carbonation Studies

Gang Liu

nr 305

Low-Carbon City Development based on Land Use Planning

Gengzhe Wang

nr 306

Sustainable energy transition scenario analysis for buildings and neighborhoods - Data driven optimization

Shalika Saubhagya Wickramarachchi Walker

nr 307

In-between living and manufactured: an exploratory study on biobuilding components for building design

Berrak Kirbas Akyurek

The concrete sector is one of the largest industrial emitters of CO₂. The emission of CO₂ is mainly associated with the combustion processes during the manufacture of traditional Portland cement. Therefore, attempts are made to minimize or even eliminate the use of Portland cement in concrete. The wide availability of industrial by-products (e.g., slags and fly ashes) render them great candidates for cement substitutes. However, the chemical and mineralogical composition of by-products and industrial wastes may vary significantly. Consequently, in-depth analyses of these materials are needed to produce high-quality building products. Before being used in concrete, industrial wastes often require treatments, and in many cases, chemical or physical activation is necessary to ensure their safe utilization and sufficient reactivity. Optimization of these processes is essential to meet the goal of reduced environmental impact. Since concrete is mostly available in highly urbanized areas, its eco-friendly aspects can be extended with the use of photocatalytic technology. Large concrete surfaces can serve as a matrix for photocatalysts enabling the degradation of air pollutants.

With a general strategy to provide climate-friendly solutions in the concrete industry, this thesis offers improvements for currently utilized eco-efficient technologies in concrete (including alkali-activated materials and air-purifying concrete) and investigates the cementitious potential of alternative binders (steel slag).

DEPARTMENT OF THE BUILT ENVIRONMENT